



저작자표시-비영리-변경금지 2.0 대한민국

이용자는 아래의 조건을 따르는 경우에 한하여 자유롭게

- 이 저작물을 복제, 배포, 전송, 전시, 공연 및 방송할 수 있습니다.

다음과 같은 조건을 따라야 합니다:



저작자표시. 귀하는 원저작자를 표시하여야 합니다.



비영리. 귀하는 이 저작물을 영리 목적으로 이용할 수 없습니다.



변경금지. 귀하는 이 저작물을 개작, 변형 또는 가공할 수 없습니다.

- 귀하는, 이 저작물의 재이용이나 배포의 경우, 이 저작물에 적용된 이용허락조건을 명확하게 나타내어야 합니다.
- 저작권자로부터 별도의 허가를 받으면 이러한 조건들은 적용되지 않습니다.

저작권법에 따른 이용자의 권리는 위의 내용에 의하여 영향을 받지 않습니다.

이것은 [이용허락규약\(Legal Code\)](#)을 이해하기 쉽게 요약한 것입니다.

[Disclaimer](#)

Doctor of Philosophy

**ELECTRIC FIELD CONTROL OF MAGNETIC
PROPERTIES IN Fe/BaTiO₃ MULTIFERROIC
HETEROSTRUCTURES**

The Graduate School of

UNIVERSITY OF ULSAN

KOREA RESEARCHER INSTITUTE STANDARDS AND SCIENCE

Department of Physics

Tran Thi Toan

**ELECTRIC FIELD CONTROL OF MAGNETIC
PROPERTIES IN Fe/BaTiO₃ MULTIFERROIC
HETEROSTRUCTURES**

Supervisors: Chanyong Hwang and Sunglae Cho

A dissertation

Submitted to

The Graduate School of the University of Ulsan

In partial Fullfillment of the Requirements for the Degree of

Doctor of Philosophy in Physics

Department of Physics

University of Ulsan, Korea

June 2024

ELECTRIC FIELD CONTROL OF MAGNETIC PROPERTIES IN Fe/BaTiO₃ MULTIFERROIC HETEROSTRUCTURES

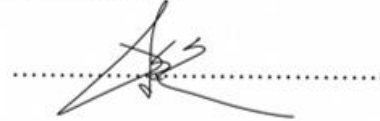
This certifies that the dissertation
of Tran Thi Toan is approved.

Professor Sung-hyon Rhim



Committee Chairman.

Professor Sanghoon Kim



Committee Member.

Professor Teun-Teun Kim



Committee Member.

Professor Sunglae Cho



Committee Member.

Professor Chanyong Hwang



Committee Member.

Department of Physics

University of Ulsan, Korea

June 2024

ABSTRACT

In traditional spintronics devices, magnetization can be controlled by injecting a current from applying a magnetic field. However, these methods have the drawback of high energy consumption. Recently, spin-transfer torque devices have emerged, eliminating the need for an external field. Nonetheless, the energy consumption remains due to increased Joule heating resulting from direct electric current writing. To address these challenges, there is a growing interest in alternative approaches that enable the processing and writing of magnetic information using electric field, thus eliminating the need for electric currents. Multiferroics (MFs), which combine both ferromagnetic (FM) and ferroelectric (FE) properties, have shown promise for electric field control of the magnetism. Among various FM/FE multiferroic heterostructures, Fe/BaTiO₃ (BTO) is particularly noteworthy due to its unique intimate lattice mismatch of approximately 1.3% and high Curie temperature of Fe (780°C). BTO is a well-studied ferroelectric material with successive structural phase transitions and remarkable domain configuration at room temperature. Several reports have observed the control of magnetic anisotropy, magnetic moment, and magnetic domains of Fe film using electric field. Especially, a novel physical mechanism has been revealed, illustrating interfacial magnetoelastic coupling at the Fe/BTO interface. This discovery showcases the potential for room temperature electrical and reversible on/off switching of the interfacial magnetization, suggesting significant application in the electric field control of magnetic properties through the magnetoelectric coupling. However, experimental results with Fe/BTO films demonstrated a less-than-90° rotation of magnetization, which does not meet requirement of spintronic device basing on 180° deterministic control of magnetization. Therefore, enhancing magnetoelectric coupling is imperative. A critical condition for achieving substantial

magnetolectric coupling is a strong elastic coupling between magnetic and ferroelectric phases. To meet this requirement, epitaxial ferroelectric-ferromagnetic structures are fabricated to establish a structurally coherent interface under epitaxial strain, thus optimizing the elastic coupling between FM and FE phase. This dissertation primarily focus on enhancing the quality of Fe films by adjusting the growth temperature and controlling the magnetism and magnetic domains within these films thorough the application of external electric field. Furthermore, this provides valuable insights into the evolution of BTO domain configurations during the application of electric fields, revealing the formation of a single in-plane domain under the influence of an out-of-plane electric field.

TABLE OF CONTENTS

| | |
|--|--------------|
| ABSTRACT | I |
| TABLE OF CONTENTS | III |
| LIST OF FIGURES | VIII |
| LIST OF TABLES | XVIII |
| TERMS AND ABBREVIATIONS | XIX |
| CHAPTER 1: INTRODUCTION | 1 |
| 1.1 Description of the research..... | 1 |
| 1.2 Thesis outlines..... | 3 |
| 1.3 References | 4 |
| CHAPTER 2: THEORETICAL BACKGROUND | 6 |
| I. MAGNETISM | 6 |
| 2.1 Magnetism and magnetic materials..... | 6 |
| 2.2 Model for Ferromagnetism | 9 |
| 2.3 Magnetic energy..... | 11 |
| 2.2.1 Exchange energy..... | 12 |
| 2.3.2 Magnetostatic energy..... | 12 |
| 2.3.3 Magnetocrystalline energy | 14 |
| 2.3.4 Magnetoelastic energy..... | 15 |

| | |
|---|-----------|
| 2.4 Magnetization in Ferromagnets..... | 16 |
| 2.4.1 Magnetic domains and domain walls | 16 |
| 2.4.2 Magnetization process | 17 |
| 2.4.3 The effects of elastic stress | 19 |
| II. PIZOELECTRIC - FERROELECTRICITY | 21 |
| 2.5 Polarization in Ferroelectricity..... | 21 |
| 2.5.1 Piezoelectric effect | 21 |
| 2.5.2 Phase transition and Ferroelectricity (BTO)..... | 22 |
| 2.5.3 Ferroelectric domains | 24 |
| 2.5.4 Hysteresis and polarization switching (BTO) | 29 |
| 2.5.5 Operating modes of piezo-materials..... | 30 |
| III. MULTIFERROIC MATERIALS | 36 |
| 2.6 Multiferroic types..... | 36 |
| 2.6.1 Types of ferroic ordering..... | 36 |
| 2.6.2 Multiferroic materials..... | 39 |
| 2.6.3 Magnetoelectric effect | 44 |
| 2.6.4 Electric field control magnetism in thin films..... | 46 |
| 2.6.5 Applications of Multiferroics Materials on Spintronics..... | 50 |
| 2.6 Reference..... | 56 |
| CHAPTER 3: LITERATURE REVIEW | 59 |

| | |
|---|-----------|
| 3.1 Fe/BaTiO ₃ domain patterns..... | 59 |
| 3.2 Unique interface of Fe/BTO heterostructures | 61 |
| 3.3 The remaining challenges..... | 63 |
| 3.4 References | 64 |
| CHAPTER 4: METHODOLOGY | 65 |
| 4.1 Molecular Beam Epitaxial (MBE) for thin film growth | 65 |
| 4.1.2 MBE setup | 66 |
| 4.1.3 Calibrations: substrate temperature, growth rate | 67 |
| 4.2 Microstructural characterization | 68 |
| 4.2.1 X-ray diffraction (XRD)..... | 68 |
| 4.2.2 Reflection high energy electron diffraction (RHEED)..... | 70 |
| 4.3 Polarized light microscope (PLM) | 71 |
| 4.4 Magneto-Optical Kerr effect magnetometer (MOKE)..... | 74 |
| 4.5 Vibrating Sample Magnetometer (VSM)..... | 77 |
| 4.6 High voltage set-up for the converse ME effect | 78 |
| 4.7 References | 79 |
| CHAPTER 5: GROWTH TEMPERATURE DEPENDENCE MAGNETIC PROPERTIES OF EPITAXY Fe FILM ON BaTiO₃ | 80 |
| 5.1 Introduction | 80 |
| 5.2 Experiment methods..... | 82 |

| | |
|--|------------|
| 5.3 Results and discussions | 82 |
| 5.4 Conclusion..... | 90 |
| 5.5 References | 91 |
| CHAPTER 6: THE INSIGHTFUL UNDERSTANDING ON P-E HYSTERESIS LOOP OF BaTiO₃ SINGLE CRYSTAL USING POLARIZED LIGHT MICROSCOPE | 94 |
| 6.1 Introduction | 94 |
| 6.2 Experiment methods..... | 97 |
| 6.3 Results and discussion..... | 98 |
| 6.4 Conclusion..... | 112 |
| 6.5 References | 113 |
| CHAPTER 7: ELECTRIC FIELD CONTROL OF MAGNETIC ANISOTROPY OF Fe FILM ON ALTERNATING a₁-a₂ BTO DOMAINS | 118 |
| 7.1 Introduction | 119 |
| 7.2 Experiment methods..... | 120 |
| 7.3 Results and discussions | 121 |
| 7.4 Conclusion..... | 138 |
| 7.5 References | 139 |
| CHAPTER 8: REVERSIBLE ELECTRIC-FIELD-DRIVEN MAGNETIC ANISOTROPY OF FE/BTO HETEROSTRUCTURES | 144 |
| 8.1 Introduction | 144 |

| | |
|-------------------------------------|------------|
| 8.2 Experiment methods..... | 145 |
| 8.3 Results and discussions | 146 |
| 8.4 Conclusion..... | 155 |
| 8.5 References | 156 |
| CHAPTER 9: CONCLUSIONS | 161 |
| ACKNOWLEDGEMENT..... | 163 |

LIST OF FIGURES

| | |
|--|----|
| Figure 2.1. Schematic of the origin of magnetism from the electronic structure in a free atom. .. | 6 |
| Figure 2.2. Schematic magnetization curves and magnetic ordering for magnetic materials | 7 |
| Figure 2.3. Schematic showing the density of states of 3d bands near Fermi level (E_F) in 3d transition metal. Splitting of spin-up and spin-down electron states at Fermi level giving rise to ferromagnetism. The δE is the energy gain per electron. [1]..... | 10 |
| Figure 2.4. Reduce of the magnetic energy by domain formaton in ferromagnet. [2] | 17 |
| Figure 2.5. Magnetic hysteresis loop for a ferromagnets [3]..... | 18 |
| Figure 2.6. Schematic representation: the strain (top) and stress (bottom)-induced domain reorientation, $90/180^\circ$ domain wall and magnetization direction. | 20 |
| Figure 2.7. Direct piezoelectric effect (a) and converse piezoelectric effect (b)..... | 21 |
| Figure 2.8. BTO crystal structure belonging to the perovskite family. | 22 |
| Figure 2.9. Changes in primate-cell lattice parameters and anomalies in relative permittivity during the sequence of phase transition in BTO. The right side of figure illustrates the crystal structure of the cubic prototype phase and the unit cell distortions in each of the ferroelectric phase of BTO. [4]..... | 24 |
| Figure 2.10. Schematic illustration of three possible domain patterns in tetragonal $BaTiO_3$ crystals with a (001)-oriented surface. [5] | 26 |
| Figure 2.11. The perovskite crystal common to many ferroelectric ceramics. For BTO the white ions at the corners are Ba with a +2 charge, the black ions on the faces are oxygen ions with a -2 charge and the central ion is Ti with a +4 charge. The top of figures illustrates the phase change through the Curie temperature, the spontaneous polarization, and the linear response of the crystal. | |

The bottom set of figures illustrates the spontaneous shape change of the crystal, and 180° and 90° switching due to applied electric field or stress. 27

Figure 2.12. Schematic illustration of the unit cell shape of tetragonal BTO. The a-domain have in-plane polarization direction, and the c-domain have out-of-plane polarization direction. 28

Figure 2.13. Polarization-electric field hysteresis loops of ferroelectric crystal with remanent polarization P_r and coercive field E_c where the polarization value of zero. (a), (b), (c), (d), and (e) represent different polarization configurations under an applied electric field. The strain-electric field butterfly loop is also shown here.[6] 29

Figure 2.14. A cuboid under load by application of forces to a pair of opposing faces, to generate a normal stress, σ . [7] 31

Figure 2.15. A cuboid under load by application of forces to two pairs of opposing faces, with the forces acting parallel to the faces, to generate a shear stresses, τ . [7] 32

Figure 2.16. Direction of forces affecting a piezoelectric element. [8] 33

Figure 2.17. Schematic of a ferroelastic phase transition. As the temperature is cooled below T_C the cubic paraelastic structure undergoes a phase change to one of the degenerate tetragonal variants shown. A mechanical stress can be used to transform between the variants. 37

Figure 2.18. Simple arrangements of magnetic moments which can lead to toroidal moments. (a) and (b) have equal and opposite toroidal moments. The antiferromagnetic arrangement in (c) has toroidal moment, whereas that in (d) does not [19]. 38

Figure 2.19. Forms of ferroic order and their transformation properties under the parity operations of spatial inversion and time reversal. 38

Figure 2.20. Multiferroic materials with the coexistence of the at least two ferroic properties. . 39

Figure 2.21. Schematic representation of the order parameter and single-multiferroic BiFeO₃ crystal structure. The yellow, green, and blue arrows indicate the polarization, while the shaded plane represents the antiferromagnetic plane. (a) The crystal structure of BiFeO₃ is oriented (001). (b) Diagram showing how the weak ferromagnetic moment in BiFeO₃ is formed by the Dzyaloshinskii-Moriya interaction. (c) An additional antiferromagnetic plane, with shifts of 190 degrees for (c), 109 degrees for (d), and 71 degrees for (e). An external electric field causes the antiferromagnetic planes to reorient.[14]..... 41

Figure 2.22. Schematic illustration of (a) 0-3, (b) 1-3, (c) 2-2 type structure on a substrate [15]42

Figure 2.23. Schematic Diagrammatic representation of converse magnetoelectric coupling mediated by strain. Through the piezomagnetic effect, strain that an electric field creates in the ferroelectric material is mechanically transferred to the magnetic material, changing the magnetization.[17] 45

Figure 2.24. Schematic illustration of ideal ME effect 46

Figure 2.25. (a)-(c) Schematic of the different magnetoelectric response in composite multiferroics, (d)-(g) magnetic hysteresis loops for the different interfacial couplings responsible for the magnetoelectric coupling.[18]..... 48

Figure 2.26. Basic MRAM cell structure. [18] 52

Figure 2.27. Basic FeRAM cell structure [18]..... 53

Figure 2.28. Sketch of a possible MERAM element.[18]..... 54

Figure 2.29. FM/FE/FM tunnel junction model..... 55

Figure 3.1. Schematic illustration of the domain configuration in the Fe/BTO system. (a) a-c domain, (b) a₁-a₂ domain, and (c) room temperature lattice parameters of the BTO substrate and

the in-plane strains of the Fe film. (c) Unit cell of the BTO at tetragonal phase on the a and c domains. 60

Figure 3.2. Minority-spin charge density at the Fe/BTO interface for two opposite electric polarization in BTO. The arrows indicate the directions of electric polarizations.[6] 61

Figure 3.3. (a) The high-angle annular dark-field images and the interface model of Fe/BTO heterostructure. (b) The schemes of the Fe/BTO interfaces for P_{up} and P_{down} , and the XMCD signals in the Fe- L_3 energy region for BTO polarization P_{up} (blue circles) and P_{down} (red squares) for capacitors at 300 K.[6]..... 62

Figure 4.1. Diagram of our MBE system (AMS’s lab)..... 67

Figure 4.2. Calibration of substrate temperature (left) and growth rate of Fe cell (right) 68

Figure 4.3. Simplified schematic of X-ray diffractometer in θ - 2θ Bragg reflection geometry. .. 69

Figure 4.4. The polarized light microscope measurement setup for BTO (001) single crystal under applying an out-of-plane electric field..... 72

Figure 4.5. The schematic illustration of the principle of the reflection in the tetragonal BTO molecules to the incident polarized light. P is the polarization of domains with the polarization direction is represented by the double-head arrows in the in the inside of domains. (a) An electric field direction is parallel to the polarization direction. (b) An electric field direction is perpendicular to the polarization direction of BTO..... 73

Figure 4.6. Domain observation by the Kerr effect. The three basic configuration of the polar, longitudinal, and transverse magneto-optical Kerr effect. The unit vector of magnetization is lying along the corresponding sensitivity axes (as indicated)..... 74

Figure 4.7. Schematic of MOKE devices of Spin Quantum Team (KRISS)..... 75

| | |
|--|-----|
| Figure 4.8. Schematic of Vibrating sample magnetometer (VSM) | 76 |
| Figure 4.9. A simplified schematic (not to scale) of high field longitude geometry MOKE system. A voltage was applied on the sample when the converse ME effect was characterized and a schematic of high-voltage set-up designed in the high H-field MOKE magnetometer | 78 |
| Figure 5.1. (a) RHEED patterns of BTO substrate and Fe films grown at 30, 100, 200, 300, and 400 °C along the BTO substrate's [110] azimuth. (b) Schematic illustration of Fe film and BTO substrate along Fe [100] // BTO [110] | 83 |
| Figure 5.2. (a) θ -2 θ XRD patterns of Fe films grown at 30, 100, 200, 300, and 400 °C. (b) The determined c-axis lattice constant (out-of-plane) and the corresponding strain of Fe films | 84 |
| Figure 5.3. Atomic schematic illustration (side view) of (left figure) the tensile strain and (right figure) the compressive strain Fe films grown on the tetragonal and cubic BTO, respectively... .. | 86 |
| Figure 5.4. Room temperature (a) in-plane and (b) out-of-plane magnetic hysteresis loops of Fe films grown at various temperatures. (c) Coercivity and saturation magnetization as a function of growth temperature. (d) Temperature dependence of normalized magnetization (M vs T curve) of Fe400 film under the magnetic field of 1 kOe. The rhombohedral, orthogonal, tetragonal, and cubic structural phases of BTO are represented by the letters R, O, T, and C, respectively..... | 89 |
| Figure 6.1. (a) Polarized light microscope (PLM) set up. (b) Birefringence images of BTO surface when the polarization of incident light is respect to a_1 - a_2 domain wall of 45°. | 99 |
| Figure 6.2. The relative contrast between a_1 and a_2 domain under rotating of polarization direction of indident light..... | 100 |

Figure 6.3. Polarization direction of a_1 and a_2 domain with incident polarization direction is respect 45° to domain wall. 100

Figure 6.4. Domain-switching process of BTO under applying electric with various speed. ... 102

Figure 6.5. (a-f) The alternating a_1 - a_2 stripe ferroelectric domains evolve when an out-of-plane electric field of 0 to 6 kV/cm is applied. The voltage rises at a rate of 10 V/min. The polarization directions of a_1 (gray region) and a_2 (dark region) stripe in-plane domains are indicated by the in-plane arrows. The out-of-plane domain is represented by the letter c, with the polarization direction shown by pointing away from the paper plane. (g-k) Schematic illustration of the observed BTO ferroelectric domain arrangement under applying an out-of-plane electric field (visualized Fig. 6.5a). The image is $100 \times 88 \mu\text{m}$ in size 103

Figure 6.6. (a-f) The alternating a_1 - a_2 stripe ferroelectric domains evolve when an out-of-plane electric field of 0 to - 6 kV/cm is applied. The voltage rises at a rate of 10 V/min. The polarization directions of a_1 (gray region) and a_2 (dark region) stripe in-plane domains are indicated by the in-plane arrows. The out-of-plane domain is represented by the letter c, with the polarization direction shown by the arrows pointing in the paper plane. (g-k) Schematic illustration of the observed BTO ferroelectric domain arrangement under applying an out-of-plane electric field (visualized Fig. 6.3a). The images size of $100 \times 88 \mu\text{m}$ 105

Figure 6.7. (a) 90° domain switch of BTO without domain wall motion. (b) Polarization – Electric field loop of BTO. The loop of sample I exhibit the 90° domain switching with domain wall motion. While, that of Sample II is without domain wall motion.[38] 106

Figure 6.8. Tetragonal unit cell of BTO in the cases: (a) the applied electric field value is smaller than that of the critical field. (b) the applied electric field value is larger than that of the critical electric field. 107

Figure 6.9. (a) The evolution of the single c domain under parallel and antiparallel out-of-plane electric field modulating from 6 to -6 kV/cm. The voltage rises at a rate of 10 V/min. The c+, c- with and denote the domain having the out-of-plane and anti-parallel-out-of-plane polarization direction pointing out and in the paper plane, respectively. The a₁ represents the in-plane domain having the polarization directions shown by the arrows. (b) Schematic illustration of the ferroelectric domain configuration under antiparallel out-of-plane electric field (visualized Fig. 6.9a). The images size of 100 × 88 μm. 109

Figure 6.10. (a) Tetragonal BTO unit cell, (b) Ti atoms switch from c+ to c- domain by 4 paths. In path 1, Ti atom can directly switch from c+ to c- position. In path 2, 3, and 4, Ti atom can jump to position A, then continuously jump to position c-. (c) The critical field for 90° and 180° domain switching of BTO.[39] 110

Figure 6.11. The summarized polarization – electric field (P-E) hysteresis loop of ferroelectric BTO from current studies. The red curve shows the polarization and electric field dependence from the virgin state to the saturation state. The tiny arrows and the number on the red curve show the direction of data observation. The numbers (orange circles) on hysteresis loop represent an order of measurement and corresponding position of the BTO domain with applying the antiparallel out-of-plane electric field on the c domain. The arrows on the sketched unit cell represent the polarization direction. 111

Figure 7.1. (a) RHEED patterns of BTO substrate and Fe films at growth temperature of 300 °C. (b) Room temperature XRD pattern of 10 nm Fe thin film formed on BTO substrate. 122

Figure 7.2. (a) Schematic illustration of the ferroelastic domain pattern of a cleaned BTO (001) substrate (left) and its ferroelectric (FE) microstructure after Fe film growth (right). (b) Schematic

illustration of the magnetic domain configuration of Fe/BTO film (left) and its MOKE image (right). The arrows in (a) indicate the direction of ferroelectric polarization, and the double-headed arrows in (b) represent the magnetic easy axes. 124

Figure 7.3. Experimental polar plots of (a) the squareness ratio (M_R/M_S) (above) and the magnetic switching fields (H_C) (bottom) of the Fe film grown on the BTO a_1 and a_2 domains. The [100] directions of the a_1 and a_2 domains of BTO substrate are denoted. (b) Magnetic hysteresis loops of Fe on single a_1 and a_2 domains measured at different magnetic field angles under zero electric field. The direction of magnetic field was modulated by sample rotation in the Kerr microscopy while electromagnet was fixed. The widths of the a_1 domain and a_2 domain are 5.13 and 15.1 μm , respectively. The α is angle between the applied magnetic field and the stripe domain walls... 126

Figure 7.4. (a) In-plane magnetic hysteresis loop of multi a_1 - a_2 Fe domains with applied magnetic field parallel to stripe domain. (b) Kerr microscopy images of a 10 nm thick epitaxial Fe film on BTO under some selected applied magnetic fields for magnetic field direction parallel to stripe domains. The number of images following the field value in hysteresis loop of (a)..... 127

Figure 7.5. (a) Schematic illustration of the observed BTO ferroelectric domain arrangement under applying an out-of-plane electric field. (b) FE domain configuration of the BTO under applied E of 6 kV/cm along out-of-plane direction. (c) Normalized Kerr magnetic hysteresis loops of the Fe film. (d) The analysis of differential-strain transfer from BTO substrate to Fe film... 129

Figure 7.6. The interpretation of the strain state that the BTO domains at their interface cause in the Fe film while the walls of the a_1 - a_2 domain move to form a single a domain and switch from a domain to a c domain..... 131

Figure 7.7. Hysteresis loop of combination of a_1 - a_2 domain of Fe film under various applied electric field values. 132

Figure 7.8. (a) The hysteresis loops of the Fe film during application of the out-of-plane electric field, which ranges from zero to $E = + 4$ kV/cm, and reaches to $E = + 6$ kV/cm. (b) The dependence of the remnant magnetization and the coercivity value to to the applied electric field values. (c) Relation between the shearing strain on the BTO surface to the magnetic anisotropy of the Fe film. 133

Figure 7.9. (a) Experimental polar plots of squareness ratio of the Fe film at the out-of-plane E of $E = + 6$ kV/cm. (b) The schematic illustration of the domain configuration in the Fe/BTO (right-hand side) at RT at the applied E of 6 kV/cm. The angles between the applied magnetic field (H) and the domain wall is represented by α . The magnetic anisotropies axes of Fe film are depicted with double-headed arrows, the arrows in the bottom schematic indicate the BTO polarization direction. (c) In-plane magnetic hysteresis loop of multiple c - a_2 Fe domains with applied H at different angles during application of $E = 6$ kV/cm. 135

Figure 7.10. (a) FE domain configuration of the BTO substrate after removing electric field (b) Experimental polar plots of squareness ratio of the Fe film after removing the out-of-plane electric field of $E = + 6$ kV/cm. (c) In-plane magnetic hysteresis loop of single c and a_2 domains of Fe film with applied magnetic field at different magnetic field angles under zero electric field..... 137

Figure 7.11. Electric field control of magnetic anisotropy of Fe/BTO..... 138

Figure 8.1. The schematic illustration of the in-plane lattice structure and ferroelectric polarization direction of the BTO substrate and the orientation of the Fe film on the a and c BTO domains. For full strain transfer from BTO substrate into the Fe film, the calculated lattice mismatch strain is estimated. The arrow and dot note in BTO unit cell depicts the ferroelectric polarization direction. 146

Figure 8.2. (a) Experimental polar plots of squareness ratio (M_R/M_S) and the magnetic switching fields (H_C) of the Fe film on a and c domains. (b) Magnetic hysteresis loop of single a (black curve) and single c (red line) domain measured at $\alpha = 45^\circ$. (c) Schematic illustration of ferromagnetic domain configuration of Fe/BTO film. The arrows indicate the direction of ferroelectric polarization, and the double-headed arrows represent the magnetic easy axes. 148

Figure 8.3. (a) Polarization microscopy images of the ferroelectric (BTO) during the application of an out-of-plane electric field. (b) The Kerr microscopy images of epitaxial Fe film on BTO for different applying electric field (corresponding to BTO domain configuration shown on (a)). (c) Magnetic hysteresis curves of a-c stripe domains measured at different electric field level. (d) Experimental polar plots of a squareness ratio of the Fe film under applied out-of-plane electric field of $E = 5$ kV/cm. 150

Figure 8.4. (a) The evolution of the single c domain under parallel and antiparallel out-of-plane electric field modulating from 0 to -5 kV/cm. The voltage rises at a rate of 1 V/min. The c+, c- with the dots and x marks denote the domain having the out-of-plane and anti-parallel-out-of-plane polarization direction pointing out and in the paper plane, respectively. The a_2 represents the in-plane domain having the polarization directions shown by the arrows. (b) Schematic illustration of the ferroelectric domain configuration under antiparallel out-of-plane electric field..... 152

Figure 8.5. The interpretation of the strain state induced on the Fe film by the BTO domain surface at their interface during a 180° domain switching process under the application of an antiparallel electric field. 153

Figure 8.6. (a) Coercivity dependent of applied electric field value on 180° domain-switching process. (b) Strain – Electric field hysteresis loop of ferroelectric material with the butterfly loop. 154

LIST OF TABLES

| | |
|---|----|
| Table 2.1. Piezoelectric coefficients for BTO single crystal and polycrystalline ceramic. | 35 |
| Table 5.1. Summarized Overview of all parameters..... | 86 |

TERMS AND ABBREVIATIONS

| | |
|----------------|---|
| FE | Ferroelectric |
| FM | Ferromagnetic |
| MFs | Multiferroics |
| ME | Magnetoelectric |
| E | Electric field |
| H | Magnetic field |
| M | Magnetization |
| H _C | Coercivity field |
| M _S | Saturation Magnetization |
| M _R | Remnant Magnetization |
| BTO | Barium titanate (BaTiO ₃) |
| MOKE | Magneto-optical Kerr effects |
| VSM | Vibrating Sample Magnetometer |
| MBE | Molecular-Beam-Epitaxy |
| XRD | X-ray diffraction |
| RHEED | Reflection high-energy electron diffraction |

CHAPTER 1: INTRODUCTION

1.1 Description of the research

In recent years, the Fe/BaTiO₃ (BTO) heterostructure has emerged as a highly promising candidate in multiferroics researches. This is primarily due to the magnetization at interface layer in Fe/BTO film can be electrically and reversibly switched on and off at room temperature by reversing the BTO polarization.[1] Several research groups have reported intriguing kinks or jumps in the temperature dependence of magnetic properties in the Fe films, correlating with structural changes in BTO.[2-6] This behavior signifies alternation in magnetic anisotropies induced by the different strain states imposed by the phase transition of BTO. Moreover, many studies have demonstrated that the magnetic anisotropy of Fe film on BTO also can be controlled by an electric field. [7-10] Underlying principle in these studies is the inverse piezoelectric effect observed in Fe/BTO composite, where elastic strain is transferred from the piezoelectric BTO substrate into the ferromagnetic Fe film.

However, the finding from these studies do not meet the requirements for applications on the spintronic devices. A study by of Venkataiah Gorige et al. have demonstrated strain-mediated 180° magnetization reversal in the Fe/BTO heterostructure through BTO phase transitions, albeit using a polycrystalline film.[11] Consequently, the film quality in this report may limit the achievement of strong magnetoelectric coupling at the film interface. A similar limitation is evident in researches employing electric means, where electric field manipulation of the Fe magnetic state in Fe films deposited on BTO resulted in only 40% in changes in the coercive magnetic field at room temperature.[12] This level of control poses a challenge for application in multiferroics devices.

Notably, a report by Lahtinen et al. has provided evidence of strong magnetoelectric coupling, demonstrating the transfer of ferroelectric-to-ferromagnetic pattern transfer from the BTO into the Fe films.[7, 13-15] In this scenario, the ferroelastic domain structure of BTO consists of stripes with both the in-plane (a_1 , a_2 -domain) and out-of-plane (c-domain) polarization. These different substrate domain types induce varying strain levels, which can modify the magnetic anisotropy of the film grown on the BTO. The mechanism here is based on strong elastic coupling between magnetic and ferroelectric domain walls in multiferroic heterostructures, leading to modify the magnetic domain patterns. Consequently, the Fe film shows a uniaxial lattice magnetic easy axis on in-plane BTO domain and biaxial magnetic one on out-of-plane BTO domains. This results is due to the full strain transfer from the substrate to the continuous films.

This thesis aims on providing the comprehensive understanding of how the magnetic states of Fe epitaxial films can be controlled via strain induced magnetoelectric coupling at interface of Fe and BTO. To begin, we conducted an in-depth study of BTO domain-switching criteria. Our research demonstrates the formation of a single in-plane domain by applying an out-of-plane electric field on the stripe domains of BTO at room temperature. These findings provide the insightful scenario of the polarization-dependent electric field of ferroelectric materials. Subsequently, this thesis explores the control of the magnetic states of Fe film grown on BTO substrate. We also investigate the electric field control of magnetic anisotropy and domain wall motion of Fe film on BTO stripe domains. The Fe epitaxial films were grown on the BTO (001) substrate using molecular-beam epitaxial (MBE) at ultra-high vacuum chamber. The structural properties of samples have been investigated by XRD, and RHEED pattern. The magnetic properties were studied using VSM and MOKE devices.

1.2 Thesis outlines

This dissertation includes nine chapters, which are briefly introduced as follows:

Chapter 1 shows introduction about thesis.

Chapter 2 presents the background theory related to this works, focusing on the magnetic energies and the effect of elastic strain on domain wall motion.

Chapter 3 reviews the research on multiferroic materials so far. Some of unsolved question in future are also presented.

Chapter 4 mentioned about the experiment techniques used in this works. It includes growth samples method, measurement methods on microstructural characterization and magnetic characterization.

Chapter 5, 6, 7 and 8 are experimental chapters.

Chapter 5 studies the effect of phase transition BTO and thermal strain on Fe films. Magnetic anisotropy of Fe films is controlled by strains induced from these schematic.

Chapter 6 shows the insightful understanding on P-E hysteresis loop of ferroelectric BTO single crystal using polarized light microscope.

Chapter 7, 8 shows magnetic anisotropy switching by polarization switching of Fe film on in-plane a_1 - a_2 and alternating a-c stripe domain of BTO under applying electric field.

Chapter 9 summarizes this dissertation and also shows some future works.

1.3 References

- [1] G. Radaelli *et al.*, “Electric control of magnetism at the Fe/BaTiO₃ interface,” *Nat. Commun.*, vol. 5, pp. 1–9, 2014.
- [2] M. Weisheit, S. Fähler, A. Marty, Y. Souche, C. Poinsignon, and D. Givord, “Electric field-induced modification of magnetism in thin-film ferromagnets,” *Science (80-.)*, vol. 315, no. 5810, pp. 349–351, 2007.
- [3] E. Güler and M. Güler, “A benchmark for some bulk properties of bcc iron,” *Int. J. Multiphys.*, vol. 7, no. 2, pp. 95–100, 2013.
- [4] S. Jia, X. Li, G. Li, S. Xie, and Y. Chen, “Epitaxial growth of (111) BaTiO₃ thin films on (0002) GaN substrates with SrTiO₃/TiN buffer layers,” *J. Mater. Sci. Mater. Electron.*, vol. 30, no. 10, pp. 9751–9757, 2019.
- [5] D. Cao, M. Q. Cai, W. Y. Hu, and C. M. Xu, “Magnetoelectric effect and critical thickness for ferroelectricity in Co/BaTiO₃/Co multiferroic tunnel junctions,” *J. Appl. Phys.*, vol. 109, no. 11, pp. 6–10, 2011.
- [6] Yin Y W, Burton J D, Kim Y M, Borisevich A Y, Pennycook S J, Yang S M, Noh T W, Gruverman A, Li X G, Tsymbal E Y and Li Q 2013 *Nat. Mater.* 12 397
- [7] T. H. E. Lahtinen, K. J. A. Franke, and S. Van Dijken, “Electric-field control of magnetic domain wall motion and local magnetization reversal,” *Sci. Rep.*, vol. 2, pp. 1–6, 2012.
- [8] G. Venkataiah, Y. Shirahata, I. Suzuki, M. Itoh, and T. Taniyama, “Strain-induced reversible and irreversible magnetization switching in Fe/BaTiO₃ heterostructures,” *J. Appl. Phys.*, vol. 111, no. 3, 2012.

- [9] Y. Shirahata, T. Nozaki, G. Venkataiah, H. Taniguchi, M. Itoh, and T. Taniyama, “Switching of the symmetry of magnetic anisotropy in Fe/BaTiO₃ heterostructures,” *Appl. Phys. Lett.*, vol. 99, no. 2, pp. 98–101, 2011.
- [8] S. Brivio, D. Petti, R. Bertacco, and J. C. Cezar, “Electric field control of magnetic anisotropies and magnetic coercivity in Fe/BaTiO₃ (001) heterostructures,” *Appl. Phys. Lett.*, vol. 98, no. 9, pp. 0–3, 2011.
- [10] S. Sahoo, S. Polisetty, C. G. Duan, S. S. Jaswal, E. Y. Tsymlal, and C. Binek, “Ferroelectric control of magnetism in BaTiO₃/Fe heterostructures via interface strain coupling,” *Phys. Rev. B - Condens. Matter Mater. Phys.*, vol. 76, no. 9, pp. 3–6, 2007.
- [11] T. H. E. Lahtinen and S. Van Dijken, “Temperature control of local magnetic anisotropy in multiferroic CoFe/BaTiO₃,” *Appl. Phys. Lett.*, vol. 102, no. 11, 2013.
- [12] S. Brivio, C. Rinaldi, D. Petti, R. Bertacco, and F. Sanchez, “Epitaxial growth of Fe/BaTiO₃ heterostructures,” *Thin Solid Films*, vol. 519, no. 17, pp. 5804–5807, 2011.
- [13] L. Bocher *et al.*, “Atomic and electronic structure of the BaTiO₃/Fe interface in multiferroic tunnel junctions,” *Nano Lett.*, vol. 12, no. 1, pp. 376–382, 2012.
- [14] T. H. E. Lahtinen, J. O. Tuomi, and S. Van Dijken, “Pattern transfer and electric-field-induced magnetic domain formation in multiferroic heterostructures,” *Adv. Mater.*, vol. 23, no. 28, pp. 3187–3191, 2011.
- [15] T. H. E. Lahtinen *et al.*, “Alternating domains with uniaxial and biaxial magnetic anisotropy in epitaxial Fe films on BaTiO₃,” *Appl. Phys. Lett.*, vol. 101, no. 26, pp. 1–5, 2012.

CHAPTER 2: THEORETICAL BACKGROUND

I. MAGNETISM

2.1 Magnetism and magnetic materials

The origin of magnetism is first understood in a free atom, where a magnetic dipole moment is inherently present even in the absence of an external magnetic field. This intrinsic magnetism can be attributed to the electronic structure within the free atom, as depicted in Fig. 2.1. In free atoms, unpaired electrons orbit the nucleus in atomic orbitals, giving rise to orbital angular momenta, which, in turn, generate the atomic magnetic moment. This phenomenon is analogous to the magnetic field produced by circulating currents created by charged particles. Additionally, each individual electron possesses angular momentum, resulting in a 'spin' magnetic moment. Importantly, these magnetic moments stemming from electrons' orbital motion and spin can couple, a phenomenon known as spin-orbit coupling. This coupling extends to interactions among electrons' orbital motion and spin, giving rise to the total atomic magnetic moment.

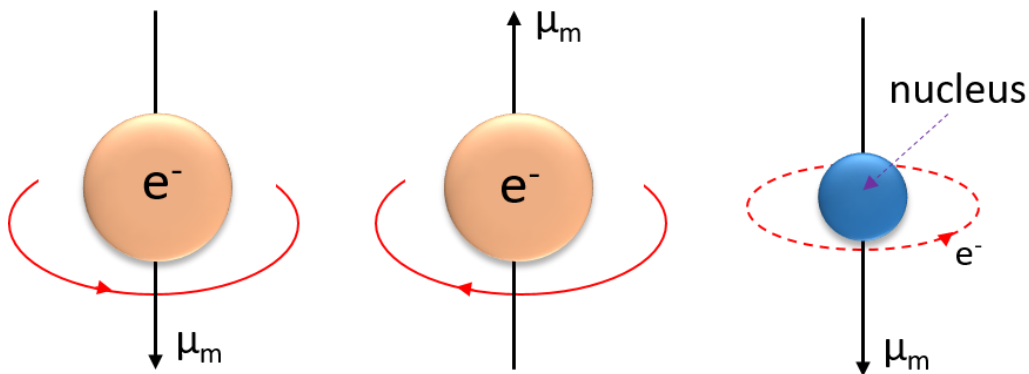


Figure 2.1. Schematic of the origin of magnetism from the electronic structure in a free atom.

After understanding the atomic origin of the magnetism, the next focus is on the magnetic materials, although only brief introduction is made expect for ferromagnetic materials.

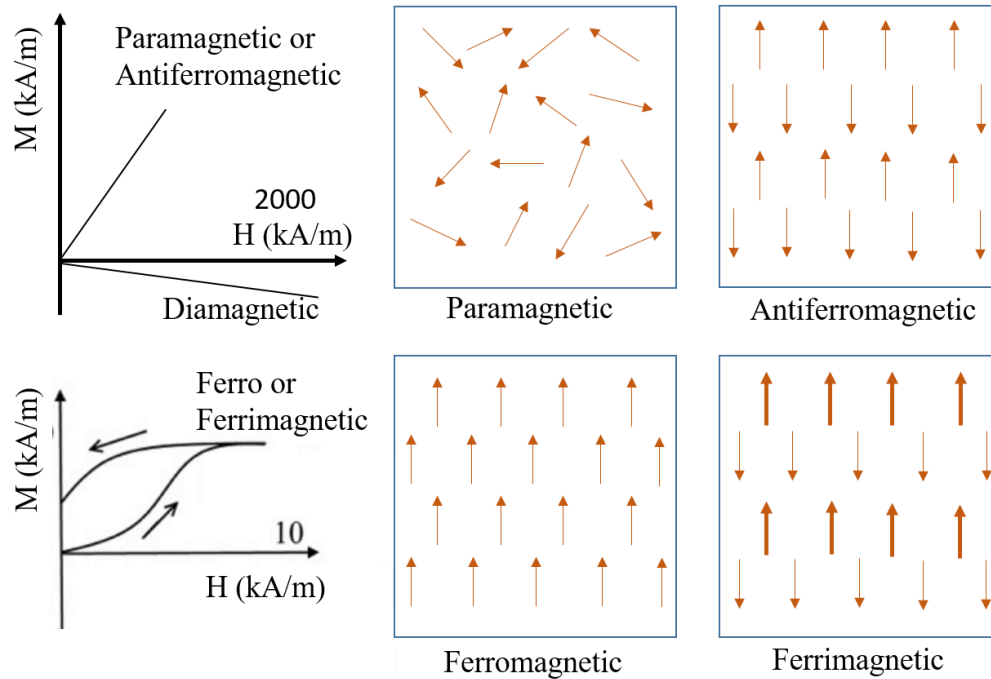


Figure 2.2. Schematic magnetization curves and magnetic ordering for magnetic materials

Diamagnetic materials are those that exhibit a diamagnetic response only in the presence of an external magnetic field. In fact, all materials demonstrate a weak diamagnetic response, but some magnetic materials display a stronger reaction to the applied field. Diamagnetic materials lack a net atomic magnetic moment, as their atomic orbitals are either completely filled or completely empty. The induced magnetic moment in the atom arises through electromagnetic induction and opposes the applied magnetic field, as depicted in Fig. 2.2. When the field is removed, the net magnetic moment returns to zero. Consequently, diamagnetic materials have limited applications due to their lack of a permanent magnetic moment. In contrast to diamagnetic materials,

paramagnetic materials possess net atomic magnetic moments, but these moments interact very weakly, leading to a random arrangement of magnetic moments due to thermal agitation, as shown in Fig. 2.2. When an external field (1000 kA/m) is applied, only a weak magnetization (0.5 kA/m) is observed. Similarly, paramagnetic materials have a limited range of applications. It's worth noting that ferromagnetic and ferrimagnetic materials transition to a paramagnetic state at temperatures above the Curie temperature (T_C).

Ferromagnetic materials offer a wide range of applications in modern device technologies for several reasons. Firstly, they exhibit a substantial magnetization strength (approximately 1000 kA/m) even under the influence of a relatively small external magnetic field (a few kA/m). This remarkable property arises from the robust interactions between atomic magnetic moments. These strong internal interactions overcome the effects of thermal energy, causing the magnetic moments to align parallel to each other and generate spontaneous magnetization, even in the absence of an external magnetic field. Additionally, the spontaneous magnetization tends to align along preferred directions, a characteristic associated with magnetocrystalline anisotropy (further details provided in Section 2.2.3). Secondly, ferromagnetic materials display hysteresis behavior in their magnetization (refer to Fig. 2.2), which means that the magnetization can persist, either fully or partially, even when the external magnetic field is completely removed. This feature presents significant opportunities for applications in information storage. The underlying reasons for this behavior can be comprehended through domain theory (discussed in Section 2.3.1) and the magnetization process (explained in Section 2.3.2).

Antiferromagnetic materials share similarities with ferromagnetic materials, but the crucial distinction lies in the exchange interaction between adjacent atoms, which results in the anti-

parallel alignment of atomic magnetic moments. Consequently, the magnetic fields cancel each other out, causing the material to exhibit behavior akin to that of a paramagnetic material. Similar to ferromagnetic materials, antiferromagnetic materials transition into a paramagnetic state above a specific temperature, known as the Néel temperature (T_N). Ferrimagnetic materials resemble antiferromagnets to some extent, as their dipoles align in an antiparallel manner. However, the magnitudes of certain dipole moments are larger than others, resulting in the material possessing an overall net magnetic moment. Ferrimagnetic materials exhibit similar magnetization characteristics, including magnetic hysteresis behavior, as illustrated in Figure 2.2.

2.2 Model for Ferromagnetism

Ferromagnetism arises from a short-range “exchange interaction” which enables the neighbouring magnetic moments to align with each other. The Heisenberg model of ferromagnetism describes the exchange interaction with a Heisenberg Hamiltonian which is given by:

$$\mathbf{H}_{\text{exch}} = -J \sum_{i < j} \mathbf{S}_i \cdot \mathbf{S}_j \quad (2.1)$$

In the context of magnetism, atomic spins S_i and S_j represent neighboring atoms, while J stands for the exchange integral, which quantifies the strength of exchange interactions between these spins, considering the localized nature of electrons around the atom. When there's an overlap between electronic wave functions and correlation between electronic spins, it results in a magnetically ordered state. However, the Heisenberg model predicts magnetic moment values as integer multiples of μ_B , and thus, it doesn't account for the experimentally observed non-integer magnetic moment values in transition metals like Fe, Co, or Ni. This discrepancy arises from the theory's reliance on localized electrons around atoms and its failure to consider itinerant electrons in metals.

This limitation is addressed by the "band theory," which proposes that available energy states for electrons exist as continuous energy bands rather than discrete energy values. These energy bands emerge from the interactions between mobile electrons in metals. In a non-magnetic metal, there is an equal density of states ($D(E_F)$) for both spin-up and spin-down electrons at the Fermi level. In the presence of an internal Weiss mean field ($\mathbf{H} = \lambda\mathbf{M}$), the centers of gravity of states characterized by opposite spins experience an energy separation.

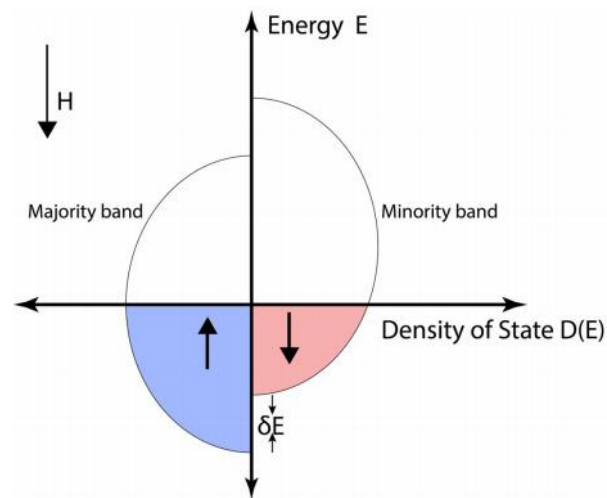


Figure 2.3. Schematic showing the density of states of 3d bands near Fermi level (E_F) in 3d transition metal. Splitting of spin-up and spin-down electron states at Fermi level giving rise to ferromagnetism. The δE is the energy gain per electron. [1]

Some of the electrons at the Fermi energy (E_F) undergo a spin-flip causing an imbalance of the so-called “minority band” and the “majority band” with “spin-up” and “spin-down”, respectively (Fig. 2.3). The spin-up and spin-down are defined with respect to a quantization direction which is chosen along the magnetic field H used to align the magnetization of sample.

The magnetization M is given by the difference in the number density of electrons (n_e) and holes (n_h) in the majority (*maj*) and minority (*min*), defined in Figure 2.3, according to:

$$|\mathbf{M}| = \mu_B(n_e^{maj} - n_e^{min}) = \mu_B(n_h^{maj} - n_h^{min}) \quad (2.2)$$

Therefore, an imbalance between spin-up and spin-down electrons gives rise to ferromagnetism in transition metal.

2.3 Magnetic energy

In Section 2.1, we provide a concise introduction to magnetic materials. We highlight that ferromagnetic materials exhibit robust magnetization in comparison to other forms of magnetism and feature magnetic hysteresis behavior, which grants them a diverse range of applications. This section also introduces the concept of magnetic energy in the context of the ferromagnetic system. Understanding magnetic energy is crucial for comprehending spontaneous magnetization, domain formation, domain wall structure, and magnetic anisotropy. Ferromagnetic domains are formed as a compromise to minimize the overall energy of the system (\mathbf{E}_{eff}) which is governed by the exchange energy (\mathbf{E}_{exch}), magnetoelastic energy (\mathbf{E}_d), Zeeman energy (\mathbf{E}_z) and the anisotropy energy (\mathbf{E}_{anis}).

$$\mathbf{E}_{eff} = \mathbf{E}_{exch} + \mathbf{E}_z + \mathbf{E}_d + \mathbf{E}_{anis} \quad (2.3)$$

The different energies compete with each other to orient the magnetization of a magnetic material in a certain direction. The final magnetization direction is determined by minimizing all these energy contributions described below.

2.2.1 Exchange energy

As discussed in Section 2.1, the exchange interaction between atomic magnetic moments causes them to align in parallel, minimizing the exchange energy (\mathbf{E}_e). In Equation 2.4, this energy pertains to the interactions between all nearest neighboring magnetic moment pairs within a unit volume.

$$\mathbf{E}_e = -J\mathbf{S}_i \cdot \mathbf{S}_j \quad (2.4)$$

Here, J represents the exchange constant, while \mathbf{S}_i and \mathbf{S}_j denote the spin vectors. It's evident that when the magnetic moments are aligned in parallel, \mathbf{E}_e reaches its minimum value. In a scenario where the ferromagnetic system is solely influenced by exchange energy, all magnetic dipoles align in the same direction. However, within a magnetic material, moments may not always be parallel due to various competing forms of energy that ultimately define the magnetic system.

2.3.2 Magnetostatic energy

Firstly, this section introduces the concept of the demagnetizing field (\mathbf{H}_d). When a magnetized magnet generates a magnetic field, it exerts a field in the opposite direction on the magnet itself, known as the demagnetizing field. This field contributes to the magnetostatic energy (\mathbf{E}_{ms}), which is calculated per unit volume using the following equation:

$$\mathbf{E}_{ms} = 1/2 \mu_0 \mathbf{H}_d \cdot \mathbf{M} \quad (2.5)$$

where the \mathbf{M} is the magnetization. A larger demagnetizing field will give a larger magnetostatic energy. The demagnetizing field H_d is proportional to the magnitude of the magnetization M , given by the equation:

$$\mathbf{H}_d = -N_d \mathbf{M} \quad (2.6)$$

Where the N_d is demagnetizing factor, which is determined by the sample geometry (the ratio of long axis and short axis). The N_d is ≤ 1 for all geometries. In terms of a two-dimension object, the demagnetizing factor N_d along a short axis is larger than along the long axis. As a result the demagnetizing field H_d is larger along a short axis. For a three-dimension object, there are N_{dx} , N_{dy} and N_{dz} along three directions respectively and also $N_{dx} + N_{dy} + N_{dz} = 1$. The equation (2.5) can be rewritten in terms of N_d :

$$\mathbf{E}_{ms} = 1/2 \mu_0 N_d \mathbf{M}^2 \quad (2.7)$$

The short axis will have a higher E_{ms} , thus the magnetization more likely to lie along the long axis, as it has the lower E_{ms} . Thus the short axis known as the hard axis and the long axis known as the easy axis when the shape anisotropy is dominant in a magnetic system. For example, in a film system, the easy magnetization direction is within the film plane while the hard magnetization direction is normal to the film plane due to the large shape anisotropy.

For a prolate rod shape, the E_{ms} is given:

$$\mathbf{E}_{ms} = \mathbf{K}_s \sin^2 \theta + \dots \quad (2.8)$$

where K_s is the shape anisotropy constant and θ is the angle between the magnetization direction and the semi-major axis c of the rod. When the semi-major axis equals the semi-minor axis, the K_s is zero and the shape anisotropy disappears.

2.3.3 Magnetocrystalline energy

In ferromagnetic single crystals, magnetization tends to align along a specific crystallographic direction, referred to as the easy axis, which can be (100) or (111). When an external magnetic field is applied along this easy axis, it's relatively easy to saturate the magnetization. In contrast, other crystallographic directions require a stronger magnetic field to achieve saturation. The crystallographic direction that demands the highest field for saturation is called the hard axis, while other directions are considered intermediate axes. For instance, in body-centered cubic (bcc) iron, the easy directions consist of six cube edge orientations: [100], [010], [001], [-100], [0-10], and [00-1], whereas the hard directions include four body diagonal orientations: [111], [-111], [1-11], and [11-1]. Different ferromagnetic materials may exhibit distinct preferred crystallographic directions; for instance, in face-centered cubic (fcc) nickel, the easy direction is [111]. The anisotropy associated with crystal structure is known as magnetocrystalline anisotropy. Magnetocrystalline anisotropy energy (E_{mc}) quantifies the energy difference between saturating along the easy axis and saturating along the hard axis. This anisotropy energy also represents the energy required to deviate the magnetization from the easy direction. In cubic crystals like iron, E_{mc} can be expressed as follows:

$$E_{mc} = K_1(\alpha_1^2\alpha_2^2 + \alpha_2^2\alpha_3^2 + \alpha_3^2\alpha_1^2) + K_2(\alpha_1^2\alpha_2^2\alpha_3^2) + \dots \quad (2.9)$$

Where K_1 and K_2 are the anisotropy constants and α_i is a series of the direction cosines between the magnetization direction and the crystal axis. For a uniaxial anisotropy energy in hexagonal crystals such as Cobalt (Co), the E_{mc} can be given:

$$E_{mc} = K_0 + K_1\sin^2\theta + K_2\sin^4\theta + \dots \quad (2.10)$$

where K_0 , K_1 and K_2 are the anisotropy constants and θ is the angle between the magnetization vector and the magnetocrystalline easy axis.

2.3.4 Magnetoelastic energy

Magnetoelastic energy, also known as magnetostrictive energy, stems from the magnetostriction effect. Essentially, magnetostriction describes the change in length of a ferromagnetic material when subjected to an external magnetic field. Some materials, like Fe, exhibit positive magnetostriction, causing them to elongate in the direction of the magnetic field, while others, like Ni, display negative magnetostriction, resulting in contraction along the magnetic field direction. These changes in length are typically quite small, in the range of tens of parts per million (ppm). In ferromagnetic systems, numerous orientation domains exist (as discussed in Section 2.3.1), and they tend to elongate or contract along different directions. These changes cannot occur simultaneously, leading to the generation of magnetoelastic energy. Additionally, external stress can induce variations in magnetoelastic energy, influencing the magnetization process. This is a crucial factor that allows piezoelectric strain, generated by an electric field, to control magnetization in ferromagnetic films. More comprehensive details will be provided in Section 2.3.3. The expression for magnetoelastic energy (E_{me}) is as follows:

$$E_{me} = -3/2\lambda_s\sigma\cos^2\theta \quad (2.11)$$

where λ_s is the saturation magnetostriction constant, σ is the external stress, and θ is the angle between the saturation magnetization (M_s) and the stress (σ).

2.4 Magnetization in Ferromagnets

2.4.1 Magnetic domains and domain walls

It is necessary to introduce the origin of ferromagnetic domains and domain barriers in order to comprehend the magnetization process in ferromagnetic materials. Ferromagnetic domains are the tiny areas seen in ferromagnetic materials where all of the atomic magnetic dipoles are aligned parallel to one another. From one domain to another, the overall direction of magnetization varies [9]. In order to reduce the overall magnetic energy inside a ferromagnet, domains arise. Due to the reduced demagnetizing effect, the ferromagnet's domain structure greatly reduces the magnetostatic energy (see section 2.2.2), even while it increases the exchange energy due to the unparallel magnetic moment alignment between the domains. As a result, the system's overall magnetic energy is reduced. A domain wall is the line that separates two neighboring domains, much like a grain border. A balance between the various contributions of magnetic energy determines the creation of domain barriers. Because there is a gradual change rather than a sudden transition between each magnetic moment, a wide domain wall will decrease the exchange energy contribution. The magnetic moments of a 180° domain wall, for instance, will rotate progressively from 0° to 180° . However, because there are more magnetic moments that are not along the favored crystallographic directions, the wide domain wall will also increase the magnetocrystalline energy contribution (see section 2.2.3). Conversely, a narrow wall will increase the exchange energy but decrease the magnetocrystalline energy, thus the total energy is optimized between the two energies (Fig. 2.4).

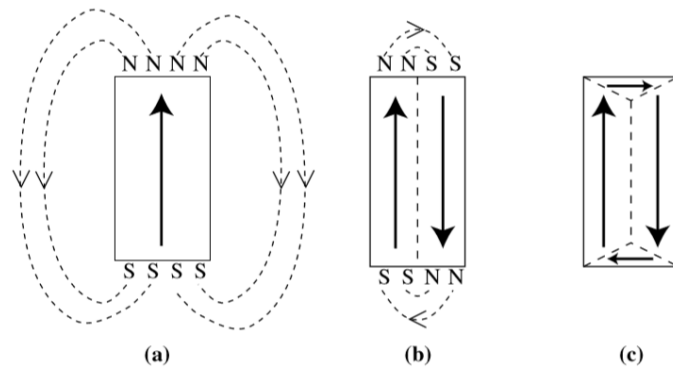


Figure 2.4. Reduce of the magnetic energy by domain formaton in ferromagnet. [2]

2.4.2 Magnetization process

In summary, at every level of magnetization (M), both domain wall motion and domain rotation are involved in the magnetization process and can happen simultaneously when subjected to an external magnetic field. All domains are first placed randomly in the demagnetized condition with zero applied field, and the total magnetization is cancelled to zero. The domain walls will begin to shift in response to the application of a magnetic field, causing some domains those with spontaneous magnetization closest to the applied field direction to expand. Consequently, the remaining regions whose spontaneous magnetization is not aligned with the direction of the applied field get increasingly smaller.

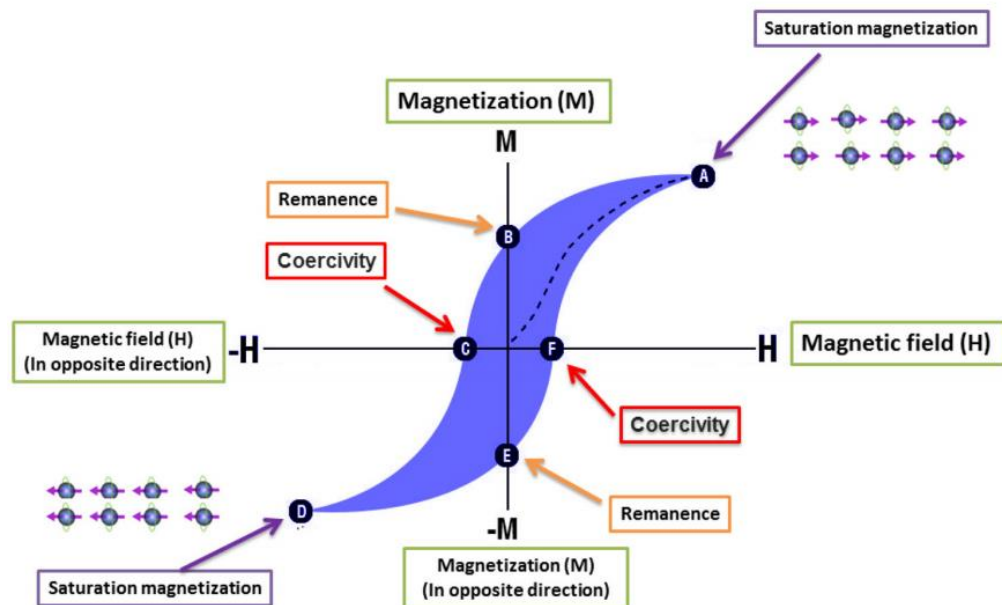


Figure 2.5. Magnetic hysteresis loop for a ferromagnets [3]

Domain wall pinning can occur when the domain wall encounters material flaws during the motion process. The domain wall motion needs energy from the external field in order to overcome the pinning sites. Due to a discontinuous domain wall motion, there is a sudden change in the magnetization once the domain walls separate. Then, as the field continues to grow, it will finally remove every domain wall, leaving only one inside the material. The magnetization approaches saturation (M_s) when the magnetic field is further increased to the point of saturation (H_s). This causes the magnetic moments in the single domain to rotate from the magnetization easy axis to the applied field direction. The magnetocrystalline anisotropy causes the magnetic moments to rotate back to their initial easy magnetization direction when the magnetic field is removed. Nevertheless, because of material flaws, the demagnetizing field is insufficient to break through the energy barrier that the domain walls face, preventing them from always returning to their

original places. Attained is a remanent magnetization state (M_r). As a result, Fig. 2.5 illustrates the magnetization's hysteresis characterisation. A magnetic field in the opposite direction - the coercivity field, or H_c must be supplied in order to completely eliminate the magnetization.

2.4.3 The effects of elastic stress

The concept of magnetoelastic energy was introduced in section 2.2.4. Elastic stress may influence the magnetization process if the magnetoelastic energy is greater than the other energies present in the material (see section 2.3.2). For instance, the random grain arrangement in polycrystalline magnetic films results in no preferred orientation and a small magnetocrystalline anisotropy energy. The inverse magnetostrictive effect is the term used to describe how elastic stress affects magnetization. A new anisotropy will emerge from the applied elastic stress, competing with the existing anisotropies and changing the domain structure. Equation 2.12, which represents the magnetoelastic energy minimizing in the magnetic system, provides an understanding of how elastic stress affects magnetization.

Remember the energy density of magnetic strain:

$$E_{me} = -3/2\lambda_s\sigma\cos^2\theta \quad (2.12)$$

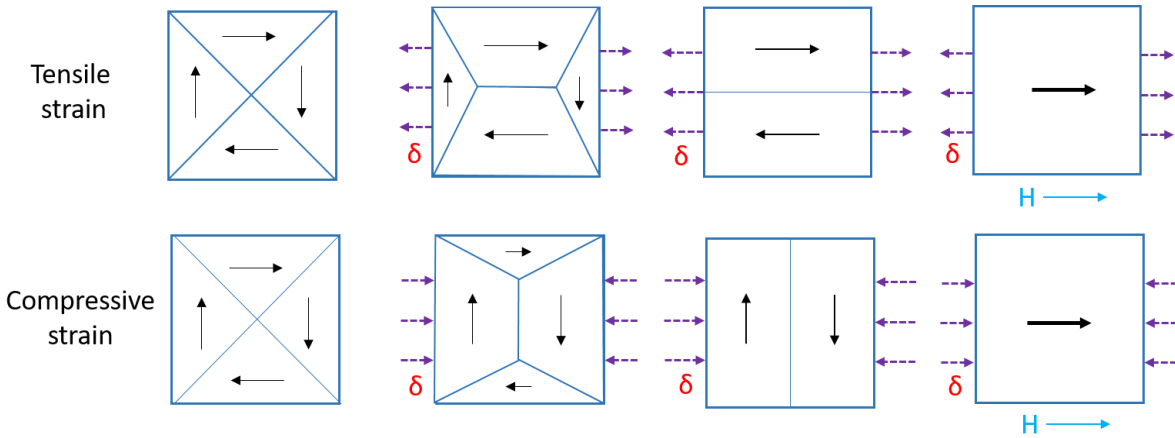


Figure 2.6. Schematic representation: the strain (top) and stress (bottom)-induced domain reorientation, 90/180° domain wall and magnetization direction.

Tensile ($\sigma > 0$) alignment with the saturation magnetization results in a minimum energy for $\theta = 0$ for iron, for example, where λ_s is positive. Despite the complexity of the domain structure, Fig. 2.6 provides a schematic representation of the stress-induced domain reorientation in a single crystal when a small portion of the sample with four domains is taken into consideration. This arrangement presupposes that domain wall motion is the only mechanism causing variation in magnetization. As a result, there are two different types of domain walls: 180° and 90°. Consequently, tension improves the magnetization by increasing the volume of domains magnetized parallel to the tensile stress axis. However, the process reverses and the magnetization decreases when σ is negative. A lower field will be needed to saturate the preferred magnetization direction that the tensile stress produces. However, in order to rotate the magnetic moments 90 degrees into the field direction, a higher magnetic field is needed when a compressed stress is applied. In actuality, the stress field and magnetic field work together to move the domain wall during the magnetization process (see section 2.3.2).

II. PIZOELECTRIC - FERROELECTRICITY

2.5 Polarization in Ferroelectricity

2.5.1 Piezoelectric effect

Pierre and Jacques Curie made the discovery of piezoelectricity in 1880. The first thing that was noticed was that when a mechanical stress was applied, a dielectric charge would appear on the crystal. The property of a material that displays electric charge on its surface when an external mechanical stress is applied (i.e., changes its polarization) is known as the direct piezoelectric effect (Fig. 2.7a). The opposite piezoelectric effect (Fig. 2.7b) results in a mechanical strain as a result of polarization shifting.[2]

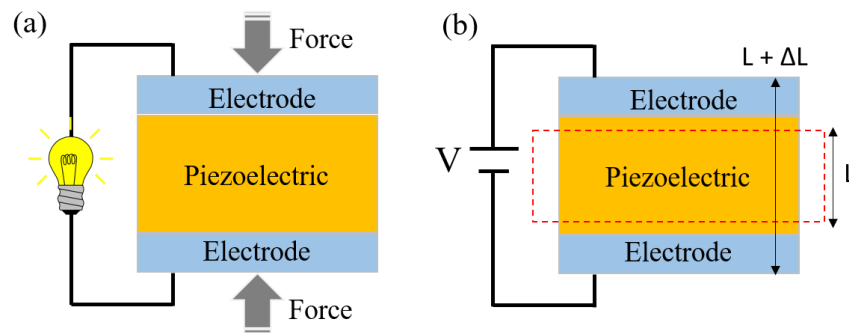


Figure 2.7. Direct piezoelectric effect (a) and converse piezoelectric effect (b)

Certain materials have the ability to produce an electric charge on their surface in response to mechanical stress. This property is known as piezoelectricity. These materials experience a linearly proportional strain when an electrical field is applied. The majority of materials with non-centrosymmetric crystal structures exhibit it. Quartz and tourmaline are two examples of naturally occurring crystalline materials with these characteristics. Lithium sulfate, ammonium dihydrogen phosphate, and Rochelle salt are a few artificially made piezoelectric crystals. Piezoelectric

ceramics are a different class of materials with these characteristics. The three types of piezoelectric ceramics that are most frequently produced are lead titanate (PTO), lead zirconate titanate (PZT), and barium titanate (BTO). The crystal structure of the BTO is derived from the perovskite family, which shares the general formula ABO_3 . In Figure 2.8, the ideal, cubic perovskite structure is shown. The BTO crystallites are centro-symmetric cubic (isotropic) above the Curie temperature and exhibit tetragonal symmetry (anisotropic structure) below the Curie temperature.

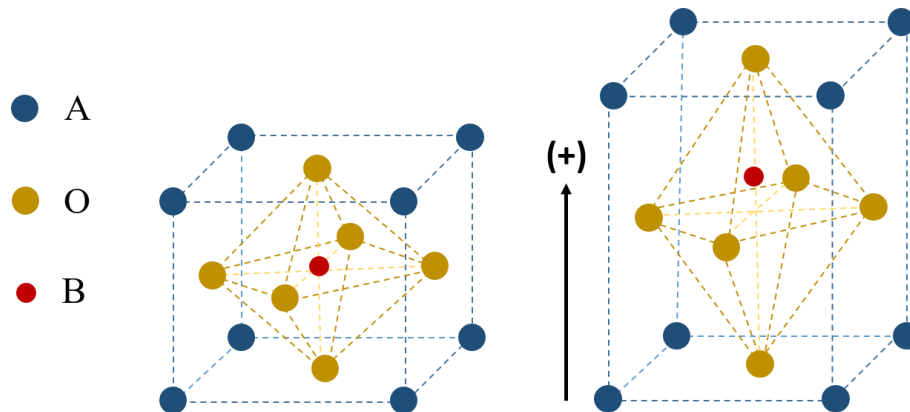


Figure 2.8. BTO crystal structure belonging to the perovskite family.

2.5.2 Phase transition and Ferroelectricity (BTO)

Ferroelectrics are polar materials that, in the absence of an electric field, have at least two equilibrium orientations of spontaneous polarization. The polarization vector's direction can be changed when an electric field is applied. As a result, ferroelectric materials exhibit nonlinear phenomena related to polarization reversal and are both piezoelectric and pyroelectric (the relationship between changes in temperature and polarization). The majority of ferroelectric materials transition into one or more ferroelectric phases of lower symmetry through a displacive

structural phase from a high temperature prototype phase, which is frequently centrosymmetric. As previously mentioned, the example for barium titanate (as illustrated in Fig. 2.8) is a member of the perovskite material family with general formula ABO_3 . Ba^{2+} is situated on the A-site at the corners of the cubic unit cell, whereas Ti^{4+} is situated on the B-site in the cell center. BO_6 octahedra are made up of the O^{2-} anions, which are found at the unit cell's face centers. From a crystallographic perspective, a shift in the Ti^{4+} and O^{2-} ions with respect to the Ba^{2+} ion at the origin is associated with the emergence of spontaneous polarization in barium titanate. The spontaneous polarization, or P_s , is the name given to the ensuing electric dipole moment. The appearance of spontaneous polarization is accompanied by changes in the dimensions of the unit cell. The strain relative to the cubic prototype due to these dimensional changes is termed the spontaneous strain.[3]

BTO goes through the following first-order phase transitions when cooled to room temperature: cubic (131 °C), tetragonal (0 °C), orthorhombic (-90 °C), and rhombohedral. These transitions correlate to the emergence of spontaneous polarization parallel to the pseudocubic unit cell of the perovskite structure's edge (tetragonal), followed by its reorientation along the orthorhombic face diagonal and the rhombohedral body diagonal (Fig. 2.9).

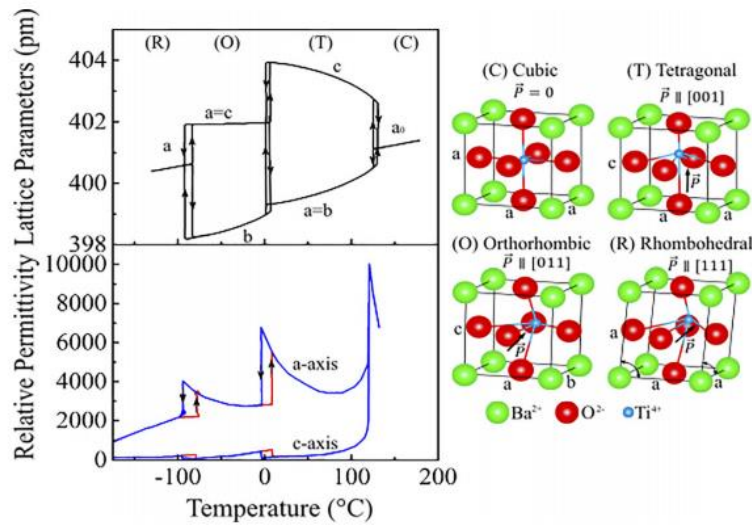


Figure 2.9. Changes in primitive-cell lattice parameters and anomalies in relative permittivity during the sequence of phase transition in BTO. The right side of figure illustrates the crystal structure of the cubic prototype phase and the unit cell distortions in each of the ferroelectric phase of BTO. [4]

2.5.3 Ferroelectric domains

Ferroelectrics and ferromagnets both form domains with uniformly polarized regions as a result of a depolarizing field that reduces electrostatic energy. The direction of the unit cell's elongation aligns with the ferroelectric polarization orientation. The c-axis of the tetragonal unit cell is where the spontaneous polarization in BTO occurs at room temperature, and the shifts of O and Ti ions with respect to Ba are typically used to characterize the crystal distortion. The crystal is spontaneously strained with $a = b = 3.996 \text{ \AA}$ and $c = 4.036 \text{ \AA}$ in the ferroelectric phase, where a, c are the axis on the tetragonal cell.[4] In most ferroelectric crystals, the spontaneous polarization is not uniformly aligned along the same direction throughout the material. When the crystal is cooled below the ferroelectric phase-transition temperature, spontaneous polarization can occur with

equal probability along any of the six directions along the three c-axis of the cubic cell in BTO. The sample's mechanical and electrical boundary conditions determine which direction the polarization will develop.

Ferroelectric domain walls are those that are oriented differently from the spontaneous polarization vector, while ferroelastic domain walls are those that are oriented differently from the spontaneous strain tensor. The 180° domain walls in BTO are exclusively ferroelectric since the polarization vector's orientation is the only difference between them. Because of the differences in the orientation of the polarization vector and spontaneous strain tensor, the 90° walls are both ferroelectric and ferroelastic. BTO has a tetragonal crystal structure with a difference lattice parameter of two tetragonal axes and a tetragonality of 1.1% at room temperature. The ferroelectric polarization aligns with the axis of the largest lattice parameter. Figure 2.10 illustrated three different domain patterns can form in tetragonal BTO (001)-oriented surface. On c_1 - c_2 domain pattern, the in-plane lattice structure of stripe domains with alternating up and down polarization is at cubic phase. The other domain patterns are characterized by 90° rotations of the ferroelectric polarization and corresponding changes of the in-plane lattice structure. Therefore, these type of domains present both ferroelectric and ferroelastic properties. For a_1 - a_2 domains pattern, the unit cell in (001)-oriented surface is rectangular in both domains, but the axis of unit cell elongation rotates by 90° at domain boundaries.[5]

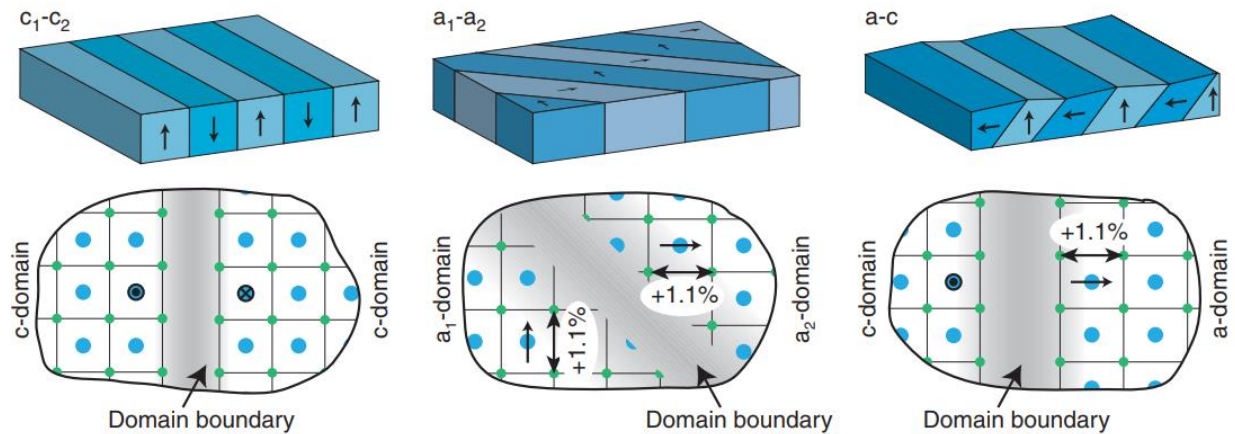


Figure 2.10. Schematic illustration of three possible domain patterns in tetragonal BaTiO₃ crystals with a (001)-oriented surface. [5]

The perovskite crystal structure of a variety of ferroelectric ceramics is depicted in Figure 2.11. In addition to the tetragonal phase, orthorhombic and rhombohedral structures are also present. The material is in the paraelectric state and the unit cell has a cubic, centrosymmetric structure above the Curie temperature. The material experiences a phase transition from cubic to tetragonal as it cools below T_C . Ti ion displacement's direction corresponds to the direction of the spontaneous polarization of the material, P_s , and is aligned with the long c -axis of the tetragonal cell. The material is both ferroelectric and piezoelectric below T_C , and the crystal's piezoelectric characteristics match the direction of spontaneous polarization. The material's elastic, dielectric, and piezoelectric responses are displayed on the first line of Figure 2.11. The polarization of the material and the strain are related to the position of Ti and the shape of the unit cell, respectively. Figure 2.11's ferroelectric response is displayed at the bottom. There are differences between

ferroelectric and ferroelastic switching. Strain only tailors the 90° switching; 180° and 90° switching can be made by the electric field.[6]

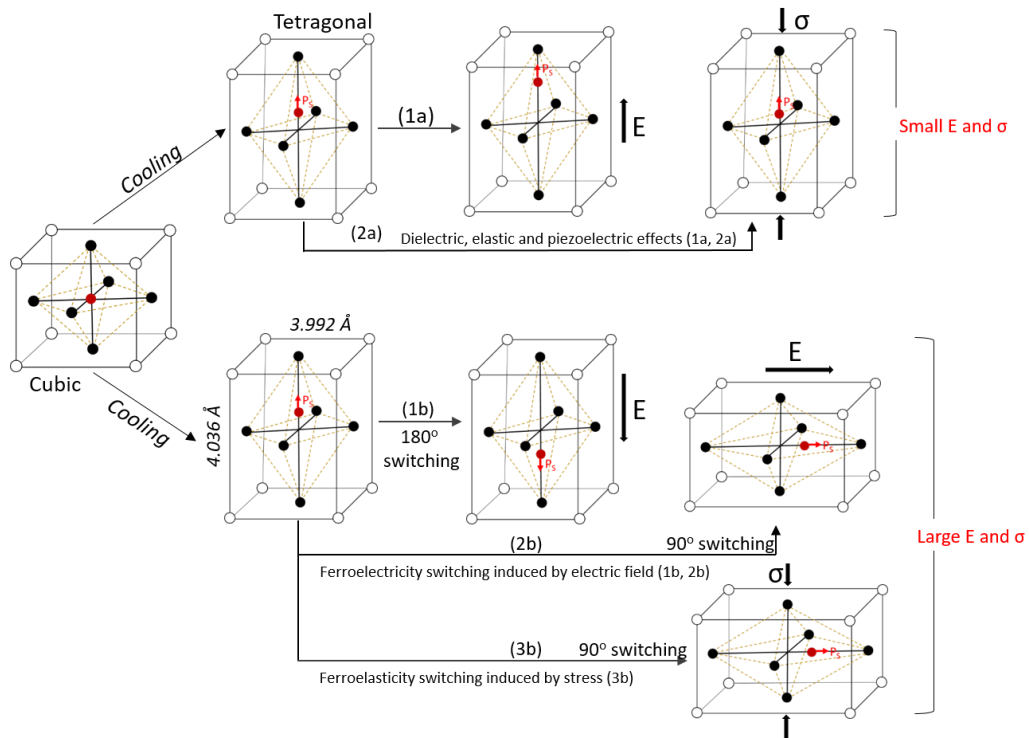


Figure 2.11. The perovskite crystal common to many ferroelectric ceramics. For BTO the white ions at the corners are Ba with a +2 charge, the black ions on the faces are oxygen ions with a -2 charge and the central ion is Ti with a +4 charge. The top of figures illustrates the phase change through the Curie temperature, the spontaneous polarization, and the linear response of the crystal. The bottom set of figures illustrates the spontaneous shape change of the crystal, and 180° and 90° switching due to applied electric field or stress.

The configuration of BTO's ferroelectric domain under temperature and electric field is depicted in Figure 2.12. The tetragonal ferroelastic domain orientation and the crystal phase (C: cubic, T: tetragonal). The polarization direction in the a_1 , a_2 , and c domains is along the in-plane, while that in the out-of-plane direction. Operations that change the observed domain states are indicated by arrows: The a_1 - a_2 in-plane polarization stripe domain is heated through T_C without voltage (V) (1), resulting in the cubic phase (paraelectric state). After cooling through T_C in the applied V , the polarization direction of BTO is parallel to the direction of the applied electric field at the tetragonal phase (2). When heating through T_C , all domain types will reach non-polarization at the cubic phase (3). Heating above 120 degrees. Applied V on a_1 - a_2 and a_1 - c stripe domain, their domains is modulated to c domain (4). Remove applied V , from c domain with polarization along to the electric field direction, the domains will be become a_1 - c stripe domains (5).

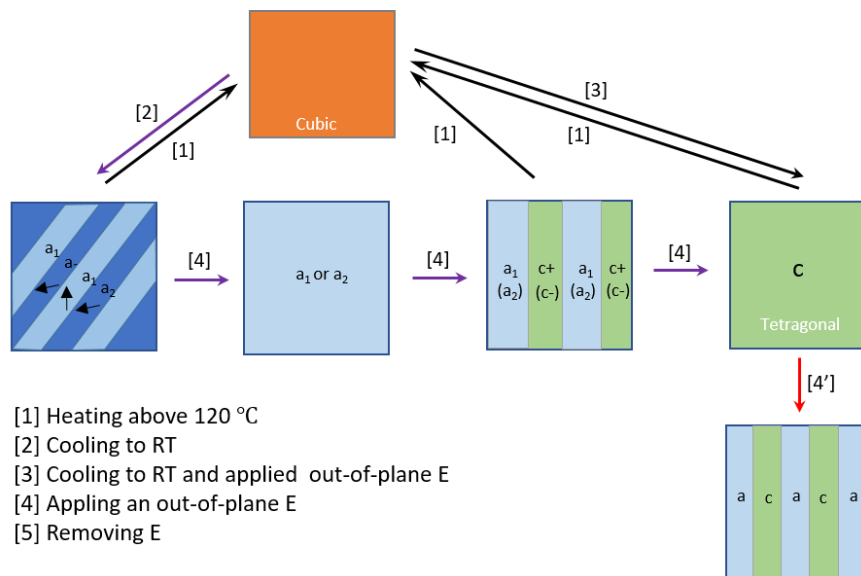


Figure 2.12. Schematic illustration of the unit cell shape of tetragonal BTO. The a -domain have in-plane polarization direction, and the c -domain have out-of-plane polarization direction.

2.5.4 Hysteresis and polarization switching (BTO)

A family of crystallographic directions with the lowest free energy will be the direction along which spontaneous polarization is oriented in the absence of external stimuli, such as an electric field or mechanical stress. For example, the spontaneous polarization vector in the room temperature tetragonal phase of BaTiO₃ will point in any of the six equivalent <100> directions. Areas with a consistent polarized orientation are known as ferroelectric domains. A domain wall designates the boundary between two domains.

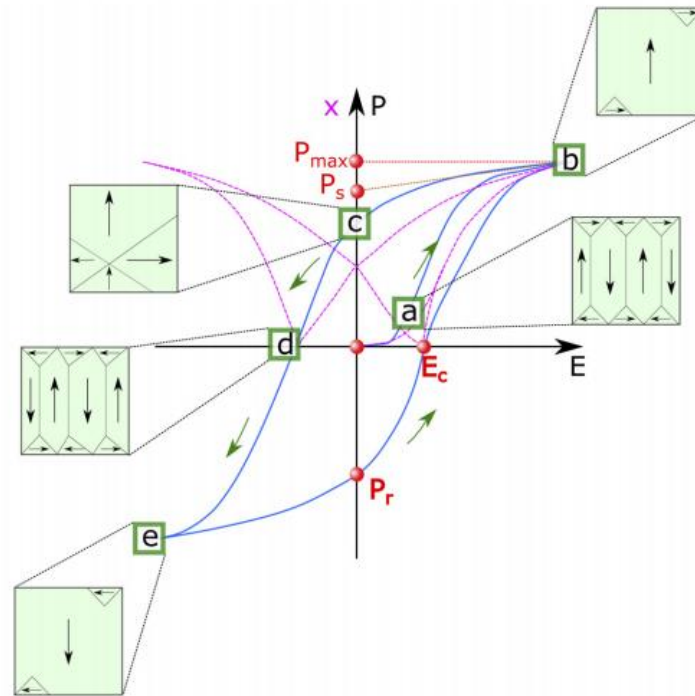


Figure 2.13. Polarization-electric field hysteresis loops of ferroelectric crystal with remanent polarization P_r and coercive field E_c where the polarization value of zero. (a), (b), (c), (d), and (e) represent different polarization configurations under an applied electric field. The strain-electric field butterfly loop is also shown here.[6]

The decrease in the elastic and electrostatic energies leads to the formation of domains in ferroelectric (FE) crystals. Walls that divide domains with parallel but opposing polarization directions are known as 180° domain walls. Non- 180° domain walls are those that divide domains whose polar vectors are oriented at a specific angle to one another. The ferroelectric crystal's polarization-electric field hysteresis loops are depicted in Figure 2.13. An FE material displays a random polydomain configuration when it is virgin, which results in a macroscopic polarization of zero. Due to intrinsic material response, the relationship between strain and polarization is almost linear at low electric field application (Fig. 2.13a). Domain walls may shift and cause domain switching when a strong enough external stimulus is applied, such as an electric field or mechanical stress. High electric fields caused the domain walls to orient at a saturation state along the field direction, which at that point restored a linear change in polarization with electric field, as seen in Fig. 2.13b. Following the removal of an applied electric field, some domain walls will backswitch, resulting in residual polarization that is non-zero macroscopic polarization, as shown in Figure 2.13c. Applying the electric field in the opposite direction is necessary to return the polarization to zero. The electric field's value is called the coercive field (Fig. 2.13d).[8]

2.5.5 Operating modes of piezo-materials

a. An introduction to stresses and strains

Normal stresses and strain

Stress refers to the local concentration of mechanical force within a material. Imagine a body experiencing equal and opposite forces applied to two of its faces (see Fig. 2.14). When these forces are applied perpendicular to a face (i.e., parallel to the face normal), as illustrated, the

resulting stress σ is known as normal stress. This stress can be either tensile (positive) or compressive (negative).

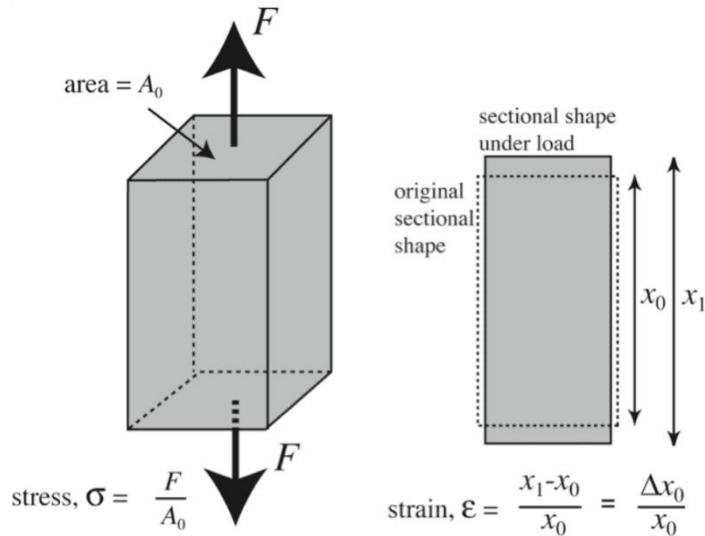


Figure 2.14. A cuboid under load by application of forces to a pair of opposing faces, to generate a normal stress, σ . [7]

As F increases and the material gradually deforms, the area being loaded will decrease. Consequently, at comparatively high strains, the true stress - which is determined by dividing the force by the current area - and the stress represented by F/A , also known as the nominal stress or engineering stress, differ considerably. The strain represents the material's reaction to the applied stress. The change in length along a given direction divided by the original length is known as the normal strain (ϵ) in that direction. Similar to stresses, this nominal or engineering strain and the genuine strain (defined as the change in length divided by the current length) can be distinguished from one another.

Shear stresses and strains

In order to create shear, forces are also possible to use parallel to two opposing faces of a body. Applying shear stresses in pairs is necessary for avoiding the body from rotating. In Fig. 2.15, this is demonstrated.

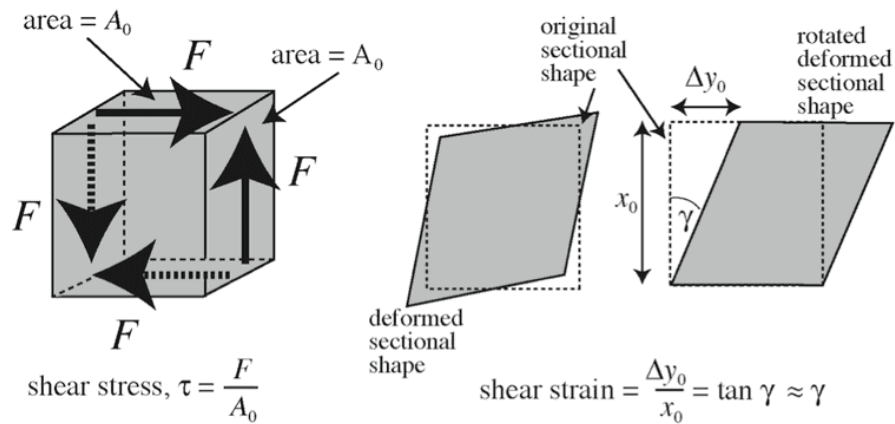


Figure 2.15. A cuboid under load by application of forces to two pairs of opposing faces, with the forces acting parallel to the faces, to generate a shear stresses, τ . [7]

b. Piezoelectric coefficient for BTO single crystal

Because a piezoelectric ceramic is anisotropic, physical constants relate to both the direction of the applied mechanical or electric force and the direction perpendicular to the applied force.

Consequently, each constant generally has two subscripts that indicate the directions of two related quantities, such as stress (force on the ceramic element / surface area of the element) and strain (change in length / original length) for elasticity. The direction of positive polarization usually is made to coincide with the Z-axis of a rectangular system of X, Y, and Z axes (Fig. 2.16). Direction of X, Y, and Z presented by the subscript 1, 2, or 3, respectively, and shear about one of these axes is represented by the subscript 4, 5, or 6, respectively. Definitions of the most frequently used constants, and equations for determining and interrelating these constants, are summarized here. The piezoelectric charge constant: d ; the piezoelectric voltage constant: g ; the permittivity: ϵ .

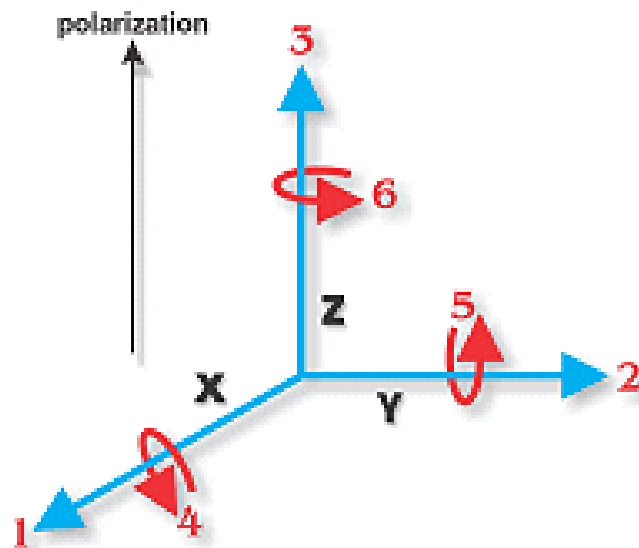


Figure 2.16. Direction of forces affecting a piezoelectric element. [8]

The piezoelectric charge constant, d , is the polarization generated per unit of mechanical stress (T) applied to a piezoelectric material or, alternatively, is the mechanical strain (S) experienced by a piezoelectric material per unit of electric field applied. The first subscript to d indicates the direction of polarization generated in the material when the electric field, E , is zero or, alternatively, is the direction of the applied field strength. The second subscript is the direction of the applied stress or the induced strain, respectively.

Example:

d_{33} : induced polarization in direction 3 (parallel to polarization direction) per unit stress applied in direction 3.

d_{31} : induced strain on direction 3 per unit stress applied in direction 1 (perpendicular of polarization direction).

d_{15} : induced polarization in direction 1 (perpendicular to polarization direction) per unit shear stress applied about direction 2 (perpendicular to polarization direction).

The piezoelectric voltage constant, g , is the electric field generated by a piezoelectric material per unit of mechanical stress applied or, alternatively, is the mechanical strain experienced by a piezoelectric material per unit of electric displacement applied. The first subscript to g indicates the direction of the electric field generated in the material, or the direction of the applied electric displacement. The second subscript is the direction of the applied stress or the induced strain, respectively.

The permittivity or dielectric constant, ϵ , is dielectric displacement per unit electric field. ϵ^T is the permittivity at constant stress, ϵ^S is the permittivity at constant strain. The first subscript indicates the direction of the dielectric displacement; the second is the direction of the electric field.

Elastic compliance, s , is the strain produced in a piezoelectric material per unit of stress applied and, for the 11 and 33 directions is the reciprocal of the modulus of elasticity (Young's modulus, Y). s^D is the compliance under a constant electric displacement; s^E is the compliance under a constant electric field. The first subscript indicates the direction of strain, the second is the direction of stress.

The basic piezoelectric coefficient for BTO single crystal and polycrystalline ceramic is shown in the table 2.1.

Table 2.1. Piezoelectric coefficients for BTO single crystal and polycrystalline ceramic.[9]

| | Crystal | Ceramic |
|------------------------------|---------|---------|
| d_{15} | 392 | 270 |
| d_{31} | -34.5 | -79 |
| d_{33} | 85.6 | 191 |
| g_{15} | 15.2 | 18.8 |
| g_{31} | -23.0 | -4.7 |
| g_{33} | 57.5 | 11.4 |
| k_{31} | 0.315 | 0.208 |
| k_{33} | 0.560 | 0.494 |
| k_{15} | 0.570 | 0.466 |
| $\epsilon_{11}^T/\epsilon_0$ | 2920 | 1436 |
| $\epsilon_{33}^T/\epsilon_0$ | 168 | 1680 |
| $\epsilon_{11}^S/\epsilon_0$ | 1970 | 1123 |
| $\epsilon_{33}^S/\epsilon_0$ | 109 | 1256 |
| S_{11}^E | 8.05 | 8.55 |
| S_{33}^E | 15.7 | 8.93 |

III. MULTIFERROIC MATERIALS

2.6 Multiferroic types

2.6.1 Types of ferroic ordering

Ferroelectrics

Ferroelectric materials are distinguished by a spontaneous electric polarization, P , that can be switched by an applied electric field, E , as was discussed in section 2.4.2. Ferroelectric P-E hysteresis loops are remarkably similar to ferromagnet M-H hysteresis loops. Both ferromagnetic and ferroelectric materials contain the domains. At a critical temperature (T_C), both the ferroelectric to paraelectric phase transition and the ferromagnetic to paramagnetic phase transition take place. Additionally, ferroelectrics have the piezoelectric effect, whereas ferromagnets have the piezomagnetic (magnetostriction) effect. But compared to the piezomagnetic effect, the piezoelectric effect is substantially greater. Piezoelectric effects can cause strains up to 10^3 parts per million in the former case, and piezomagnetic effects can cause strains up to 10 parts per million in the latter.

Regarding applications, hysteresis in ferromagnets and ferroelectrics can result in storage applications where the direction of either electric or magnetic polarization represents the "1" or "0" of the data bit. This hysteresis causes the spontaneous polarization to persist in the absence of an applied field. While magnetic materials dominate the market, for instance, in computer hard drives ferroelectrics have a few specialized uses and could see a rise in usage in next-generation information-storage technologies.

Ferroelastic

A material that exhibits switchable spontaneous deformation in response to applied stress is known as ferroelastic. In the absence of mechanical stress, ferroelasticity occurs when a material has two or more orientation states with identical crystal structures; mechanical stress will then favor one or the other and cause shifting between them.

Figure 2.17 illustrates an example where the cubic phase exists above the Curie temperature. The system is in the tetragonal phase below the Curie temperature. As we can see, in the absence of mechanical stress, the two low-temperature variants in Fig. 2.17 have the same energy. However, if a horizontal compress stress is applied, the left variant is preferred over the right, which changes into the left, and vice versa.

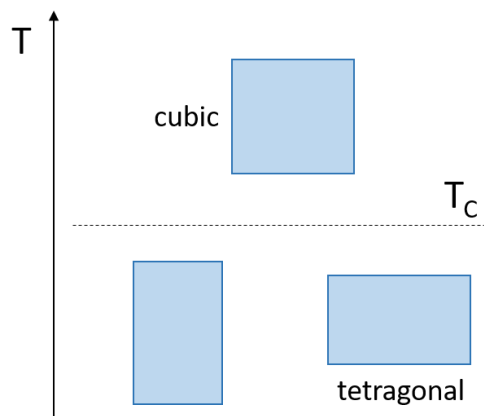


Figure 2.17. Schematic of a ferroelastic phase transition. As the temperature is cooled below T_C the cubic paraelastic structure undergoes a phase change to one of the degenerate tetragonal variants shown. A mechanical stress can be used to transform between the variants.

Ferrotoroidics

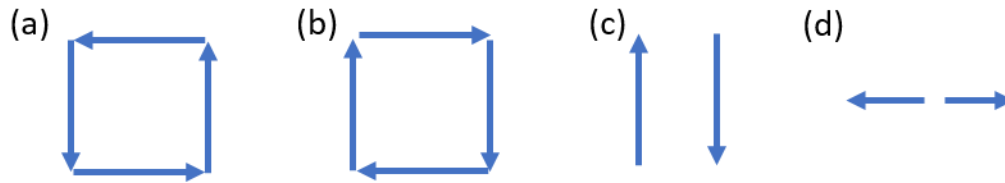


Figure 2.18. Simple arrangements of magnetic moments which can lead to toroidal moments. (a) and (b) have equal and opposite toroidal moments. The antiferromagnetic arrangement in (c) has toroidal moment, whereas that in (d) does not [19].

A "circular" or "ring-like" arrangement of spins, like the ones in Fig. 2.18, is typically linked to a magnetic toroidal moment. Ferrotoroidics change under both operations, whereas ferroelastics remain invariant under both space inversion and time reversal, and ferroelectrics and ferromagnets remain invariant under only the first or the second, respectively (Figure 2.19).

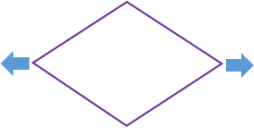
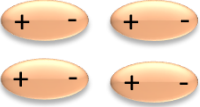
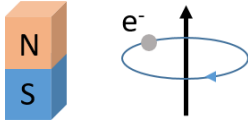
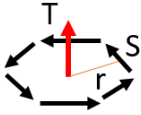
| Time \ Space | Invariant | Change |
|--------------|--|--|
| Invariant | Ferroelastic  | Ferroelectric  |
| Change | Ferromagnetic  | Ferrotoroidic  |

Figure 2.19. Forms of ferroic order and their transformation properties under the parity operations of spatial inversion and time reversal.

2.6.2 Multiferroic materials

Multiferroic ordering combines magnetic ordering with ferroelectricity, ferroelasticity, and ferrotoroidicity, three other types of ferroic ordering. The combination of ferroelectricity and magnetism, which is interesting due to its potential for magnetoelectric response - that is, the

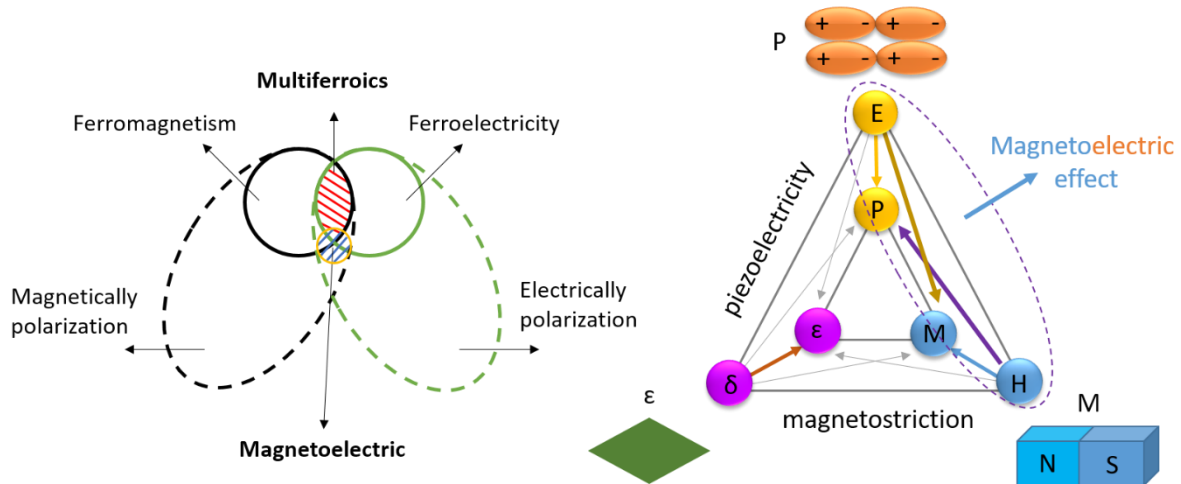


Figure 2.20. Multiferroic materials with the coexistence of the at least two ferroic properties.

ability to tune and control magnetism using an electric field - will be the main topic of this chapter. A material that exhibits two or more primary ferroic ordering simultaneously is defined as a multiferroic. The well-known basic ferroics are the ferromagnets, which can be switched by applying a magnetic field; the ferroelectrics, which can be switched by applying an electric field; and the ferroelastics, which can be switched by applying a mechanical stress causing a spontaneous strain (Figure 2.20).

a. Single-phase multiferroic materials

Ferroelectric polarization and ferromagnetic magnetization are both induced in the same phase by single-phase multiferroic materials. Thus, just as the ferroelectric polarization can be controlled by an applied magnetic field, so too can the magnetization be controlled by an applied electric field. Nevertheless, single-phase multiferroic materials are uncommon. The first discovered multiferroic material was nickel iodine boracite ($\text{Ni}_3\text{B}_2\text{O}_{13}\text{I}$) [10], although some other multiferroic boracite compounds were synthesized afterwards, such as $(1-x)\text{PbFe}_{0.66}\text{W}_{0.33}\text{O}_{3-x}\text{PbMg}_{0.5}\text{W}_{0.5}\text{O}_3$ (PFW-PMW), $\text{Pb}_2(\text{Co,W})\text{O}_6$ and $\text{Pb}_2\text{FeTaO}_6$, etc, multiferroic materials. For these synthesized multiferroic materials, they all show very low Curie or Neel temperature ($\ll 273$ K) [10]. Afterwards, significant progress was made on the study of various oxides, such Bi-based compounds (BiMnO_3 , BiFeO_3) and rare earth magnates (TbMn_2O_5 and YMnO_3). BiMnO_3 has a simple B site cation and is both ferromagnetic and ferroelectric due to the covalent bonding between Bi and O atoms. BiMnO_3 is ferromagnetic with a transition temperature at about 105 K and ferroelectric with Curie temperature at about 450 K. BiFeO_3 is antiferromagnetic with a high Neel temperature at 380 °C and ferromagnetic with a high Curie temperature at 810 °C [10]. The polarization and magnetization plane of BiFeO_3 are shown on Fig. 2.21.

Substitution of the A site cation yields rare earth (RE) perovskite manganite compounds (REMnO_3 , RE = Y, Ho, Er, Tm, Yb, Lu). It was recently found that multiferroic properties were also exhibited by the REMn_2O_5 family. Ferroelectric transition temperature and antiferromagnetic transition temperature in REMn_2O_5 compounds are approximately 25 K – 39 K and 39 K – 45 K, respectively [10–12]. As previously mentioned, bulk single-phase multiferroic materials have been extensively studied. Additionally, thin films of these materials (YMnO_3 , BiFeO_3 , and NiMnO_3) were obtained for use in contemporary multifunctional devices and other practical applications.[11-13]

Bulk and film versions of single-phase multiferroic materials have been extensively studied. In the majority of these materials, the magnetoelectric effect is only present below room temperature. However, single-phase materials face significant scientific challenges due to practical requirements like room temperature operation and strong magnetoelectric coupling between both ferroic order parameters. Consequently, there has been a lot of interest lately in multiferroic composites with stronger magnetoelectric coupling at room temperature and more design flexibility.

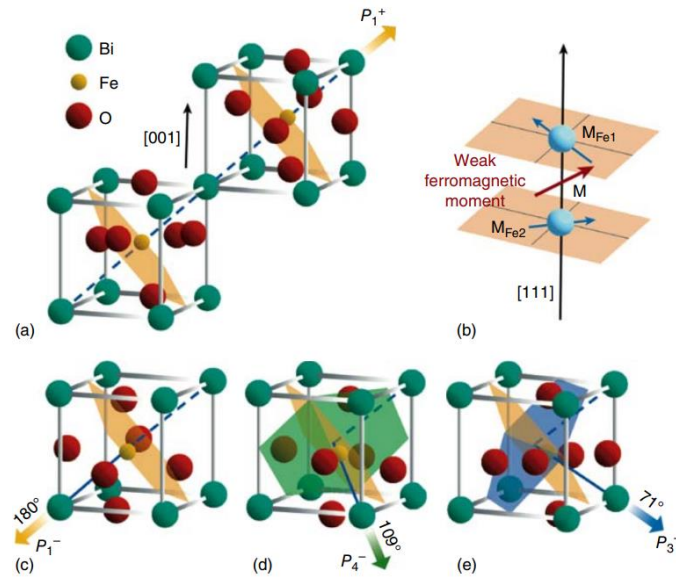


Figure 2.21. Schematic representation of the order parameter and single-multiferroic BiFeO_3 crystal structure. The yellow, green, and blue arrows indicate the polarization, while the shaded plane represents the antiferromagnetic plane. (a) The crystal structure of BiFeO_3 is oriented (001). (b) Diagram showing how the weak ferromagnetic moment in BiFeO_3 is formed by the Dzyaloshinskii-Moriya interaction. (c) An additional antiferromagnetic plane, with shifts of 190 degrees for (c), 109 degrees for (d), and 71 degrees for (e). An external electric field causes the antiferromagnetic planes to reorient.[14]

b. Multiferroic heterostructures.

As previously mentioned, a growing amount of research has focused on multiferroic composites over the past ten years in an effort to address the issues that seem to be inherent to single-phase materials. Ferroelectric and ferromagnetic phases are closely combined in these composites, which can be found in bulk, polymer-based, and thin-film composite materials. The advantages of multiferroic composite thin films over bulk and polymer composites are distinct. (i) Using epitaxial or super lattice composite thin films, we can control lattice matching through interface engineering and strain engineering, combining different phases of the film at the atomic level. (ii) By studying the interaction and competition mechanism between "spin-lattice-charge-orbit" multi-degrees of freedom in high-quality ME composite films, we can uncover the mechanism of ME coupling and comprehend the various effects associated with the interface. (iii) ME composite thin films can be blended with silicon components, which is anticipated to be used in electrical devices with multiple functions.[16]

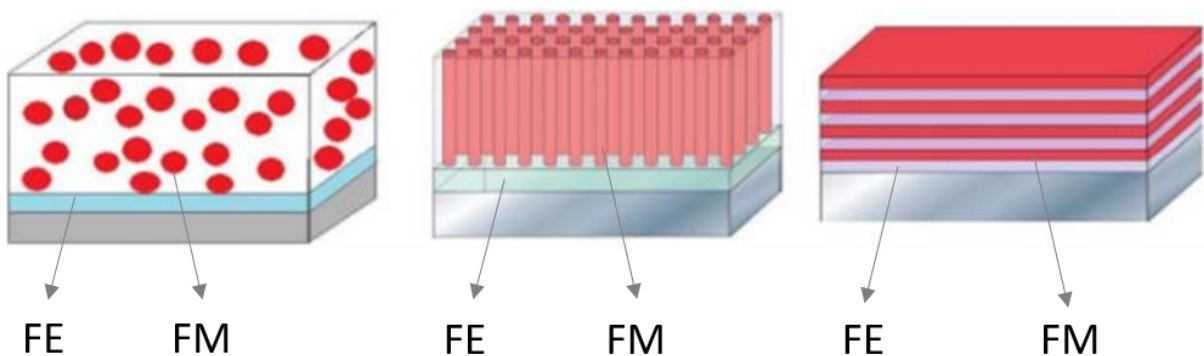


Figure 2.22. Schematic illustration of (a) 0-3, (b) 1-3, (c) 2-2 type structure on a substrate [15]

(iv) by adjusting the ferroelectric and ferromagnetic layers' thickness, orientation, number of layers, and growth order, the layered ME composite films can regulate the ME coupling coefficient. Thus, the field of integrated magnetic/electric devices holds great potential for multiferroic ME thin films.

Three primary categories of composite structure are depicted in Figure 2.22. 0-3 structure or 0-3 type particle composite thin film ferromagnetic nanoparticles disperse within the ferroelectric thin film matrix to form ME composite thin films (a). These 0-3 type composite thin films typically have ME coupling coefficients in the range of tens to hundreds of mV/cm Oe. Due to the challenge of fully polarizing the ferroelectric thin-film substrate, a large ME coupling coefficient is difficult to achieve.[17]

Ferromagnetic nano-columns scattered in the ferroelectric thin film matrix perpendicular to the plane form 1-3 type columnar composite thin films or 1-3 type cylindrical composite magnetoelectric thin films (b). While there is strong ME coupling in 1-3 columnar nanostructured composite films, their growth is hindered by harsh growth conditions, such as high growth temperature ($> 900\text{ }^{\circ}\text{C}$) and controlled growth of nano-columnar arrays. Furthermore, because the low resistance magnetic phase permeates the entire film, there is so much leakage conductance that it is impossible to observe the direct ME effect, making device application extremely challenging.

Laminated composite thin film 2-2 is the final type structure (c). Ferroelectric and ferromagnetic thin films can be readily deposited on the substrates layer by layer to create laminated ME composite thin films. Common 2-2 type ME composite films are either multilayer polycrystalline films fabricated by chemical solution spin-coating, which is a very straightforward, affordable, and accessible method, or epitaxial films prepared by PLD. Moreover, the main benefit of layered

thin film is that the insulated ferroelectric layer isolates the low-resistance magnetic layer from the plane of evaporation, hence eliminating the leakage issue entirely. Notably, in such NFO/BTO/STO composite film, a noteworthy ME response was directly observed. Upon computation, the composite film's ME voltage coefficient perpendicular to the film direction, or $\alpha_E = 12 \text{ mVcm}^{-1}\text{Oe}^{-1}$, is determined. Lately, by employing non-oxide ferroelectric and ferromagnetic materials and refining the composite thin film's structural design, it has become possible to achieve large ME coupling coefficients in 2-2 type composite thin films. Furthermore, $\text{SrRuO}_3/\text{BaTiO}_3/\text{SrRuO}_3$ composite thin film may be used as a four-state resistance device, according to first-principles calculations. When the barrier's electric polarization was reversed and the electrodes' magnetizations were changed from parallel to antiparallel, the multiferroic tunnel junction underwent substantial changes. After that, some system composites also exhibits the four-state resistance on other thin films such as $\text{Au}/\text{La}_{0.1}\text{Bi}_{0.1}\text{MnO}_3/\text{La}_{2/3}\text{Sr}_{1/3}\text{MnO}_3$, $\text{La}_{0.67}\text{Sr}_{0.33}\text{MnO}_3/\text{BiFeO}_3/\text{La}_{0.67}\text{Sr}_{0.33}\text{MnO}_3$, $\text{LSMO}/\text{La}_{0.5}\text{Ca}_{0.5}\text{MnO}_3/\text{BaTiO}_3/\text{LSMO}$. [16]

2.6.3 Magnetoelectric effect

Coexistence of coupling interactions between two "ferroic" phases in multiferroic materials can result in the creation of new functionalities. For instance, the coexistence of the ferromagnetic and ferroelectric phases results in the magnetoelectric effect. By means of the so-called direct magnetoelectric effect (DME), an applied magnetic field can regulate the electric polarization. Similarly, by using the so-called converse magnetoelectric effect (CME), an applied electric field can regulate the magnetization. The following is an expression for them:

$$\text{DME: } \Delta P = \alpha \Delta H \quad (2.14)$$

$$\text{CME: } \Delta M = \alpha \Delta E \quad (2.15)$$

In this case, H is the magnetic field, E is the electric field, P is the electric polarization, M is the magnetization or magnetic polarization, and α is the magnetoelectric coupling coefficient. In particular, the magnetoelectric effect is a produced property in multiferroic composites because the effect is present in the composites even though neither the ferroelectric phase nor the ferromagnetic phase do. The result of the piezoelectric effect in the ferroelectric phase and the magnetostrictive effect in the ferromagnetic phase is the magnetoelectric effect, i.e.[18]

$$\text{DME:} \quad \frac{\text{magnetic}}{\text{mechanical}} \times \frac{\text{mechanical}}{\text{electric}} \quad (2.16)$$

$$\text{CME:} \quad \frac{\text{electric}}{\text{mechanical}} \times \frac{\text{mechanical}}{\text{magnetic}} \quad (2.17)$$

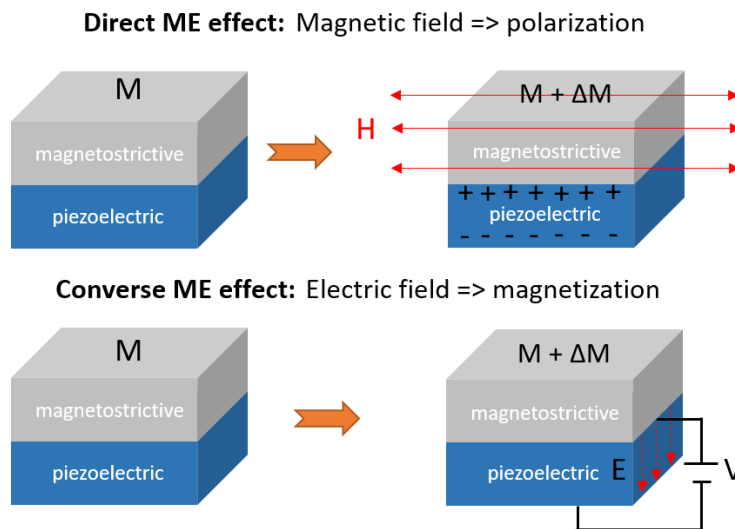


Figure 2.23. Schematic Diagrammatic representation of converse magnetoelectric coupling mediated by strain. Through the piezomagnetic effect, strain that an electric field creates in the ferroelectric material is mechanically transferred to the magnetic material, changing the magnetization.[17]

In particular, the magnetstriction effect causes a composite to change shape when a magnetic field is applied. Next, the electric polarization changes as a result of the mechanical strain being transferred to the ferroelectric phase, and vice versa (Fig. 2.23).

As in the case of ferroelectric and ferromagnetic hysteresis loops, ideally the electric polarization (P) and magnetization (M) exhibit a hysteresis characterization with the manipulation of magnetic field (H) and electric field (E), respectively (Fig. 2.24). As a result, there are a wide range of possible uses for the magnetoelectric effect, including memory devices and sensors.

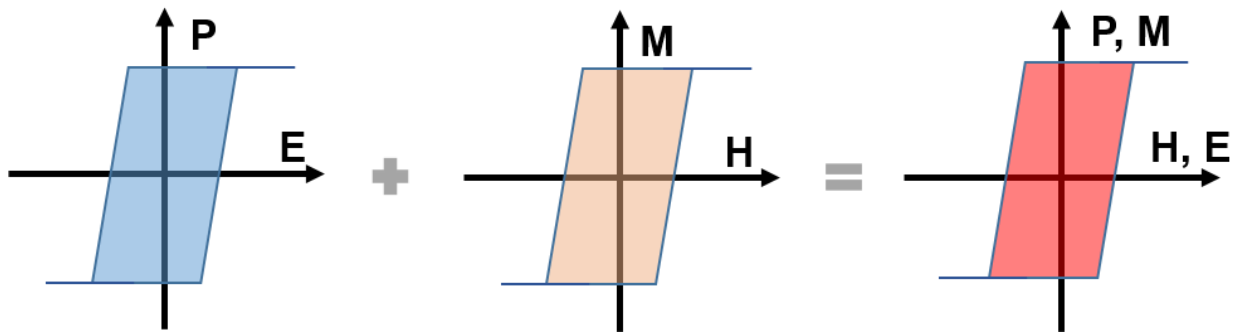


Figure 2.24. Schematic illustration of ideal ME effect

2.6.4 Electric field control magnetism in thin films

2.6.4.1 Brief history of electric field control magnetism in magnetic thin films

In the early 2000s, multiferroic materials (MFs) emerged from relative obscurity and began attracting renewed interest, particularly those with magnetoelectric properties, where magnetic and ferroelectric order parameters are interconnected. Fundamentally, the coexistence of magnetism

and ferroelectricity is often mutually exclusive, requiring innovative approaches to stabilize both orders within a single compound.

One of the most exciting aspects of these materials is their potential application in next-generation electronic devices, where magnetic states can be controlled by electric fields and vice versa. These multifunctional materials could be used in solid-state transformers, magnetic sensors, actuators, and, notably, in spintronics to design electrically writable, low-power, non-volatile magnetic memories. Despite extensive research, the search for room-temperature multiferroics with significant magnetoelectric (ME) coupling has not yet been successful. This challenge has led to intensive studies into composite multiferroics, which combine ferroelectric (FE) or piezoelectric materials with ferromagnets (FMs). Among these, thin film composite MFs are considered the most promising for device applications. This section will explore how electric fields can control magnetic properties in thin film composite MFs. Figure 2.25 (a)-(c) schematically illustrates various responses in magnetoelectric coupling within composite MFs, while (d)-(g) show magnetic hysteresis loops under different interfacial coupling conditions that are responsible for magnetoelectric coupling.

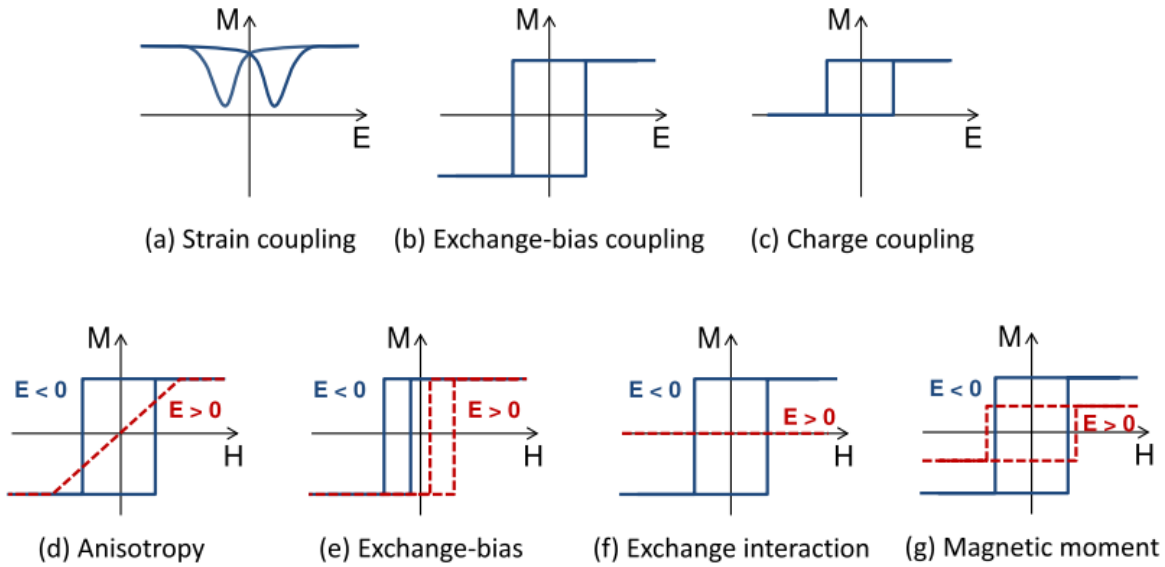


Figure 2.25. (a)-(c) Schematic of the different magnetoelectric response in composite multiferroics, (d)-(g) magnetic hysteresis loops for the different interfacial couplings responsible for the magnetoelectric coupling.[18]

a. Strain mediated magnetoelectric multiferroic

The converse piezoelectric effect in strain-mediated magnetoelectric multiferroics causes a change in the size of the FE lattice parameter when a magnetic film comes into contact with a ferroelectric one. The magnetic material in contact experiences strain as a result, which alters its magnetic properties, most notably its anisotropy through magnetostriction. Thus, the product of the piezoelectric effect in the FE phase and the magnetostrictive effect in the magnetic phase yields the corresponding converse ME coupling. It is as follows:

$$\text{Converse ME effect} = \frac{\text{Mechanical}}{\text{Electric}} \times \frac{\text{Magnetic}}{\text{Mechanical}} = \text{piezoelectric} \times \text{magnetostrictive}$$

$$\Delta M = \alpha \Delta E \quad (2.18)$$

We can obtain a ME coupling by calling it by the α coefficient using this formula. Compared to single-phase multiferroics, where the value is constrained by the square root of the product of the magnetic and electric susceptibilities, this value is much larger. On the other hand, MRAMs are predicated on the 180° deterministic control of the magnetization, while strain-mediated ME coupling typically leads to a less than 90° rotation of the magnetization. Therefore, strain-mediated ME coupling appears to be more promising for microwave magnetic devices that can be tuned for E-field. In contrast, multiferroic heterostructures produce a completely different square shape and a butterfly-shaped loop of magnetization vs. electric field that resembles that of strain vs. electric field and reveals the elastic nature of the ME coupling. Indeed, for small thickness of the ferromagnetic film, interface-charge-mediated ME coupling was predicted to dominate the changes in the magnetic properties by polarization reversal.

b. Electronic effect in magnetoelectric multiferroics

The effect of the ferroelectric (FE) polarization direction on the electronic structure of the ferromagnet at the interface pertains to the second type of magnetoelectric (ME) coupling, which allows for electric control of magnetic properties in ferroelectric/magnetic bilayers. Notably, these electronic effects can lead to two distinct magnetic states at electrical remanence, depending on the direction of FE polarization. This electronically-driven ME coupling is highly promising for applications and intriguing from a fundamental perspective. However, while elastic interactions can extend over several hundreds of nanometers, the field effect operates over distances comparable to the Thomas-Fermi screening length (λ_{TF}), which is one or two unit cells for metals and a few nanometers for semiconductors. Fortunately, in magnetic materials, changes in magnetic

properties can be detected over distances defined by the exchange interaction length (l_{ex}), which is usually larger than λ_{TF} and can approach 10 nm.

c. Other mechanisms based on intrinsic multiferroic

Heterostructures comprising a multiferroic or magnetoelectric material and an FM coupled by exchange-bias interaction provide an additional means of electrically controlling magnetization. Ferroelectric antiferromagnets (AFMs) make up the majority of multiferroic materials. Thus, the AFM and FE orders are linked by the ME coupling in these materials, which also permits an electric control of the AFM spin configuration. The FM's hysteresis loop shifts when FM/AFM heterostructures are cooled in the presence of a magnetic field across the AFM's Néel temperature. The exchange-bias field, which typically moves in the opposite direction of the cooling field, measures the magnitude of this shift. Although the exact mechanism underlying this exchange-bias interaction is still up for discussion, uncompensated spins at the interface are typically suggested. It's interesting to note that the E-field control of the exchange bias may cause the FM to change its magnetization direction by 180 degrees, opening up new possibilities for electrically controlled magnetic memories.

2.6.5 Applications of Multiferroics Materials on Spintronics

The field of spintronics, which combines electronics and spin functionalities, is expanding quickly and has already been used in commercial devices. The goal of spintronics devices, a new generation of nanoelectric devices, is to boost processing, memory, and power efficiency. Ferromagnetism (MRAM) and ferroelectricity (FeRAM) have been the basis of many valuable devices produced recently; however, they come with a number of limitations, including issues with writing, reading, and energy consumption, in addition to being very costly. As a result, there is a

high demand for the production of incredible memory that is also fast, reliable, non-volatile, dense, inexpensive, and energy-efficient. I will concentrate on the use of multiferroic materials in spintronics devices in this section. Due to the simultaneous existence of ferromagnetism and ferroelectricity, multiferroics are single or even multiphase materials. Therefore, the most significant materials in spintronics are those with magnetoelectric coupling multiferroics, which are well known for their multiferroic random access memory (MFRAM). In MFRAM, an electric field can control the magnetization (M, ferromagnetism), and a magnetic field can switch the polarization (P, ferroelectric). As a result, we can lower device prices, increase writing and reading speed, and use less energy.

a. Magnetic Random Access Memory (MRAM)

Unlike DRAM and SRAM technologies, which use electrical charges to store data bits, Magnetic Random Access Memory (MRAM) is a nonvolatile RAM technology. Memory cells with two magnetic storage elements one with a fixed magnetic polarity and the other with a switchable polarity are the foundation of MRAM operation. As seen in the cell structure in Fig. 2.26, these magnetic elements are separated by a thin insulating tunnel barrier. Giant magnetoresistance (GMR), tunnel magnetoresistance (TMR), magnetoresistance (MR), and anisotropic magnetoresistance (AMR) are the methods used in MRAM to write data by converting the two magnetic states (spin up or spin down). Combining the high density of DRAM with the high speed of static RAM, MRAM has the potential to greatly enhance electronic products by storing more data and facilitating faster access while using less battery power than current electronic memories.

[16]

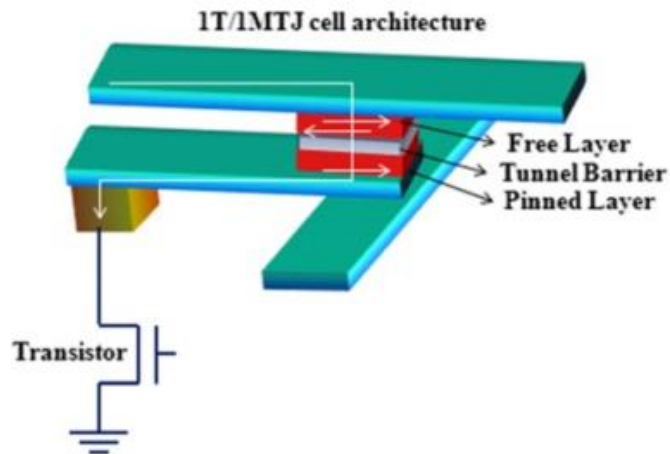


Figure 2.26. Basic MRAM cell structure. [18]

However, the ferromagnetic materials used in MRAM have high coercivity, necessitating a strong magnetic field to switch between the two magnetic states (write), resulting in high energy consumption. A recently developed writing method, called Spin-Transfer Torque (STT-RAM), eliminates the need for an external magnetic field. Although direct writing by electric current offers the significant advantage of confining the switching area and consuming much less energy compared to MRAM that requires a magnetic field, the energy consumption remains substantial. Therefore, alternative methods for processing magnetic data and writing on spintronic devices using electric fields and fully insulating structures to prevent the presence of electric current are still needed.

b. Ferroelectric Random Access Memory (FeRAM)

Figure 2.27 presents the cell of FeRAM which is a nonvolatile RAM and combining the fast read and write access of DRAM cells. FeRAM consisting of capacitor and transistor structure.

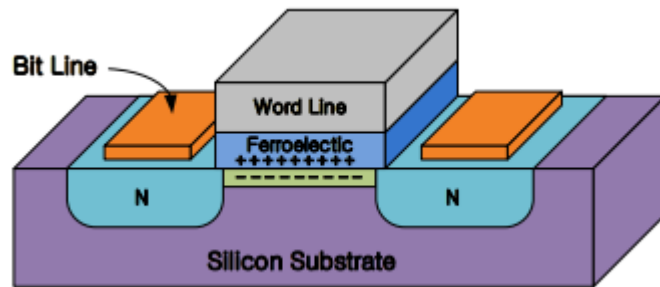


Figure 2.27. Basic FeRAM cell structure [18]

FeRAM is a prevalent type of computer memory that can retain data even when the power is turned off, without needing an external power supply. It achieves this by using a ferroelectric material instead of a conventional dielectric material between the capacitor's plates. When an electric field (E) is applied across the ferroelectric layer in FeRAM, the dipoles align with the field direction, causing a slight shift in atom positions and altering the distribution of electronic charge within the crystal structure. When the electric field is removed, the dipoles maintain their polarization state, allowing for data "reading" based on the orientation of the atoms in the dielectric. As a result of polarization switching, FeRAM offers faster writing speeds and greater energy efficiency. However, FeRAM has some limitations, such as destructive read operations that require subsequent resets, leading to size constraints and slower readability.

c. Single-phase multiferroic materials on spintronics

To date, many scientists have worked to improve both separately, with promising future results. However, is the integration the best? We can use the best MRAM and FeRAM functionalities (magnetic read and ferroelectric write, as shown above) to improve reading and writing speeds while also lowering energy consumption.

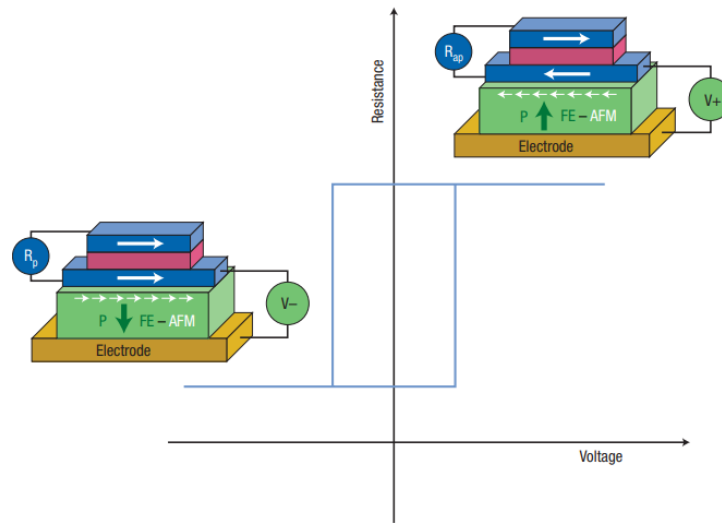


Figure 2.28. Sketch of a possible MERAM element.[18]

Figure 2.28 depicts the basic operation of magnetoelectric random access memories (MERAM), which use a voltage to switch the magnetization of a ferromagnetic layer by combining magnetoelectric coupling with interfacial exchange coupling between a multiferroic and a ferromagnet. Magnetoelectric coupling in MERAMs allows an electric field to control the exchange coupling at the interface of multiferroic and ferromagnet. The exchange coupling across the interface then controls the magnetization of the ferromagnetic layer, which can be switched by the multiferroic's electric polarization. Because almost every multiferroic is a ferroelectric antiferromagnet, recent research has concentrated on exchange bias, the directional coupling that occurs at the interface of a ferromagnet and an antiferromagnet. Until now, only BiFeO_3 (BFO) has demonstrated rhombohedral perovskite and antiferromagnetism with a Néel temperature of 640 K and ferroelectricity up to 1 at 100 K.

d. Composite multiferroic materials on spintronics

By combining two ferroic order parameters with room temperature ferroelectric and ferromagnetism, composite is an intriguing technique for producing multiferroic materials. Figure 2.29 depicts the simplest multiferroic tunnel junction, in which the two ferromagnetic electrodes are separated by a ferroelectric layer.

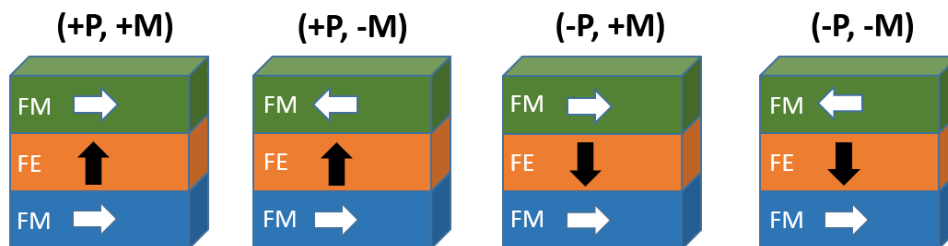


Figure 2.29. FM/FE/FM tunnel junction model.

Magnetoelectric coupling (if present) occurs at the interface of these devices via the following phenomena: elastic coupling between ferromagnetic/magnetostrictive materials and ferroelectric/piezoelectric materials, electric field modification of charge doping and the concomitant modification in magnetic ordering, and orbital reconstruction upon ferroelectric switching.

2.6 Reference

- [1] Physics of Ferromagnetism book, Chikazumi Graham
- [2] S. Wada, K. Yako, K. Yokoo, H. Kakemoto, and T. Tsurumi, “Domain wall engineering in barium titanate single crystals for enhanced piezoelectric properties,” *Ferroelectrics*, vol. 334, no. 1 PART 2, pp. 17–27, 2006.
- [3] L. S. R. Rocha *et al.*, “A study approach on ferroelectric domains in BaTiO₃,” *Mater. Charact.*, vol. 120, pp. 257–262, 2016.
- [4] T. H. E. Lahtinen, K. J. A. Franke, and S. Van Dijken, “Electric-field control of magnetic domain wall motion and local magnetization reversal,” *Sci. Rep.*, vol. 2, pp. 1–6, 2012.
- [5] F. Rubio-Marcos, A. Del Campo, P. Marchet, and J. F. Fernández, “Ferroelectric domain wall motion induced by polarized light,” *Nat. Commun.*, vol. 6, 2015.
- [6] Z. K. Zhang, D. N. Fang, and A. K. Soh, “A new criterion for domain-switching in ferroelectric materials,” *Mech. Mater.*, vol. 38, no. 1–2, pp. 25–32, 2006.
- [7] V. Boddu, F. Endres, and P. Steinmann, “Molecular dynamics study of ferroelectric domain nucleation and domain switching dynamics,” *Sci. Rep.*, vol. 7, no. 1, pp. 1–10, 2017.
- [8] M. G. Shaikh, S. Phanish, and S. M. Sivakumar, “Domain switching criteria for ferroelectrics,” *Comput. Mater. Sci.*, vol. 37, no. 1–2, pp. 178–186, 2006.
- [9] W. Kleemann and P. Borisov, “Multiferroic and magnetoelectric materials for spintronics,” *NATO Sci. Peace Secur. Ser. B Phys. Biophys.*, no. May 2014, pp. 3–11, 2008.
- [9] <https://plastometrex.com/blogs/an-introduction-to-stresses-and-strains>

- [10] <https://www.americanpiezo.com/knowledge-center/piezo-theory>
- [11] Jinghui Gao *et al.*, “Recent progress on BTO based piezoelectric ceramics for actuator application”, *Actuators* 2017, 6, 24
- [12] L. W. Martin *et al.*, “Multiferroics and magnetoelectrics: Thin films and nanostructures,” *J. Phys. Condens. Matter*, vol. 20, no. 43, 2008.
- [13] M. M. Vopson, “Fundamentals of multiferroic materials and their possible applications,” *Crit. Rev. Solid State Mater. Sci.*, vol. 40, no. 4, pp. 223–250, 2015.
- [14] V. Garcia, M. Bibes, and A. Barthélémy, “Artificial multiferroic heterostructures for an electric control of magnetic properties,” *Comptes Rendus Phys.*, vol. 16, no. 2, pp. 168–181, 2015.
- [15] A. O. Cetinkaya, S. Kaya, A. Aktag, E. Budak, and E. Yilmaz, “Structural and electrical characterizations of BiFeO₃ capacitors deposited by sol-gel dip coating technique,” *Thin Solid Films*, vol. 590, pp. 7–12, 2015.
- [16] A. J. C. BURMA, G. R. Blake, T. T. M. Palstra, and U. Adem, *Multiferroic Materials: Physics and Properties*. Elsevier Ltd., 2016.
- [17] W. Zheng *et al.*, “Strain control of phase transition and magnetic property in multiferroic BiFeO₃ thin films,” *Thin Solid Films*, vol. 695, no. October 2019, p. 137741, 2020.
- [18] I. Fina and X. Martí, “Spintronic Functionalities in Multiferroic Oxide-based Heterostructures,” *arXiv*, no. October, 2017.
- [19] N. A. Spaldin, “Multiferroics beyond electric-field control of magnetism,” *Proc. R. Soc. A*

Math. Phys. Eng. Sci., vol. 476, no. 2233, 2020.

- [20] J. Varignon, N. C. Bristowe, E. Bousquet, and P. Ghosez, “Magneto-electric multiferroics: Designing new materials from first-principles calculations,” *Phys. Sci. Rev.*, vol. 5, no. 2, pp. 1–24, 2020.

CHAPTER 3: LITERATURE REVIEW

In this section, I will provide a briefly overview of the background concerning the Fe film and BTO substrate. This will include discussion on domain patterns, the principles behind imprinting domains from ferroelectric into ferromagnetic materials into ferromagnetic films, and a review of practical applications of Fe/BTO films over the past few decades. Finally, I will outline some challenges that researchers in this field must address.

3.1 Fe/BaTiO₃ domain patterns

As discussed in Chapter 2, the tetragonal BTO (001) crystal can exhibit three possible domain patterns: c_1 - c_2 , a-c and a_1 - a_2 domains, with the polarization directions of a_1 , a_2 , and c domains aligned along the [100], [010], and [001] directions, respectively [1]. Ferroelastic a_1 - a_2 and a-c domains within ferromagnetic structures provide a means to establish domain correlations between ferroelectric BTO and a Fe ferromagnetic film. This mechanism is predicated on the strong pinning of ferroic domains, enabling the electric field to exert precise control over the magnetic domain of the Fe film through the evolution of BTO's domain configuration. Furthermore, the domain switching in BTO, which induces various strain levels, significantly influences the magnetism of the Fe film due to the robust magnetoelectric coupling at their interface. In ferromagnetic materials, magnetostriction properties cause shape changes during magnetization reversal, leading to the generation of magnetoelastic anisotropy (K_{me}) when an external mechanical stress is applied [2]

Figure 3.1 presents a full imprinting of the ferroelectric BTO of a-c (a) and a_1 - a_2 (b) domain patterns into the epitaxial Fe films. Consequently, the uniaxial magnetic easy axis is presented in

the Fe film on the in-plane domain of the BTO, while the biaxial magnetic easy axis is exhibited in that on the out-of-plane domain of the BTO.[3-5]

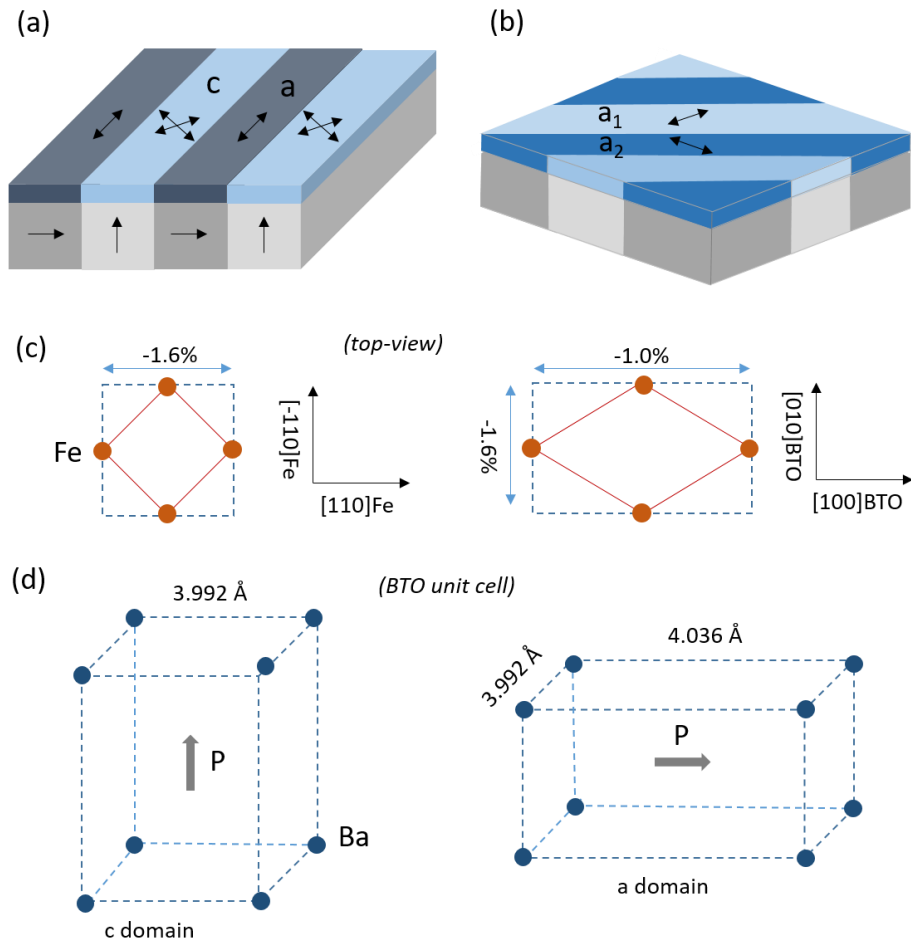


Figure 3.1. Schematic illustration of the domain configuration in the Fe/BTO system. (a) a-c domain, (b) a₁-a₂ domain, and (c) room temperature lattice parameters of the BTO substrate and the in-plane strains of the Fe film. (d) Unit cell of the BTO at tetragonal phase on the a and c domains.

3.2 Unique interface of Fe/BTO heterostructures

Interfacial magnetoelectric coupling is a viable avenue for achieving the electrical writing of magnetic information in spintronic devices. The mechanism behind this phenomenon lies in the alteration of ferroelectric-ferromagnetic interfacial bonds when the electric field was applied. This results in the change in the magnetization at the interface. The changes occurs due to shifts in interfacial atomic positions, caused by ferroelectric instability, leading to modification in the overlap between atomic orbitals. As illustrated in Fig. 3.2(a) and (b), the overlap between Ti and Fe electronic clouds were distinct for two opposite electric polarization in BTO. The d orbital hybridization between Ti and Fe is notably foe one of these polarization states. Additionally, an ultrathin oxidized iron layer, FeO_x , is present at the interface. Remarkably, the magnetization can be electrically and reversibly switched on and off at room temperature by reversing the BTO polarization.[6]

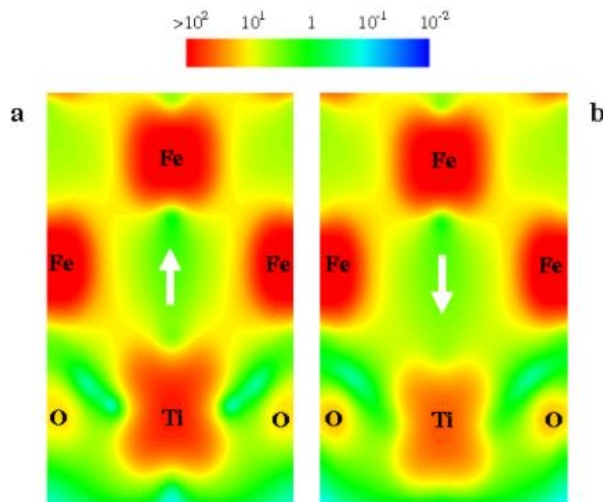


Figure 3.2. Minority-spin charge density at the Fe/BTO interface for two opposite electric polarization in BTO. The arrows indicate the directions of electric polarizations.[6]

The effects of an electric field (E) on the surface magnetization (M_S) is usually described in terms of the surface magnetoelectric coefficient (α_s) according to the following equation $\mu_0 \Delta M_S = \alpha_s E$. The observation value of $\alpha_s = 2 \times 10^{-9} \text{ Gcm}^2\text{V}^{-1}$, corresponding to the complete switching of the interfacial layer magnetization. [7, 8]

Figure 3.3 demonstrates that the magnetization of the oxidized iron layer at the Fe/BTO interface can be electrically and reversibly switched “on” and “off” at room temperature by reversing polarization of BTO. With ferroelectric polarization downward, the FeO_x interface will undergo a magnetic transition towards an AFM (or paramagnetic) state, while for ferroelectric polarization upward, the FeO_x interface remains robustly FM state.

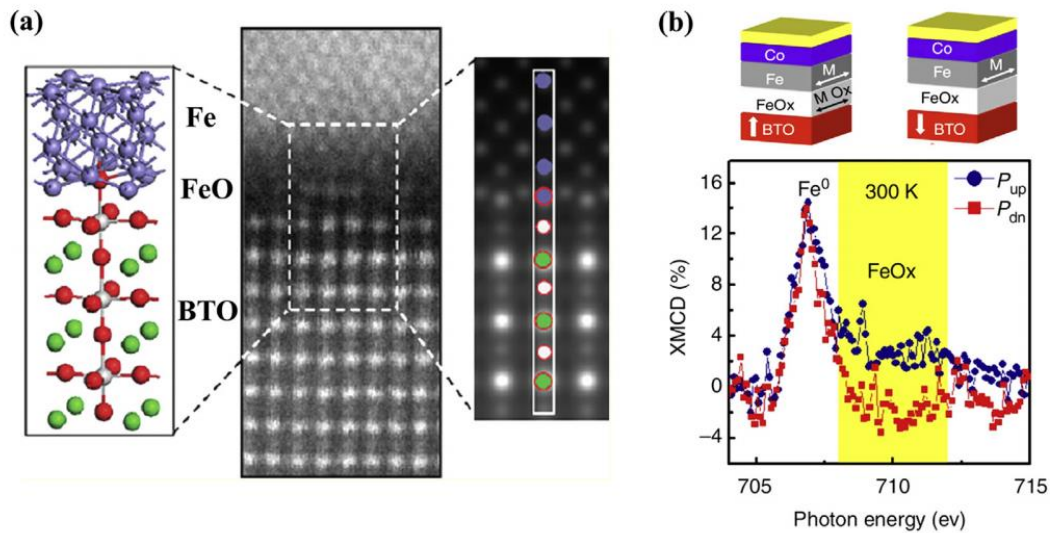


Figure 3.3. (a) The high-angle annular dark-field images and the interface model of Fe/BTO heterostructure. (b) The schemes of the Fe/BTO interfaces for P_{up} and P_{down} , and the XMCD signals in the Fe- L_3 energy region for BTO polarization P_{up} (blue circles) and P_{down} (red squares) for capacitors at 300 K.[6]

3.3 The remaining challenges

Recent reports have provided valuable insights into enhancing magnetoelectric coupling and delving deeper into the microscopic mechanisms underlying Fe/BTO films. However, certain challenges and questions remain:

1. While it is widely acknowledged that the BTO domain plays a pivotal role in modifying magnetic properties when an electric field is applied, the evolution of domain configurations from alternating a_1 - a_2 stripe domains to single c domains has not been fully understood. This area of research holds significant importance as the strain induced by alternating between a and c domains of BTO is substantial enough to rotate the magnetic anisotropy of the film.
2. The strain induced by BTO is acknowledged to transfer and modulate the magnetic properties of the film through magnetoelectric coupling at the interface. However, the sources of this strain have not been thoroughly studied. In the FeBTO multiferroic system, in addition to lattice mismatch and thermal strain, there exists a FeO_x layer at their interface that significantly influences the properties of the Fe film. Therefore, comprehending how lattice mismatch, thermal strain, and the strain induced from the FeO_x layer affect the Fe/BTO film is of significant importance.
3. While we are aware of the electric field's control over the magnetic anisotropy of Fe/BTO heterostructures, a comprehensive interpretation of these observations is yet to be presented. Studies in this area are essential for a deeper understanding.

3.4 References

- [1] L. S. R. Rocha *et al.*, “A study approach on ferroelectric domains in BaTiO₃,” *Mater. Charact.*, vol. 120, pp. 257–262, 2016.
- [2] Physics of Ferromagnetism book, Chikazumi Graham
- [3] T. H. E. Lahtinen, K. J. A. Franke, and S. Van Dijken, “Electric-field control of magnetic domain wall motion and local magnetization reversal,” *Sci. Rep.*, vol. 2, pp. 1–6, 2012.
- [4] T. H. E. Lahtinen, J. O. Tuomi, and S. Van Dijken, “Pattern transfer and electric-field-induced magnetic domain formation in multiferroic heterostructures,” *Adv. Mater.*, vol. 23, no. 28, pp. 3187–3191, 2011.
- [5] T. H. E. Lahtinen *et al.*, “Alternating domains with uniaxial and biaxial magnetic anisotropy in epitaxial Fe films on BaTiO₃,” *Appl. Phys. Lett.*, vol. 101, no. 26, pp. 1–5, 2012.
- [6] G. Radaelli *et al.*, “Electric control of magnetism at the Fe/BaTiO₃ interface,” *Nat. Commun.*, vol. 5, pp. 1–9, 2014.
- [7] R. Ramesh and L. W. Martin, “Electric field control of magnetism: multiferroics and magnetoelectrics,” *Riv. del Nuovo Cim.*, vol. 44, no. 5, pp. 251–289, 2021.
- [8] R. Ramesh and N. A. Spaldin, “Multiferroics: Progress and prospects in thin films,” *Nanosci. Technol. A Collect. Rev. from Nat. Journals*, vol. 3, pp. 20–28, 2009.

CHAPTER 4: METHODOLOGY

4.1 Molecular Beam Epitaxial (MBE) for thin film growth

MBE is one of the most effective physical vapor deposition (PVD) technologies existing today. It is used for producing the high-quality thin film in ultra-high vacuum (UHV). A. Y. Cho initially suggested MBE in 1970. MBE supplies numerous benefits over other traditional vapor deposition methods making it the most competitive thin film deposition technology. These advantages involve those that follow:

- Sample is grown in UHV (the typical base pressure is 10^{-10} Torr) which is very importance condition to produce high purity epitaxial thin film with controllable composition. This UHV condition of MBE is also suitable to integrate of many in-situ characterization tools such as: reflection high energy electron diffraction (RHEED) or low energy electron diffraction (LEED), ...
- The sample can be grown with low growth rate ($0.1 \sim 3 \text{ \AA/s}$) and low growth temperature. The evaporation of element is separated. These features enable MBE to precisely control of epi-layers at atomic scale and produce very sharp interface of super-lattices as well as multilayers.

However, there are some disadvantages of MBE such as: very complicate system, very expensive (10^6 /MBE chamber).

This section introduces some basic knowledge about vacuum levels, vacuum components, vacuum pumps, our home-built MBE set up and the calibration to get accurate temperature and growth rate

4.1.2 MBE setup

MBE is one of the most powerful method in PVD techniques, which is used to grow high quality thin film in UHV condition. Figure 4.1 shows out home-built MBE set-up and RHEED pattern of Fe film on BaTiO₃ (001) substrate. Our MBE system consist of three main chamber: the load lock chamber, the store chamber, and the growth chamber. An oblique configuration was used in our MBE system as shown in Fig. 4.1. A magnetic transfer bar is used to move sample. A high vacuum up to 10⁻⁶ Torr is created in load lock chamber using diaphragm pump and turbopump. The store and growth chamber are kept at UHV (10⁻¹⁰ Torr) condition by ion pump (not shown in the figure). During the growth we run liquid N₂ in cryo-panel. Water is used to cool down the growth chamber near effusion cells. Shutters with a linear configuration are used can be controlled by computer through a relay box, which open/close states can be changed within 0.1 second. The sample manipulator can rotate. A K-type thermocouple is used to determine temperature near the sample holder. Real substrate temperature is calibrated based on melting point of some typical metals (In, Sn, Be, etc.). The in-situ RHEED is used to monitor sample and substrate surface. By looking at RHEED pattern we may know whether the film is epitaxial or not and its surface quality. A shutter is placed in front of the florescent screen to protect it from the deposition of materials. To verify the growth rate and estimate the film's thickness we use a thickness monitor with quartz crystal, placed near substrate. In order to protect the heater of sample manipulator and substrate surface during rate checking, a shutter is used.

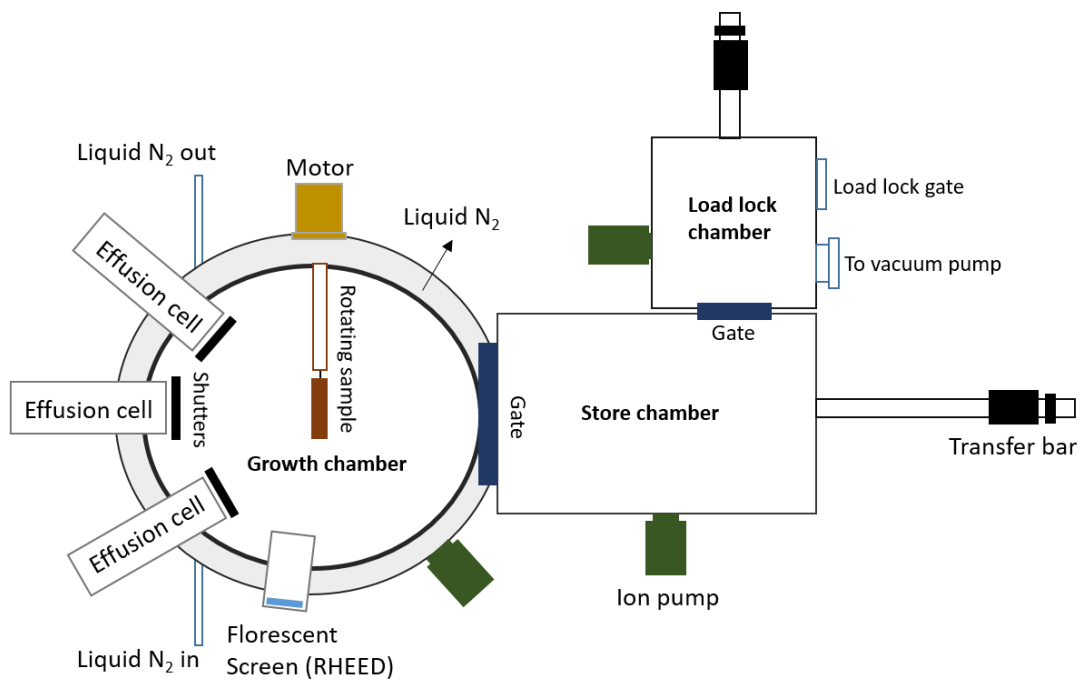


Figure 4.1. Diagram of our MBE system (AMS's lab).

4.1.3 Calibrations: substrate temperature, growth rate

Substrate temperature calibration: in our MBE system, we used a bare K-type thermocouple to determine the substrate temperature. A calibration of substrate temperature is needed because of many factors. The thermocouple is placed 1~3 mm from substrate (including thickness of sample holder and some distances). Therefore, a temperature gradient between reading and real temperature of substrate is expected. On the other hand, there are many factors affect to this temperature gradient such as; conduction from sample manipulator, heat radiation from sample holder surface, some displacement of thermocouple. In this work, we calibrated the substrate temperature by measuring the melting temperature of three materials: In (156.3 °C), Sn (231.9 °C), and Bi (271.3 °C). The temperature is read at each melting point of these materials to create three

data point. The reading temperature is linear function of real temperature. The linear function is given in the Fig. 4.2.

Growth rate also need to calibrate due to: the different positions, difference sticking coefficients of thickness monitor and substrate, and difference crystal between substrate and thickness monitor.

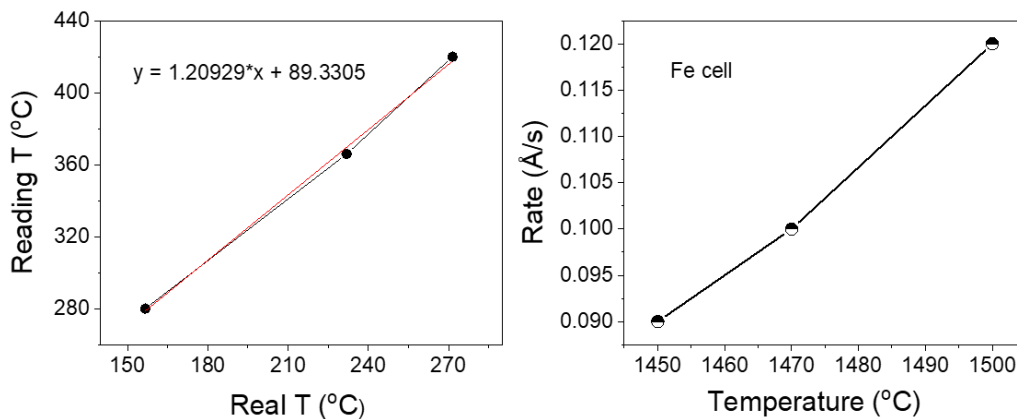


Figure 4.2. Calibration of substrate temperature (left) and growth rate of Fe cell (right)

To calibrate the growth rate we can use SEM cross section or AFM to determine the actual thickness of the film. On the other hand, it is impossible to detect a very low rate using thickness monitor. To solve this problem, we check the rate at high temperature is a linear curve in logarithm scale. As shown in Fig. 4.2 (right) is the growth rate of Fe cell.

4.2 Microstructural characterization

4.2.1 X-ray diffraction (XRD)

When a monochromatic X-ray beam irradiates a family of atomic planes, the waves in the X-ray beam can be diffracted. The diffraction condition is that the path differences ($\delta = 2d_{hkl}\sin\theta$) between the waves scattered by the atomic planes obey Bragg's Law: $2d\sin\theta = n\lambda$. The d_{hkl} is the

inter-planar distance. The θ and λ is the X-ray beam incident angle and the wavelength, respectively. The n is an integer representing the order of diffraction. In this topic, XRD measurements were conducted by the model of Smartlab, Rigaku X-ray diffractometer with $\text{CuK}\alpha$ radiation ($\lambda = 1.540499 \text{ \AA}$). A simplified schematic of X-ray diffractometer is shown in Fig. 4.3.

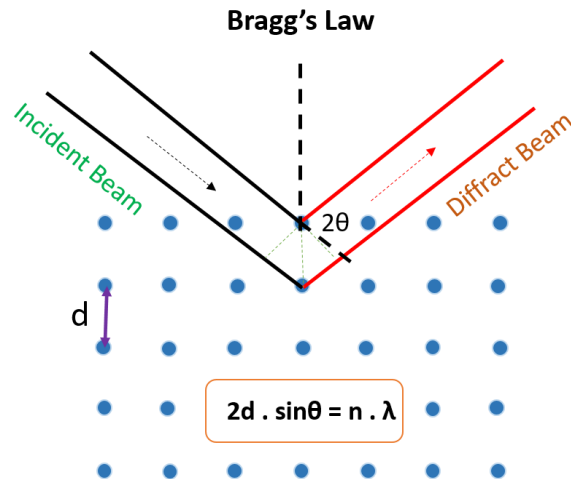


Figure 4.3. Simplified schematic of X-ray diffractometer in θ - 2θ Bragg reflection geometry.

First, for the Cu target in the X-ray tube, the X-ray beam has the $\text{K}\beta$ radiation filtered out using a Ni filter. Before and after incidence on the sample the beam was collimated with both divergence slit and anti-scattering slit of 0.6° wide, which is set according to the dimension of the sample. The X-ray diffractometer were analyzed.

The structure phase, texture, lattice parameter and minimum grain size can be identified and estimated from the XRD pattern. For example, in the cubic crystal, the lattice constant (a) is

calculated by the combination of Bragg law and $d_{hkl} = \frac{a}{\sqrt{(h^2+k^2+l^2)}}$. The minimum grain size (t) is estimated by the Scherrer formula:

$$t = \frac{0.9\lambda}{B\cos\theta_B} \quad (4.1)$$

where the B is the full width at the half maximum (FWHM) of the diffraction peak, Bragg angle θ_B is the diffraction peak position and λ is the X-ray wavelength. In addition, the shift and broadening of diffraction peaks can indicate the presence of compressive or tensile stress in the films. For the homogeneous strain (i.e uniform compressive or tensile strain), the diffraction peak position will shift to a higher or lower Bragg angle, respectively, because the lattice plane spacing (d) is reduced or increased, respectively according to Bragg law. However, for the inhomogeneous strain, the diffraction peak is broadened because non-uniform strain causes non-uniform interplanar spacing.

4.2.2 Reflection high energy electron diffraction (RHEED)

The RHEED is a useful technique to characterize the surface of crystalline materials during and after MBE growth. RHEED gun use a high voltage 0-30 kV to accelerate electron from filament. A phosphor screen is used to detect the diffraction pattern. The RHEED gun, phosphor screen, and substrate are positioned to create a small angle 1~2° between incident electron beam and sample surface. This very small angle ensures that the penetration depth of electron beam is only 1~2 atomic surface. That is reason why RHEED pattern only provide the surface information reflecting the growth mode and surface morphology. Streaky RHEED pattern indicates the smooth surface with the layer by layer growth mode. Spotty RHEED pattern indicates the smooth surface and three-dimensional growth mode. Ring pattern indicates the growth of polycrystalline thin film.

RHEED oscillation can be used to determine the layer by layer growth mode of the film. On the other hand, by meaning the line spacing in streaky patterns, we can determine the lattice constant of the thin film (provide that the lattice constant of substrate is known) with the error of 0.1%. The line spacing is inverse proportion to the lattice constant.

$$a \sim \frac{1}{d} \quad (4.2)$$

where, a is lattice constant, and d is line spacing in the streaky RHEED pattern.

4.3 Polarized light microscope (PLM)

The polarized light microscope system consisted of the polarization optics, an objective, and a digital camera. A single polarizer was used to identify the polarization axis in the alternating in-plane a_1 and a_2 stripe domains by rotating on the in-plane polarized light direction. We used the polarizing filter property of ferroelectric BTO reflecting the incident linear polarization light to determine the parallel and perpendicular alignments of the ferroelectric on each domain.(Fig. 4.4)An electric field wave (EM) is composed of oscillating electric and magnetic fields. In molecules, the electric field is stronger and more effective compared the magnetic field in exerting force on charges. Because electron masses are small, these electrons are the most affected charged particles. If an electron is forced to oscillate, it can absorb energy from the EM wave. This reduces the field on the wave and, hence, reduces its intensity. (Fig. 4.5)

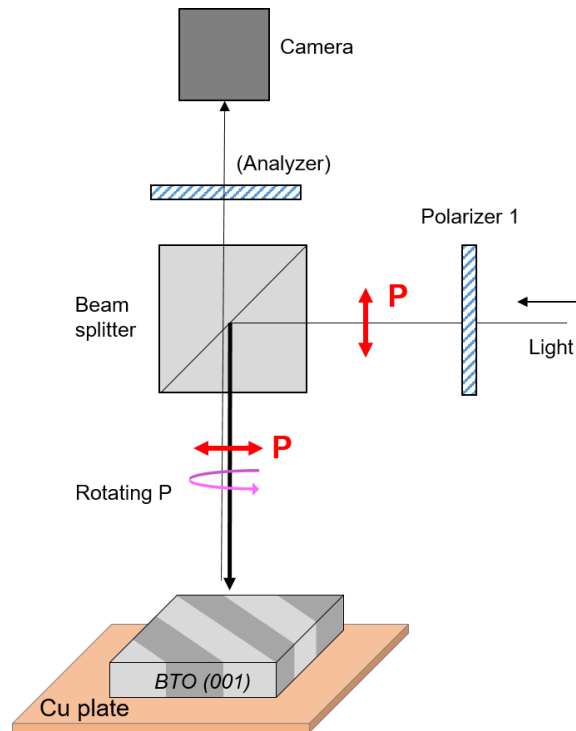


Figure 4.4. The polarized light microscope measurement setup for BTO (001) single crystal under applying an out-of-plane electric field.

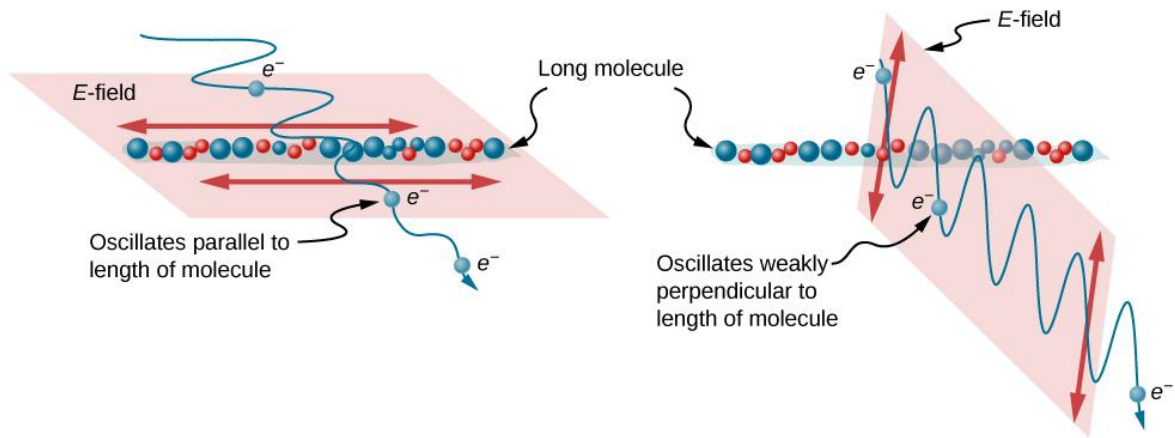


Figure 4.5. The schematic illustration of the principle of the reflection in the tetragonal BTO molecules to the incident polarized light. P is the polarization of domains with the polarization direction is represented by the double-head arrows in the in the inside of domains. (a) An electric field direction is parallel to the polarization direction. (b) An electric field direction is perpendicular to the polarization direction of BTO.

4.4 Magneto-Optical Kerr effect magnetometer (MOKE)

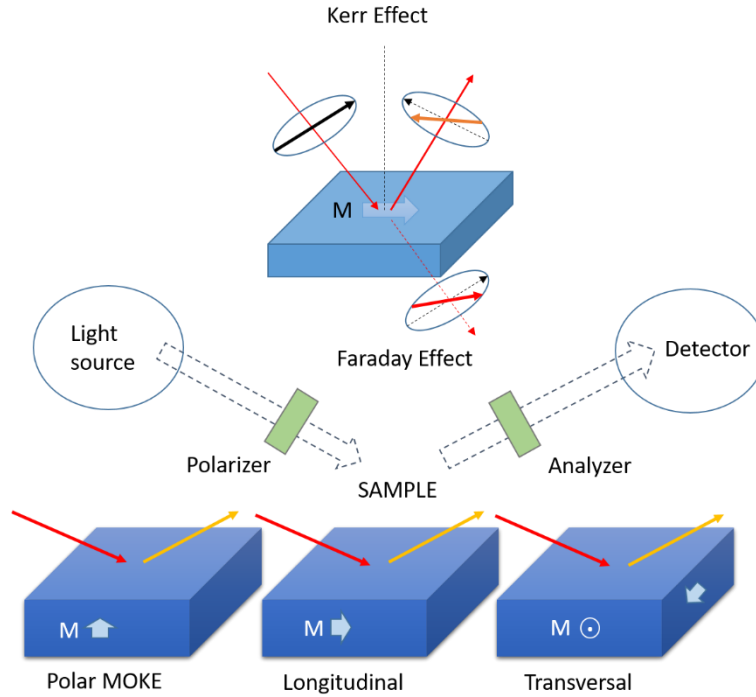


Figure 4.6. Domain observation by the Kerr effect. The three basic configuration of the polar, longitudinal, and transverse magneto-optical Kerr effect. The unit vector of magnetization is lying along the corresponding sensitivity axes (as indicated).

A MOKE magnetometer is a simple, non-destructive instrument, which is operated at room temperature and is used to determine the normalized magnetization loop of a magnetic film. When a light beam is incident on a magnetic sample, the electromagnetic waves in the light are subjected to a Lorentz force generated by the magnetization in the sample. Thus the polarization of the reflected light is rotated. The alteration of the polarization state can be detected and used to show the magnetization variation. There are three basic configurations (polar, longitudinal and

transverse) of the MOKE magnetometer classified by the relative orientation of the magnetization (M) with the incident light plane. On both polar MOKE and longitude MOKE, the orientation of the M is parallel to the incident plane. The difference between polar MOKE and longitude MOKE is that the M direction for the former is out-of-plane, while that for the latter is in-plane, as shown in Fig. 4.6.

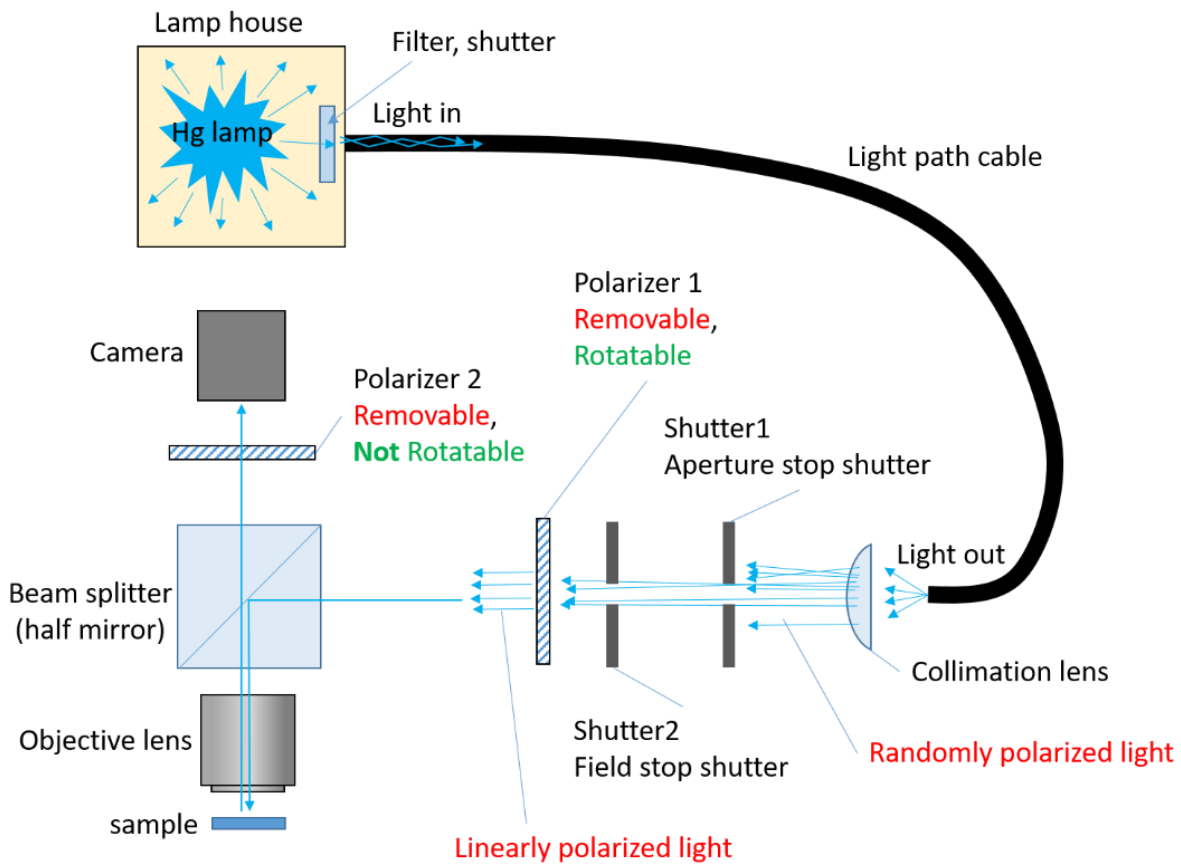


Figure 4.7. Schematic of MOKE devices of Spin Quantum Team (KRISS)

In this project, the longitude MOKE was used for magnetic characterization, the magnetization is in the plane of the sample and parallel to the incident plane. The MOKE set-up used includes a solid state laser diode of wavelength 635 nm as shown on Fig. 4.7. The skin depth of the laser is about ~ 30 nm at this wavelength for metallic films. The laser first passes through a polarizer before hitting the film. The polarizer angle was set at a certain value so that the laser has s (polarized perpendicular to the plane of incidence) and p (polarized parallel plane of incidence) mixed polarization. After reflecting from the film, the laser beam passed through an analyzer.

The analyzer angle was set close to the extinction point (normally deviating about 2°) for a symmetric hysteresis loops. Finally, the reflected laser was detected by a photo-detector. The sample was mounted on a sample stage. Also, a well polished substrate surface was required to avoid laser scattering and to enhance the signal to noise ratio.

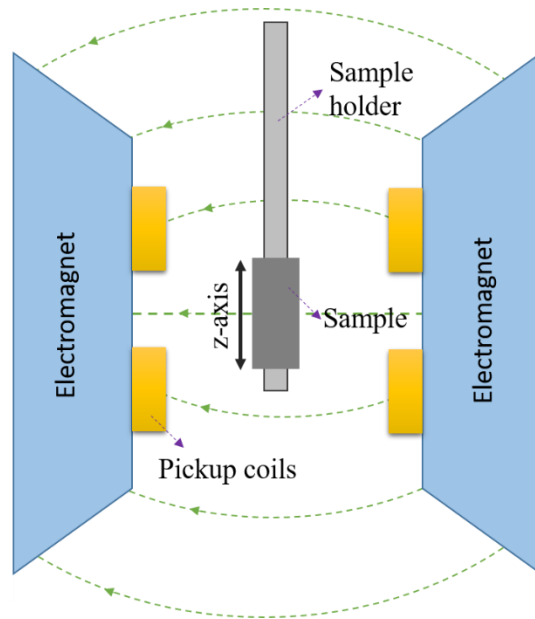


Figure 4.8. Schematic of Vibrating sample magnetometer (VSM)

4.5 Vibrating Sample Magnetometer (VSM)

The VSM is a commonly used instrument for the study of magnetic moments in many materials as a function of applied magnetic field and/or temperature (Figure 4.8). Its use in studies of superconducting materials arises from the ability to perform a contactless determination of the critical current density, by measuring the magnetic moment, and hence magnetization of the sample. We used the VSM system with range of 40 – 400 K. Limitation of magnetic field application is 10 kOe.

A VSM operates by first placing the sample to be studied in a constant magnetic field. If the sample is magnetic, this constant magnetic field will magnetize the sample by aligning the magnetic domains, or the individual magnetic spins, with the field. The magnetic dipole moment of the sample will create a magnetic field around the sample, sometimes called the magnetic stray field. As the sample is moved up and down, this magnetic stray field is changing as a function of time and can be sensed by a set of pick-up coils. The alternating magnetic field will cause an electric field in the pick-up coils according to Faraday's Law of Induction. This current will be proportional to the magnetization of the sample. The greater the magnetization, the greater the induced current. The induction current is amplified by a transimpedance amplifier and lock-in amplifier. The various components are hooked up to a computer interface. Using controlling and monitoring software, the system can tell you how much the sample is magnetized and how its magnetization depends on the strength of the constant magnetic field.

4.6 High voltage set-up for the converse ME effect

To study the converse ME coupling effect, a high voltage (maximum of 550 V) was applied to the piezoelectric BTO substrate so that a large strain was created in the sample. Then the effect of the strain on the magnetic properties of the thin film were investigated. Therefore, for this project, a high voltage set-up was build up within the MOKE magnetometer. The detailed diagram which explains how the high voltage was applied to the sample safely for a hysteresis loop be measured that is shown in Figure 4.9. The H-field was applied along the in plane direction of the BTO, while the voltage was along the out of plane direction of the sample. A custom made plastic sample holder sat on the metal columnar stage. Two thin metal pieces were fitted on the sample holder and used as two electrodes. Then the sample was clamped firmly between them so that a good contact was obtained between the sample surface and the electrodes. Before loading the sample into the MOKE, a multi-meter was used to check all connections. Finally, these two electrodes were connected with a high voltage supply

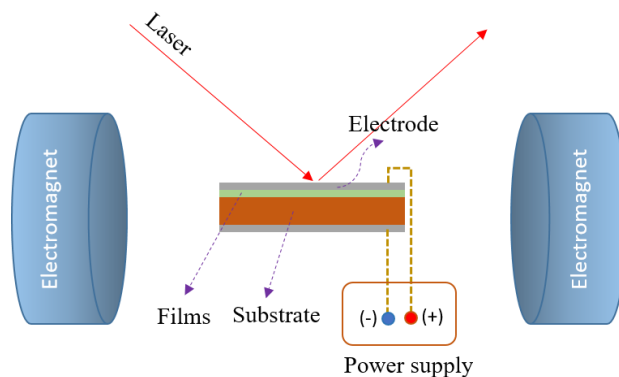


Figure 4.9. A simplified schematic (not to scale) of high field longitude geometry MOKE system. A voltage was applied on the sample when the converse ME effect was characterized and a schematic of high-voltage set-up designed in the high H-field MOKE magnetometer

4.7 References

- [1] Molecular Beam Epitaxy book, Robin F.C. Farrow.
- [2] https://en.wikipedia.org/wiki/Ultra-high_vacuum
- [3] Lecturer handout of Prof. Kim Jungdae (University of Ulsan) in Solid State of Physics subject.
- [4] <https://en.wikipedia.org/wiki/Pressure>
- [5] [https://en.wikipedia.org/wiki/Ion_pump_\(physics\)](https://en.wikipedia.org/wiki/Ion_pump_(physics))
- [6] A. Stupakiewics *et al.*, “Direct imaging of the magnetization reversal in microwire using all-MOKE microscopy,” *The Review of scientific instruments*, 2014.
- [7] https://en.wikipedia.org/wiki/Vibrating-sample_magnetometer
- [8] X-ray Diffracton book, B.E Warren.

CHAPTER 5: GROWTH TEMPERATURE DEPENDENCE MAGNETIC PROPERTIES OF EPITAXY Fe FILM ON BaTiO₃

Following interesting phase transition of BTO substrate, in this chapter, we discuss the effect of growth temperature on the saturation magnetization (M_S) and magnetic coercivity (H_C) of epitaxial Fe films grown on BaTiO₃ (BTO). When Fe films are formed on tetragonal BTO below the growth temperature of 120 °C, a tensile strain can be observed, nevertheless when Fe films are grown on cubic BTO above the growth temperature of 120 °C, a compressive strain is generated. The strongest tensile strain in Fe₃₀ and the compressive strain in Fe₄₀₀, when the lattice mismatch compressive and tensile thermal strains are combined, show a trend opposite to what was predicted. This could be because the FeOx interface layer has a larger lattice constant than expected. As the growing temperature went up from 30 to 400 °C, the H_C increased from 14.6 to 66.6 Oe and the M_S decreased from 2129 to 1244 emu/cm³.

5.1 Introduction

Multiferroic materials (MFs) exhibiting both ferromagnetism (FM) and ferroelectricity (FE) have attracted much attention for developing low power consumption and durability of multiferroic devices.[1]–[4] Because the single-phase MFs at room temperature are rare, two-phase MFs composed of FM/FE structures have been explored.[5],[6] Among FM/FE heterostructures, Fe/BaTiO₃ (Fe/BTO) film is one of the most promising magnetoelectric heterostructures due to high Curie temperature ($T_C = 770$ °C) of Fe and the negligible lattice mismatch between Fe ($a = 2.867$ Å) and BTO.[7],[8] The BTO is a widely studied ferroelectric material that has the

successive structural phase transitions from cubic ($a = 4.009 \text{ \AA}$) to tetragonal ($a = 3.991 \text{ \AA}$, $c = 4.035 \text{ \AA}$), orthorhombic ($a = 3.989$, $b = 5.667$, and $c = 5.681 \text{ \AA}$), and rhombohedral ($a = 3.998 \text{ \AA}$, $\alpha = 89.849^\circ$) phases at 120, 5, and $-195 \text{ }^\circ\text{C}$, respectively.[9] During the phase transition, the dielectric, ferroelectric, and piezoelectric properties are significantly adjusted. There are many reports on the manipulation of the magnetization and magnetic anisotropy of Fe/BTO films by applying electric field [10-18] and/or using strain induced from the BTO phase transition.[19] On the other hand, strain is known to be a powerful tool in modifying the structural, electronic, and magnetic properties of a material because the energies associated with structural and magnetic changes have a similar order of magnitude 0.1 eV/atom . Hwang *et al.* demonstrated that strain on antiferromagnetic Mn films on GaAs grown at temperature $30\sim 500 \text{ }^\circ\text{C}$ is strong enough to induce ferrimagnetic ordering up to a net magnetic moment of $0.33 \mu_B/\text{Mn}$ and the ferrimagnetic ordering lasts up to 9000 \AA thickness.[20] As a result, a comprehensive understanding of the role of strain-driven magnetic properties is crucial. However, strain type and sources and/or its related magnetic properties in Fe/BTO heterostructure have not been fully understood.[21] Besides, the temperature is a key factor for growing high-quality epitaxial film. Appropriate temperature is a very important term in crystal growth. It also decides many interface properties such as thickness, composition, and so on. As a result, a comprehensive understanding of the role of strain-driven magnetic properties is crucial. However, strain type and sources and/or its related magnetic properties in Fe/BTO heterostructure have not been fully understood.

Here we have studied the structural and magnetic properties of Fe films on BTO grown at temperature (T_g) from 30 to $400 \text{ }^\circ\text{C}$. A tensile strain is observed in Fe films grown on tetragonal BTO below the growth temperature of $120 \text{ }^\circ\text{C}$, whereas a compressive strain is induced in Fe films grown on cubic BTO above the growth temperature of $120 \text{ }^\circ\text{C}$. These are opposite to the

expectation, which may be due to the FeO_x interface layer. The H_C grew from 14.6 to 66.6 Oe as the growth temperature increased from 30 to 400 °C, while the M_S reduced from 2129 to 1244 emu/cm^3 .

5.2 Experiment methods

Fe thin films were grown on the BTO (001) substrate using molecular-beam epitaxy (MBE) at various substrate temperatures of 30, 100, 200, 300, and 400 °C, referred to as Fe30, Fe100, Fe200, Fe300, and Fe400, respectively. The BTO (001) substrate was cleaned with methanol, loaded into a growth chamber, and pre-heated at 600 °C to remove residual impurities. After that, the substrate was cooled down to the desired growth temperature to start the deposition of a 10-nm-thick Fe thin film. The deposition rate of Fe was 0.1 Å/s, determined using a quartz crystal thickness monitor. The base pressure of the growth chamber was $\sim 5 \times 10^{-10}$ Torr. The quality of the substrate and the films was monitored by in-situ reflection high energy electron diffraction (RHEED). To protect the films against oxidation, a 2 nm Sb capping layer was deposited on the sample's surface after the growth. X-ray diffraction (XRD, Smartlab, Rigaku) measurements were used to identify the crystal structure of the samples. A vibrating sample magnetometer (VSM) was used to determine the magnetic properties.

5.3 Results and discussions

5.3.1 Crystal structure of grown Fe/BTO films

Figure 6.1(a) shows the RHEED patterns of BTO substrate and Fe films along with [100] azimuth of BTO substrate, which are grown at various temperatures. The streaky RHEED pattern of the BTO substrate was observed, indicating the clean and flat surface. The RHEED patterns of Fe

films change with growth temperature from line-dot patterns for Fe30 and Fe100 to streaky patterns for Fe200, Fe300, and Fe400.

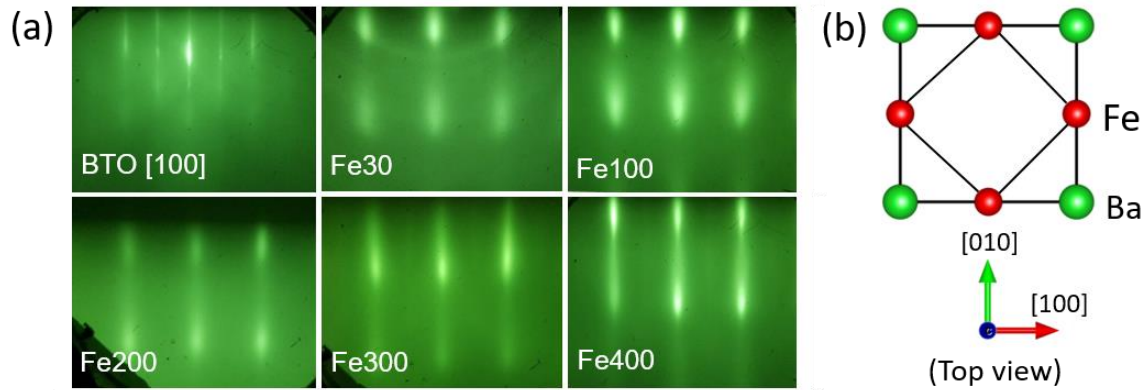


Figure 5.1. (a) RHEED patterns of BTO substrate and Fe films grown at 30, 100, 200, 300, and 400 °C along the BTO substrate's [110] azimuth. (b) Schematic illustration of Fe film and BTO substrate along Fe [100] // BTO [110]

This observation indicates that all films are epitaxial grown and growth mode changes with substrate temperature from 3D islands to 2D layer-by-layer growth mode. Figure 5.1(b) shows a schematic illustration on the epitaxial relationship between Fe films and BTO substrate along Fe [100] // BTO [110]. This epitaxial relationship is reasonable due to the small lattice mismatch, ~1%, between Fe and BTO.

To characterize the crystal structure of grown Fe/BTO films, we performed the room-temperature θ -2 θ XRD measurement (Fig. 5.2(a)). Fe (200) diffraction peak is observed at $\sim 65^\circ$ with the help of powder diffraction database JCPDS of 870721. The XRD patterns reveal diffraction peaks at 22.78° and 22.59° , at 45.21° and 45.71° , and at 69.86° and 70.77° , corresponding to tetragonal BTO (001) and (100), (002) and (200), and (003) and (300) planes, respectively. This confirms the

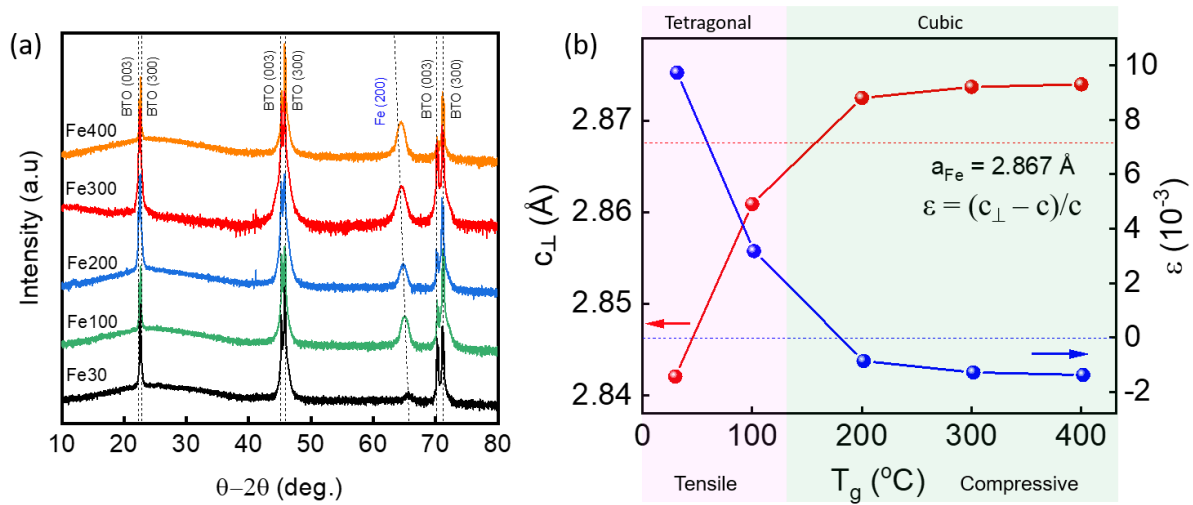


Figure 5.2. (a) θ - 2θ XRD patterns of Fe films grown at 30, 100, 200, 300, and 400 °C. (b) The determined c-axis lattice constant (out-of-plane) and the corresponding strain of Fe films

coexistence of the c- and a-domains in tetragonal BTO substrate at room temperature. It is well known that tetragonal BTO at room temperature has an alternating a and c stripe ferroelectric domains, which are perpendicular each other.

The peak of Fe (200) at $\sim 65^\circ$ becomes sharper at higher growth temperature, indicating an increase of crystallinity with growth temperature. Interestingly, the peak position slightly shifts to the lower angle as growth temperature decreases, indicating an increase of c-axis lattice constant (c_{\perp}) of the film. The out-of-plane strain (ϵ) as a function of growth temperature was calculated from c_{\perp} values following the equation of $\epsilon = (c_{\perp} - c)/c$, where c and c_{\perp} are the c-axis lattice constants of the Fe bulk and thin film, respectively. Positive ϵ value indicates in-plane compressive strained Fe film, while negative ϵ value indicates an in-plane tensile strain. The lattice constant of c-axis Fe film is calculated using the formula: $1/d^2 = (h^2 + k^2 + l^2)/c^2$, where d is the interatomic spacing, c is the

lattice constant, (*hkl*) is the miller indices; We used the (002) diffraction peak position to calculate the lattice constant. As seen in Fig. 5.2(b), Fe films grown on tetragonal BTO below 120 °C exhibit in-plane tensile strain, while the films grown on cubic BTO above 120 °C exhibit in-plane compressive strain. Note that the strongest tensile strain, +1%, is observed at Fe30. Full width at half maximum (FWHM) of (002) peak as a function of the growth temperature shows the smaller FWHM value, indicating the higher crystallinity with temperature, consistent with the RHEED pattern.

5.3.2 Effect of thermal strain in the Fe/BTO films during growth

Then, how to understand the observed strain in Fe/BTO? Considering lattice mismatch strain, the calculated lattice mismatches using bulk Fe and BTO lattice constants are -1.0% on a-domain and -1.6% on c-domain at tetragonal BTO phase, and -1.3% at cubic BTO phase,[7] implying that all films are under in-plane compressive strain. Thus, lattice mismatch strain seems not to be a suitable reason for the observed in-plane tensile strained Fe films grown on tetragonal BTO below 120 °C.

The other source, thermal strain, is calculated using the formula, $\varepsilon_{\text{thermal}} = (\alpha_{\text{Fe}} - \alpha_{\text{BTO}})\Delta T$, where ΔT is the temperature difference between the growth and the measurement temperatures and α_{Fe} and α_{BTO} are thermal expansion coefficients of Fe and BTO at growth temperature, respectively.

The average thermal expansion coefficients of Fe and BTO are $\alpha_{\text{Fe}} = 13.02 \times 10^{-6} \text{ K}^{-1}$ and $\alpha_{\text{BTO}} = 3.5 \times 10^{-6} \text{ K}^{-1}$, respectively, in the temperature range of 20 ~ 120 °C, and $\alpha_{\text{Fe}} = 14.17 \times 10^{-6} \text{ K}^{-1}$ and $\alpha_{\text{BTO}} = 10.0 \times 10^{-6} \text{ K}^{-1}$, respectively, in the temperature range of 130 ~ 400 °C.[22-24] During growth at elevated temperature, both Fe film and BTO of substrate are expanded. Cooling down to room temperature after growth, the Fe film shrinks more than BTO because of larger thermal

expansion coefficient of Fe compared to that of BTO, resulting in in-plane tensile strain (out-of-plane compressive strain).

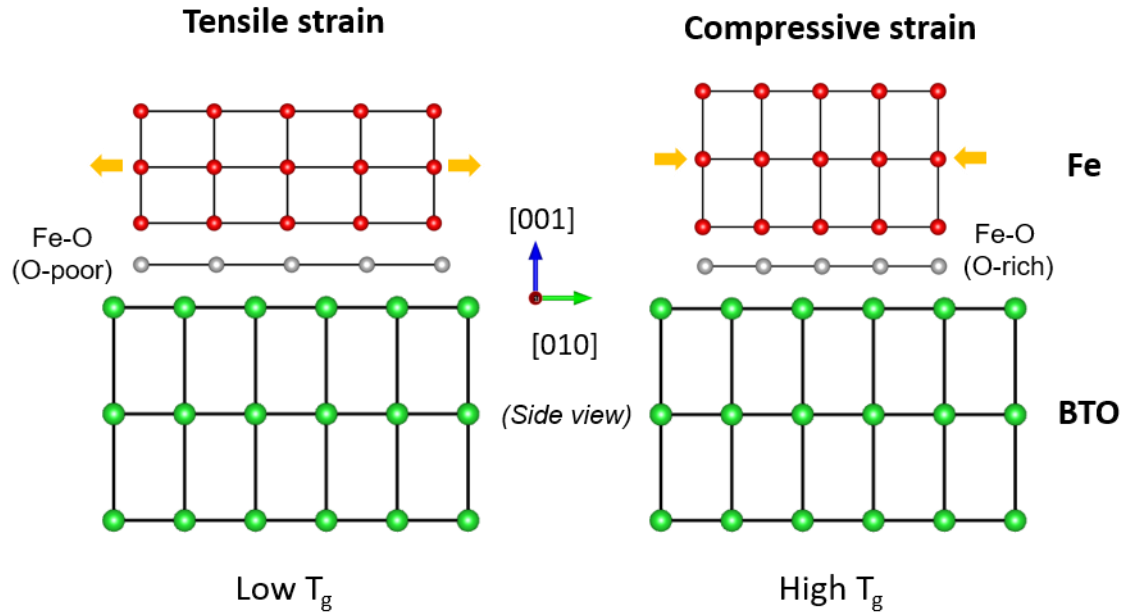


Figure 5.3. Atomic schematic illustration (side view) of (left figure) the tensile strain and (right figure) the compressive strain Fe films grown on the tetragonal and cubic BTO, respectively.

Table 5.1. Summarized Overview of all parameters.

| Name of sample | Growth temperature, T_g , (°C) | The lattice constant, a , (Å) | The induced strain, ϵ , ($\times 10^{-3}$) | Magnetization, M_s , (emu/cm ³) | Coercivity, H_c , (Oe) |
|----------------|----------------------------------|---------------------------------|---|---|--------------------------|
| Fe30 | 30 | 2.84205 | 9.73870 | 2129.3 | 14.59 |
| Fe100 | 100 | 2.86089 | 3.17374 | 1735.4 | 23.04 |
| Fe200 | 200 | 2.87248 | -0.86569 | 1649.6 | 51.70 |
| Fe300 | 300 | 2.87370 | -1.28883 | 1283.0 | 59.53 |
| Fe400 | 400 | 2.87397 | -1.38222 | 1244.0 | 66.59 |

No thermal strain in Fe30 and a strong tensile in Fe400 are expected. Combining the expected lattice mismatch compressive strain and compressive thermal strain, the small compressive strain in Fe30 and the strongest compressive strain in Fe400 are opposite trend to the expectation.

The most possible reason may be due to the presence of FeO interface layer. Brivio *et al* reported the interdiffusion of Ba and Ti cations or Fe atoms in Fe/BTO by X-ray photoemission spectroscopy, resulting in the Fe oxidation at interface.[10] In atomically resolved STEM (scanning transmission electron microscope) and EELS (electron energy loss spectroscopy) investigations, the presence of a single FeO layer between BaTiO₃ and Fe has been confirmed. Bocher. et al. reported an intermediate FeO monolayer between BTO and Fe. Also, Radaelli et al detected a significant amount of O beyond the BTO, suggesting FeO_x interfacial layer at the interface plane. The strongest tensile strain, +1%, in Fe30 may be induced by FeO_x interface layer with larger lattice constant. A compressive strain in Fe400 may be oxygen-rich FeO_x interface layer. Figure 5.3 presents the atomic schematic illustration of the tensile strain in the sample grown at low temperature (tetragonal BTO) and the compressive strain in that grown at higher growth temperature (cubic BTO).

5.3.3 The influence of strain on the magnetism of Fe films

To investigate the influence of strain on the magnetism of Fe films, we measured the room temperature magnetic hysteresis loops of Fe films under an in-plane and out-of-plane magnetic fields, as shown in Fig. 5.4(a) and 5.4(b), respectively. Fe films exhibit the ferromagnetic ordering along with an in-plane easy axis due to the shape anisotropy. We plotted the growth temperature vs. the saturated magnetization and coercivity as shown in Fig 5.4(c). The H_C grew from 14.6 to 66.6 Oe as the growth temperature increased from 30 to 400 °C, while the M_S reduced from 2129 to 1244 emu/cm³. The temperature dependence on normalized magnetization under a 1 kOe in-plane magnetic field is shown in Fig. 5.4(d). The determined materials constants of Fe on BTO at various growth temperatures are summarize in Table 5.1. The contribution of the significant increase in H_C and reduction in M_S with growth temperature is attributed to the strain in the film. The magnetization of Fe film has two abrupt changes at -195 and 5 °C, corresponding to BTO phase transition temperature. Thus, the structured phase transition of BTO causes lattice distortion on the films at their interface, modifying magnetic properties.

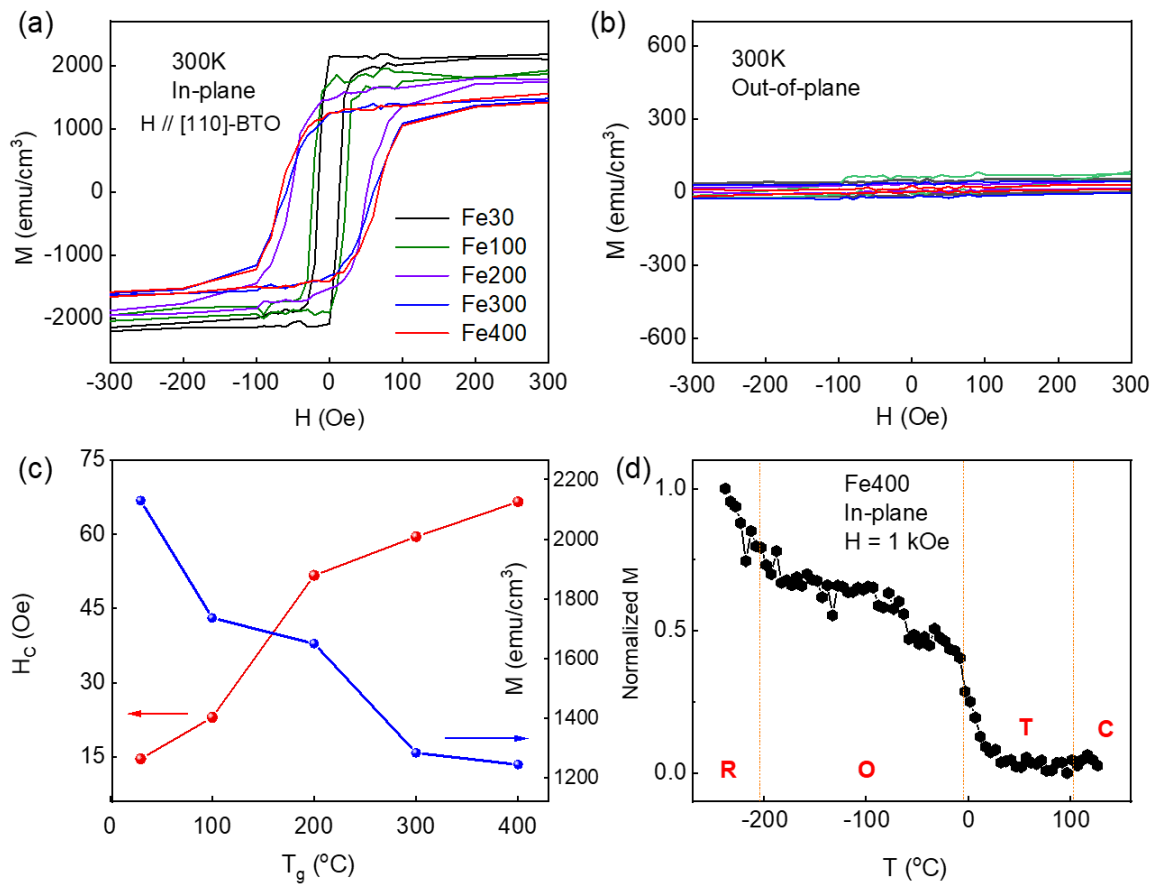


Figure 5.4. Room temperature (a) in-plane and (b) out-of-plane magnetic hysteresis loops of Fe films grown at various temperatures. (c) Coercivity and saturation magnetization as a function of growth temperature. (d) Temperature dependence of normalized magnetization (M vs T curve) of Fe400 film under the magnetic field of 1 kOe. The rhombohedral, orthogonal, tetragonal, and cubic structural phases of BTO are represented by the letters R, O, T, and C, respectively.

5.4 Conclusion

In summary, we have successfully grown the Fe epitaxial thin films on the BTO substrate at various temperatures. The growth mode and crystallinity of the films were modified by the growth temperature. We investigated the effect of strains on magnetic properties of epitaxial films. Tensile strain is observed in Fe films 120 °C, while grown on tetragonal BTO below compressive strain is observed on cubic BTO above 120 °C. The observation is caused by the FeO_x interface layer. Tensile strained Fe films have a higher H_C and a lower M_S value over compressive strained Fe films. This provides the way how to use a strain to modify the magnetic characteristics of epitaxial Fe films, which will be a useful information on the design of future spintronic devices.

5.5 References

- [1] K. Eshraghian, “Evolution of Nonvolatile Resistive Switching Memory Technologies: The Related Influence on Heterogeneous Nanoarchitectures,” *Trans. Electr. Electron. Mater.*, vol. 11, no. 6, pp. 243–248, 2010.
- [2] R. Ramesh and L. W. Martin, “Electric field control of magnetism: multiferroics and magnetoelectrics,” *Riv. del Nuovo Cim.*, vol. 44, no. 5, pp. 251–289, 2021.
- [3] R. Ramesh and N. A. Spaldin, “Multiferroics: Progress and prospects in thin films,” *Nanosci. Technol. A Collect. Rev. from Nat. Journals*, vol. 3, pp. 20–28, 2009.
- [4] S. M. Yakout, “Spintronics: Future Technology for New Data Storage and Communication Devices,” *J. Supercond. Nov. Magn.*, vol. 33, no. 9, pp. 2557–2580, 2020.
- [5] J. Ma, J. Hu, Z. Li, and C. W. Nan, “Recent progress in multiferroic magnetoelectric composites: From bulk to thin films,” *Adv. Mater.*, vol. 23, no. 9, pp. 1062–1087, 2011.
- [6] C. Lu, M. Wu, L. Lin, and J. M. Liu, “Single-phase multiferroics: New materials, phenomena, and physics,” *Natl. Sci. Rev.*, vol. 6, no. 4, pp. 653–668, 2019.
- [7] G. Venkataiah, Y. Shirahata, M. Itoh, and T. Taniyama, “Manipulation of magnetic coercivity of Fe film in Fe/BaTiO₃ heterostructure by electric field,” *Appl. Phys. Lett.*, vol. 99, no. 10, pp. 98–101, 2011.
- [8] S. Brivio, D. Petti, R. Bertacco, and J. C. Cezar, “Electric field control of magnetic anisotropies and magnetic coercivity in Fe/BaTiO₃ (001) heterostructures,” *Appl. Phys. Lett.*, vol. 98, no. 9, pp. 0–3, 2011.
- [9] Y. Shirahata, T. Nozaki, G. Venkataiah, H. Taniguchi, M. Itoh, and T. Taniyama,

- “Switching of the symmetry of magnetic anisotropy in Fe/BaTiO₃ heterostructures,” *Appl. Phys. Lett.*, vol. 99, no. 2, pp. 98–101, 2011.
- [10] S. Sahoo, S. Polisetty, C. G. Duan, S. S. Jaswal, E. Y. Tsympal, and C. Binek, “Ferroelectric control of magnetism in BaTiO₃/Fe heterostructures via interface strain coupling,” *Phys. Rev. B - Condens. Matter Mater. Phys.*, vol. 76, no. 9, pp. 3–6, 2007.
- [11] G. Venkataiah, Y. Shirahata, I. Suzuki, M. Itoh, and T. Taniyama, “Strain-induced reversible and irreversible magnetization switching in Fe/BaTiO₃ heterostructures,” *J. Appl. Phys.*, vol. 111, no. 3, 2012.
- [12] G. Venkataiah, E. Wada, H. Taniguchi, M. Itoh, and T. Taniyama, “Electric-voltage control of magnetism in Fe/BaTiO₃ heterostructured multiferroics,” *J. Appl. Phys.*, vol. 113, no. 17, pp. 1–4, 2013.
- [13] T. H. E. Lahtinen *et al.*, “Alternating domains with uniaxial and biaxial magnetic anisotropy in epitaxial Fe films on BaTiO₃,” *Appl. Phys. Lett.*, vol. 101, no. 26, pp. 1–5, 2012.
- [14] G. H. Kwei, A. C. Lawson, S. J. L. Billinge, and S. W. Cheong, “Structures of the ferroelectric phases of barium titanate,” *J. Phys. Chem.*, vol. 97, no. 10, pp. 2368–2377, 1993.
- [15] C. A. F. Vaz, J. Hoffman, A. B. Posadas, and C. H. Ahn, “Magnetic anisotropy modulation of magnetite in Fe₃O₄/BaTiO₃ (100) epitaxial structures,” *Appl. Phys. Lett.*, vol. 94, no. 2, pp. 92–95, 2009.
- [16] T. H. E. Lahtinen and S. Van Dijken, “Temperature control of local magnetic anisotropy in multiferroic CoFe/BaTiO₃,” *Appl. Phys. Lett.*, vol. 102, no. 11, 2013.

- [17] H. F. Tian *et al.*, “Strain induced magnetoelectric coupling between magnetite and BaTiO₃,” *Appl. Phys. Lett.*, vol. 92, no. 6, pp. 1–4, 2008.
- [18] V. Gorjge, A. Swain, K. Komatsu, M. Itoh, and T. Taniyama, “Magnetization Reversal in Fe/BaTiO₃(110) Heterostructured Multiferroics,” *Phys. Status Solidi - Rapid Res. Lett.*, vol. 11, no. 11, pp. 1–5, 2017.
- [19] Y. Hwang *et al.*, “Ferromagnetic ordering in Mn induced by thermal strain,” *Phys. Rev. B - Condens. Matter Mater. Phys.*, vol. 79, no. 4, pp. 1–5, 2009.
- [20] J. J. Wang, F. Y. Meng, X. Q. Ma, M. X. Xu, and L. Q. Chen, “Lattice, elastic, polarization, and electrostrictive properties of BaTiO₃ from first-principles,” *J. Appl. Phys.*, vol. 108, no. 3, 2010.
- [21] T. Mion, D. M. Potrepka, F. J. Crowne, A. Tauber, and S. C. Tidrow, “Dielectric and X-ray diffraction analysis of Ba(Ga,Ta)_{0.05}Ti_{0.90}O₃,” *Ferroelectrics*, vol. 473, no. 1, pp. 13–23, 2014.
- [22] “Thermal expansion coefficient of Fe and BTO” .
- [23] S. Brivio, C. Rinaldi, D. Petti, R. Bertacco, and F. Sanchez, “Epitaxial growth of Fe/BaTiO₃ heterostructures,” *Thin Solid Films*, vol. 519, no. 17, pp. 5804–5807, 2011.
- [24] L. Bocher *et al.*, “Atomic and electronic structure of the BaTiO₃/Fe interface in multiferroic tunnel junctions,” *Nano Lett.*, vol. 12, no. 1, pp. 376–382, 2012.
- [25] G. Radaelli *et al.*, “Electric control of magnetism at the Fe/BaTiO₃ interface,” *Nat. Commun.*, vol. 5, pp. 1–9, 2014.

CHAPTER 6: THE INSIGHTFUL UNDERSTANDING ON P-E HYSTERESIS LOOP OF BaTiO₃ SINGLE CRYSTAL USING POLARIZED LIGHT MICROSCOPE

Our next motivation is studying on the electric field control of magnetic anisotropy of epitaxial Fe/BTO film. To do that, we study about the domain configuration of BTO under electric field first. In this chapter, we report on single in-plane domain evolution of ferroelectric BaTiO₃ (BTO) under out-of-plane electric field using polarized light microscope, which helps an insightful understanding P-E hysteresis loop of ferroelectric BTO. Specifically, by applying a low electric field along with out-of-plane direction, the initial alternating in-plane stripe domains experience the domain wall motion to become the single in-plane domain. This is attributed to that the in-plane polarization is slightly out-of-plane. With a higher electric field, the single out-of-plane domain is observed through domain nucleation and domain wall movement. Resulting in all polarization orients to the external electric field direction. After saturating, a domain evolution process is investigated in the presence of an antiparallel out-of-plane electric field, which causes the polarization to switch from out-of-plane to antiparallel out-of-plane. Interestingly, two 90° switching steps are found instead of conventional 180° domain-switching. That could occur to release the internal stress in the polarization reversal. As a result of our research, we demonstrated a clearly domain-switching process of BTO by applying low field for a long-time duration.

6.1 Introduction

Ferroelectric materials have been extensively used in microelectronic and sensing applications for a long time because of possessing high dielectric permittivity and spontaneous polarization.[11]–

[15] Ferroelectric domains, the basic structural units, play a crucial role in determining the unique ferroelectricity. Particularly, controlling the domain evolution, which can be modulated by applying external stress or external electric field, provides an ability to obtain the various polarization states.[16]–[18] Therefore, studying the response of domains to external forces is especially essential for the application and designs of ferroelectric materials. To date, the domain-switching behavior, such as domain formation, domain wall motion, and domain-switching criteria, under external loads has been studied by many researchers.[19]–[22]

Due to a high dielectric constant and simple crystal structure, BaTiO_3 (BTO) has been recognized as an interesting candidate for many applications such as non-volatile memories, communication devices, and micro-actuators.[23]–[30] BTO single crystal exhibits tetragonal structure which presents the spontaneous polarization by off-centered Ti^{4+} atom in unit cell at room temperature. In the absence of external stimuli, the spontaneous polarization aligns with the six-equivalent $\langle 100 \rangle$ directions. Normally, BTO demonstrates three types of domain configurations consisting of head-to-tail c - a_1 , c - a_2 , and a_1 - a_2 domains to minimize electrostatic energy at the domain wall.[31]–[33] Here, the out-of-plane c domains have polarization along $[001]$ direction. The in-plane domains are named by a_1 and a_2 with polarization along $[010]$ and $[100]$ direction, respectively. According to the domain-switching criteria, an electric field generally could cause both 180° and 90° domain switching based on the domain nucleation and domain wall motion while the mechanical stress could only cause 90° domain switching. In addition, 180° domain switching will occur when applying an antiparallel electric field.[34] There is a variety of factors affecting the domain switching mechanism. Normally, the unit cell distortion caused by an applied electric field which as intrinsic contribution. On the other hand, the extrinsic contribution as the converse piezoelectric effect of a ferroelectric material is main source to modulate the crystal as

well. That is a reason why the motion of non-180° ferroelectric domain wall is occurred.[35] Nonetheless, defect such as oxygen vacancies, point charges, and dislocations play a crucial role in the polarization switching.[27]

Recently, some studies have found that, in BTO single crystals, 180° domain switching occurs via a two-step 90° domain switching process (the electric field of 2 kV/cm and the experiment time of 222 hours) under applying an antiparallel electric field.[36] In this previous report, by applying electric field on an out-of-plane mono-domain, the polarization vector switches 90° to become the in-plane mono-domain with the polarization direction perpendicular to the external field. The polarization vectors of the new mono-domain switched 90° once again to become parallel to the direction of the external field. Herein, the two-step 90° domain switching process is demonstrated by slowly moving on the domain walls under applying a low electric field.

In this study, we develop a process (the applying low electric field of 6 kV/cm, and the duration time of about 20 hours) using polarized light microscope to insightfully understand the evolution of the alternating in-plane BTO stripe domain under the out-of-plane electric field. Besides, we could confirm the two-step 90° domain switching in BTO single crystal.[36] Specifically, we reveal that the in-plane a_1 - a_2 stripe domains at an initial zero field become a single a_1 or a_2 domain under out-of-plane electric field. The $a_1(a_2)$ - c domains coexisting for short time at further out-of-plane electric field, then suddenly switching to a single c domain. The direction of the applied electric field determines the kind of a single a_1 or a_2 domain forms. This is attributed to that the in-plane polarization is slightly out-of-plane. Our domain switching criteria helps an insightful understanding P-E hysteresis loop of ferroelectric BTO.

6.2 Experiment methods

6.2.1 Principle of the polarized light microscope

In tetragonal BTO molecules, the electrons can more easily oscillate parallel to the polarization direction than in the perpendicular direction. The electrons are bound to the molecule and are more restricted in their movement perpendicular to the molecule. Thus, the electrons can absorb EM waves that have a component of their electric field parallel to the molecule. The electrons are much less responsive to electric fields perpendicular to the molecule and allow these fields to pass. As a result, when entering EM wave parallel to the BTO polarization, the observed image domain will show the dark domain, while the bright domain will be observed with perpendicular entering. (Fig. 6.1)

6.2.2 Measurement set-up

The 0.5 mm thick BTO (001) single crystal with one side polished and good surface with average surface roughness of 1 nm provided by the Surface.Net Company were used here. The BTO contains an alternating a_1 - a_2 in-plane stripe domains which was formed upon sample cooling through the ferroelectric Curie temperature ($T_C = 120^\circ\text{C}$). The annealing process is presented in Fig. 2.12. The ferroelastic stripes have a domain width varied from 2 to 6 μm at room temperature.

Ferroelectric BTO domains were imaged using birefringence contrast with the polarizer and analyzer in cross-configuration by the polarization light microscope (section 4.3). The system consisted of the polarization optics, an objective, and a digital camera. A single polarizer was used to identify the polarization axis in the alternating in-plane a_1 and a_2 stripe domains by rotating on the in-plane polarized light direction. We used the polarizing filter property of ferroelectric BTO reflecting the incident linear polarization light to determine the parallel and perpendicular

alignments of the ferroelectric on each domain. The domain-switching processes were observed *in situ* under applying an electric field. The electric field along [001] direction is generated using a high voltage power supply applied on the electrodes, where a 5 nm W layer is the top electrode, and silver paint on the back of BTO is the bottom electrode. The electric field was ramped at 10 V/min and a 100× objective was used. The polarized light microscope measurement setup is shown in the previous chapter (Fig. 4.8)

6.3 Results and discussion

6.3.1 Determination of polarization direction on a_1 and a_2 domains.

To determine the polarization direction of a_1 and a_2 domains, we used a polarized light microscope (PLM) with the setup shown in Fig. 6.1a. The working principle of the PLM is explained in detail in Section 4.3 of Chapter 4. Here, we named the polarization direction of the polarized incident light as P, which can rotate 360°. The angle α is defined as the angle between P and the a_1 - a_2 domain walls.

In the birefringence images shown in Fig. 6.1b, we designated a_1 as the domain with a larger domain width and a_2 as the domain with a smaller domain width. When we rotate P from 0° to 360° (Fig. 6.2), the relative contrast between a_1 and a_2 changes. At $\alpha = 45^\circ$, the a_1 domain appears bright while the a_2 domain appears dark. When α rotates to 90° (or 135°), the relative contrast between a_1 and a_2 is reversed, with the a_1 domain appearing dark and the a_2 domain appearing bright. This phenomenon is similarly observed at $\alpha = 225^\circ$ and 315°.

Using the polarizing properties of BTO to interpret these observations, we can determine the polarization direction of each domain. For example, at $\alpha = 45^\circ$, the a_2 domain appears dark while

the a_1 domain appears bright. This indicates that the polarization of the a_1 domain is perpendicular to P , and the polarization of the a_2 domain is parallel to P (Fig. 6.3).

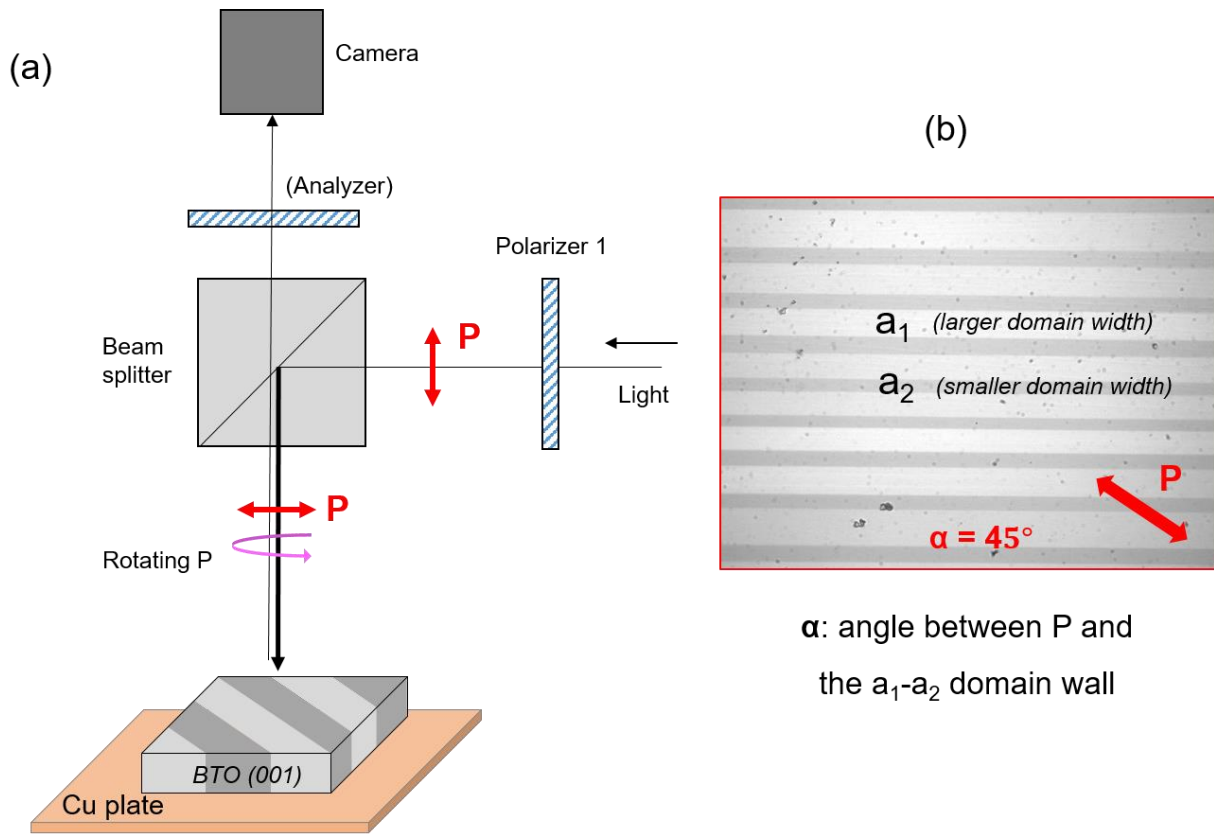


Figure 6.1. (a) Polarized light microscope (PLM) set up. (b) Birefringence images of BTO surface when the polarization of incident light is respect to a_1 - a_2 domain wall of 45° .

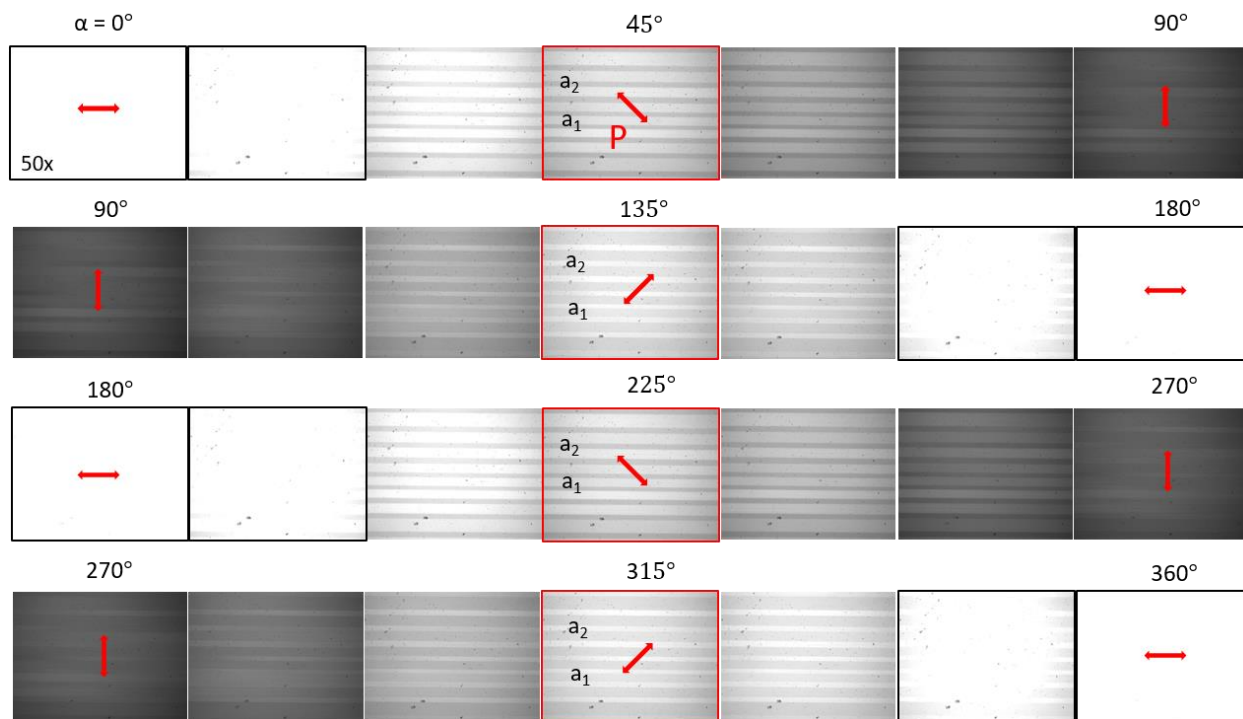


Figure 6.2. The relative contrast between a_1 and a_2 domain under rotating of polarization direction of incident light.

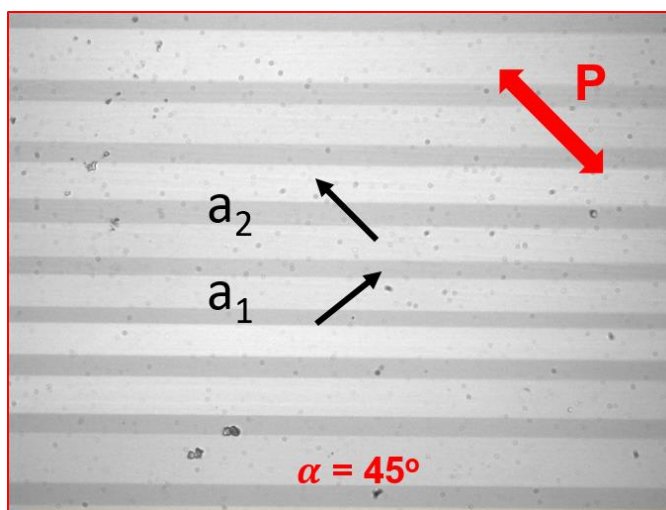


Figure 6.3. Polarization direction of a_1 and a_2 domain with incident polarization direction is respect 45° to domain wall.

6.3.1 Domain switching process of BTO.

Figure 6.4 presents the domain-switching process of BTO under an applied electric field with various application speeds. Normally, when an electric field is applied along the out-of-plane direction of alternating a_1 - a_2 in-plane domains, the a_1 - a_2 domain configuration remains stable up to a field strength of 10 kV/cm. At a higher field strength of 12 kV/cm, the domains rapidly switch to a single c-domain at a rate of 1 kV/cm per minute. However, if the field is applied at a lower rate of 1 kV/cm per 15 minutes, a_1 - a_2 domain-wall movement occurs. Upon increasing the field to 6 kV/cm, some parts of the a_1 - a_2 domains switch to c-domains. Both domain wall movement and domain switching occur simultaneously, resulting in the formation of a single c-domain at a field strength of 10 kV/cm. Interestingly, if the field is applied at a very slow rate, about 1 kV/cm per 5 hours, the domain configuration evolution of BTO is different. In the first step, a_1 - a_2 domain walls gradually move, forming a single a_1 domain. Subsequently, parts of the a_1 domain switch to c-domains. The width of the c-domains then expands, eventually leading to the formation of a single c-domain in the saturation state. However, the interpretation of this observation has not yet been established.

We attempted to reverse the direction of the applied field and observed that the formation of single a_1 and a_2 domains could be controlled by the direction of the applied field. Our next experiment will provide a detailed explanation of this phenomenon.

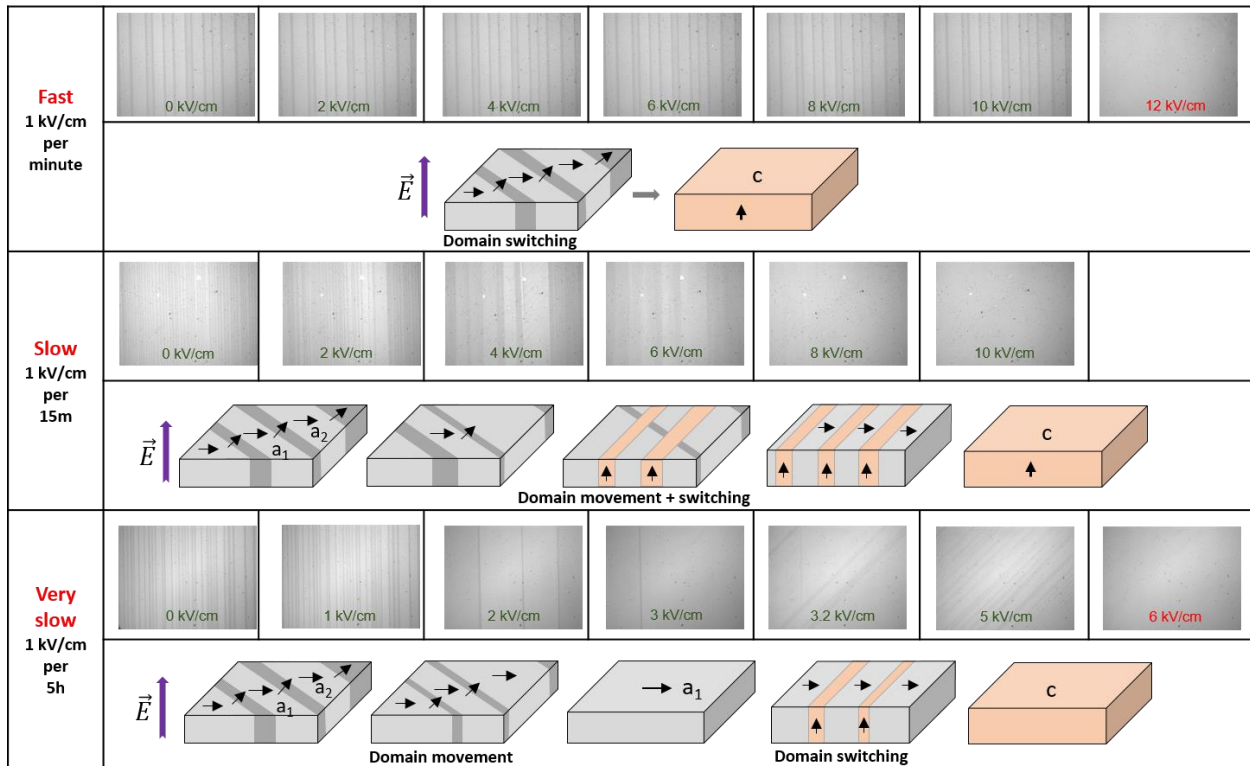


Figure 6.4. Domain-switching process of BTO under applying electric with various speed.

6.3.1 Out-of-plane electric field induces the single in-plane domain in the original alternating in-plane a_1 - a_2 BTO domains.

Figure 6.5a shows the evolution of the BTO in-plane stripe domain under an out-of-plane electric field. The in-plane a_1 , a_2 and the out-of-plane c domains denote the polarization vectors along the [100], [010], and [001] direction, respectively. In the initial state, without external electric field, the BTO surface exhibits alternating a_1 - a_2 in-plane domains with orthogonal polarizations. Their polarization direction configuration is head-to-tail connected to minimize the electrostatic energy at the domain wall.[37] With applying an out-of-plane external electric field, an evolution in initial

in-plane domains is clearly observed. By applying the electric field along to [001] direction (E_+) at 4 kV/cm, there is no obvious change in domain configuration after about 1 hour (not shown in the figure). After 5 hours, the a_1 domains became more and more overwhelming compared to the a_2 domains (Fig. 6.5b).

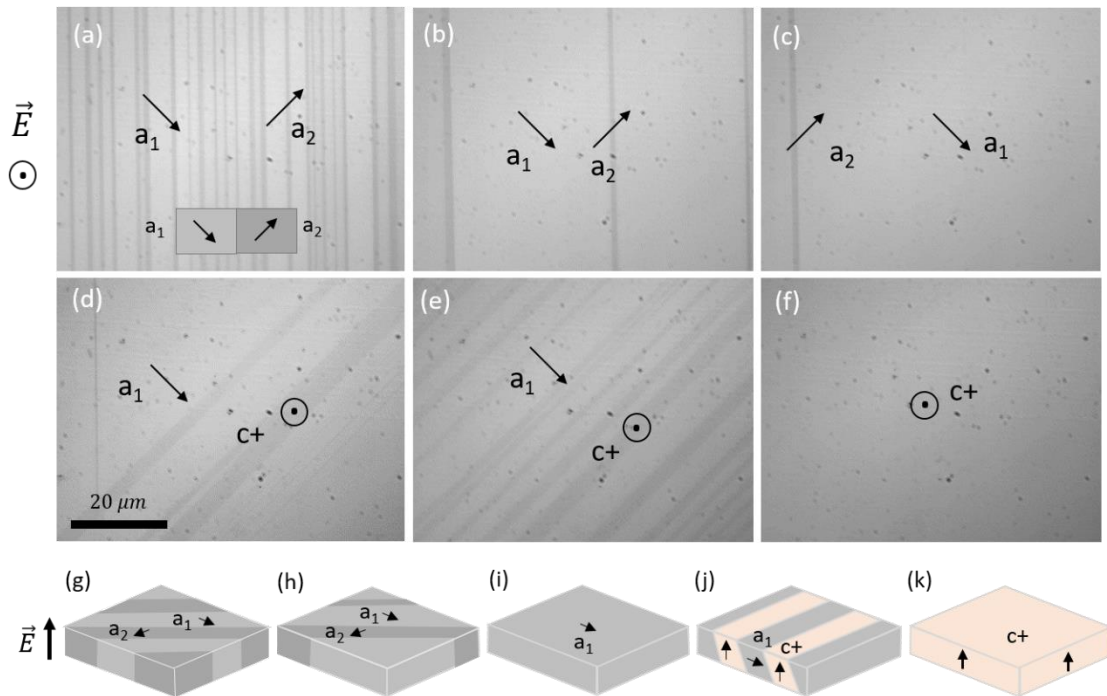


Figure 6.5. (a-f) The alternating a_1 - a_2 stripe ferroelectric domains evolve when an out-of-plane electric field of 0 to 6 kV/cm is applied. The voltage rises at a rate of 10 V/min. The polarization directions of a_1 (gray region) and a_2 (dark region) stripe in-plane domains are indicated by the in-plane arrows. The out-of-plane domain is represented by the letter c , with the polarization direction shown by pointing away from the paper plane. (g-k) Schematic illustration of the observed BTO ferroelectric domain arrangement under applying an out-of-plane electric field (visualized Fig.

6.5a). The image is $100 \times 88 \mu\text{m}$ in size

When increasing the electric field to higher values of 5 kV/cm, the a_2 domains disappeared and the entire BTO surface became a_1 mono-domains (Fig. 6.5c). We were able to observe the threshold electric field value that makes a single domain of roughly 5 kV/cm and a time-keeping of about 10 hours.

When the electric field was continuously increased to 6 kV/cm, the new $c+$ domain (domain with polarization along to [001] direction) suddenly appeared and rapidly grew over time (Fig. 6.5d, e). The entire sample finally became the $c+$ mono-domain, *i.e.*, all polarization directions are oriented to the external electric field, after maintaining for 2 hours at 6 kV/cm (Fig. 6.5f). To visualize the above observation, we provide the sketch of domain-switching process which is illustrated in Fig. 6.5g-k. Firstly, the alternating a_1 and a_2 domain configuration gradually undergoes a domain wall motion to obtain the in-plane mono-domain. Then, the in-plane polarization on the mono-domain rapidly switched on 90° and completely paralleled to the external field direction at the saturation state.

The opposite consequence is obtained when applying electric field to [00-1] direction (E^-). With applying electric field at the low level (-4 kV/cm) and keeping at long time (5 hours), the a_2 domains became more and more overwhelming compared to the a_1 domains (Fig. 6.6b-c). With applying electric field of -5 kV/cm, the new $c-$ domain (domain with polarization along to [00-1] direction) suddenly appeared forming the a_2 - c stripe domain and the $c-$ domain rapidly grew over time (Fig. 6.6d, e). Finally, single $c-$ domain are oriented to the external electric field, after maintaining for 20 minutes at -6 kV/cm. The sketch of domain-switching process by applying E^- is illustrated in Fig. 6.6g-k. Firstly, the alternating a_1 and a_2 domain configuration gradually undergoes a domain wall motion to obtain the in-plane mono-domain. Then, the in-plane

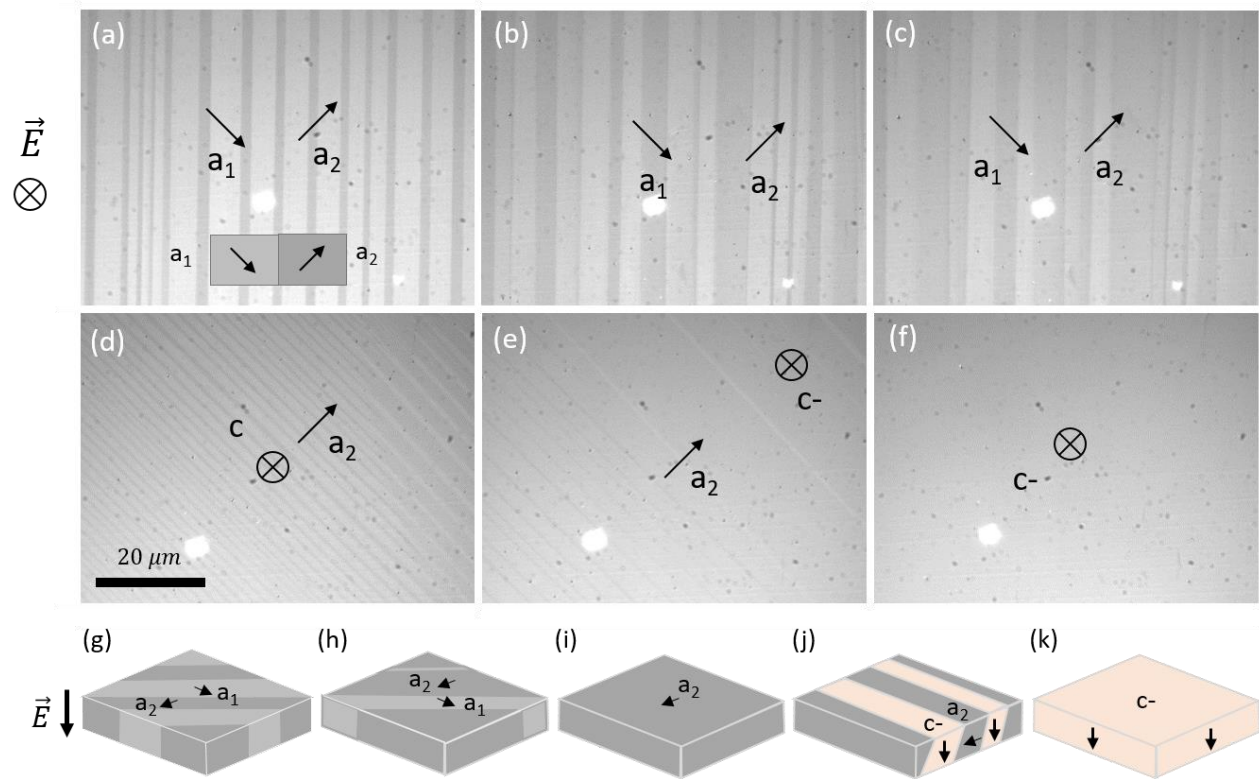


Figure 6.6. (a-f) The alternating a_1 - a_2 stripe ferroelectric domains evolve when an out-of-plane electric field of 0 to -6 kV/cm is applied. The voltage rises at a rate of 10 V/min. The polarization directions of a_1 (gray region) and a_2 (dark region) stripe in-plane domains are indicated by the in-plane arrows. The out-of-plane domain is represented by the letter c , with the polarization direction shown by the arrows pointing in the paper plane. (g-k) Schematic illustration of the observed BTO ferroelectric domain arrangement under applying an out-of-plane electric field (visualized Fig. 6.3a).

The images size of $100 \times 88 \mu m$.

polarization on the mono-domain rapidly switched on 90° and completely paralleled to the external field direction at the saturation state. By confirming the measurement on many samples, we witnessed that the single in-plane polarization can be induced by simply applying an out-of-plane electric field on the alternative in-plane domains. This is attributed to the in-plane polarization being tilted a few degrees to out-of-plane, i.e. herein, a_1 domain polarization tilts to $[001]$ direction and that of a_2 domain tilts to $[00-1]$ direction. Our findings on the domain switching steps of BTO are remarkably different with previous report, where the domains are immediately oriented to the external electric field without extension of the in-plane domains.[38]

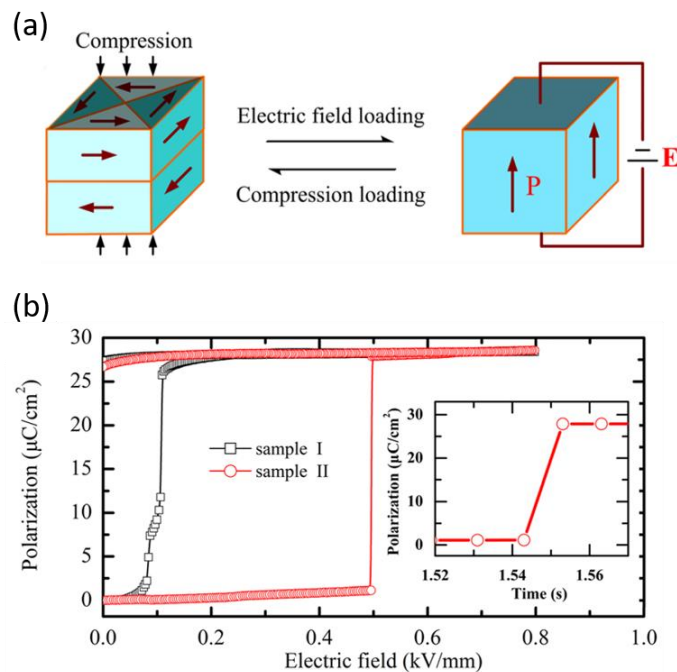


Figure 6.7. (a) 90° domain switch of BTO without domain wall motion. (b) Polarization – Electric field loop of BTO. The loop of sample I exhibit the 90° domain switching with domain wall motion. While, that of Sample II is without domain wall motion.[38]

These observations can be explained by the 90° domain switching behavior. To directly switch in-plane polarization to out-of-plane, we need apply the critical electric field of 5 kV/cm to out-of-plane sample, as shown in Fig. 6.7a and b.[38] If an applied field value is smaller than the value of this critical field, Ti atoms inside the tetragonal unit cell of BTO does not have enough energy to switch to out-of-plane. However, we expected that they is free to move among 4 positions in the in-plane (Fig. 6.8a). In the case the applied electric field value is larger than that of the critical field, Ti atoms can directly switch to out-of-plane to become c domain (Fig. 6.8b).

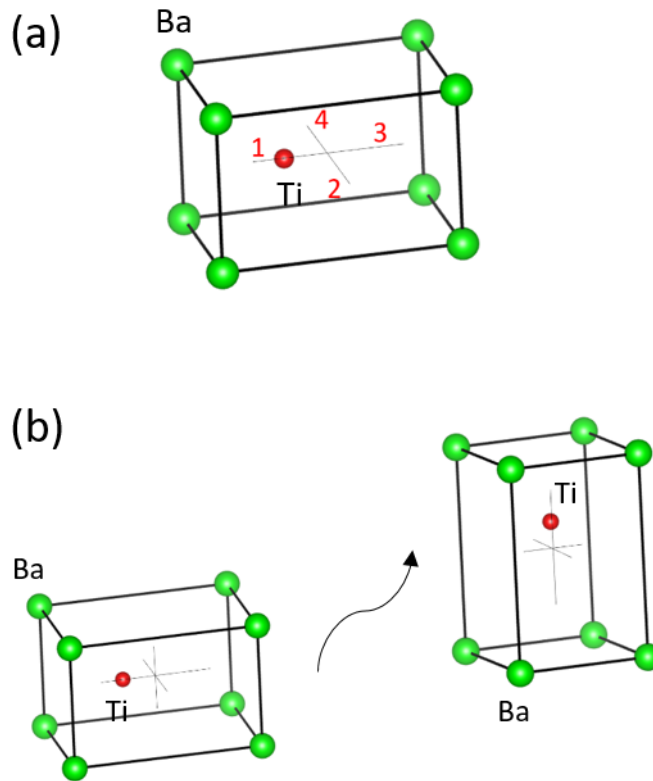


Figure 6.8. Tetragonal unit cell of BTO in the cases: (a) the applied electric field value is smaller than that of the critical field. (b) the applied electric field value is larger than that of the critical electric field.

5.3.2 The evolution of the single c domain under parallel and antiparallel out-of-plane electric field.

To better understand the process of BTO domain evolution, an antiparallel field is applied to sample at a remanent state (after removing electric field from the saturation state). As shown in Fig. 6.9a, the alternating a - c^+ stripe domain configuration appears at zero field to minimize electrostatic energy. Herein, the polarizations of c^+ and a_1 domains are head-to-tail connected and perpendicular to each other (Fig. 6.9b). When the electric field is applied antiparallel to [001] direction, the a_1 domain stripes expanded due to the movement of the domain walls. For a long-time duration, the width of the c^+ domains decrease while that of a_1 domain increases (Fig. 6.9c). After applying an electric field level of -3.2 kV/cm, the whole measured region becomes the single a_1 domain (Fig. 6.9 d). As continuously increasing electric field level of -4 kV/cm, several new c^- domain stripes with polarization paralleled to the external field direction appeared. Subsequently, the c^- domain width becomes larger and larger, whereas the width of a_1 domains decreases simultaneously (Fig. 6.9e). Finally, the c^- mono-domain is observed at an electric field level of -5 kV/cm (Fig. 6.9f). In this experiment, each electric field level is maintained for 30 minutes. Obviously, the 180° domain-switching consisting of two 90° switching steps under an applied antiparallel electric field is observed, which is well agreed to the earlier report.[36] For visualizing the domain switching process of BTO under an applied antiparallel electric field, we sketch a domain configuration evolution shown in Fig. 6.9g-k. Shortly, this domain-switching process can be divided into the two steps. Firstly, the polarization vector of the c^+ domains switched on 90° to single in-plane domain with polarization perpendicular to the external electric field. Secondly, the single in-plane polarization vectors switched on 90° once again to become the single c^- domain with polarizations along with the external electric field. As a result, the 180° domain-switching is completed by two-step 90° domain switching under an antiparallel electric field.

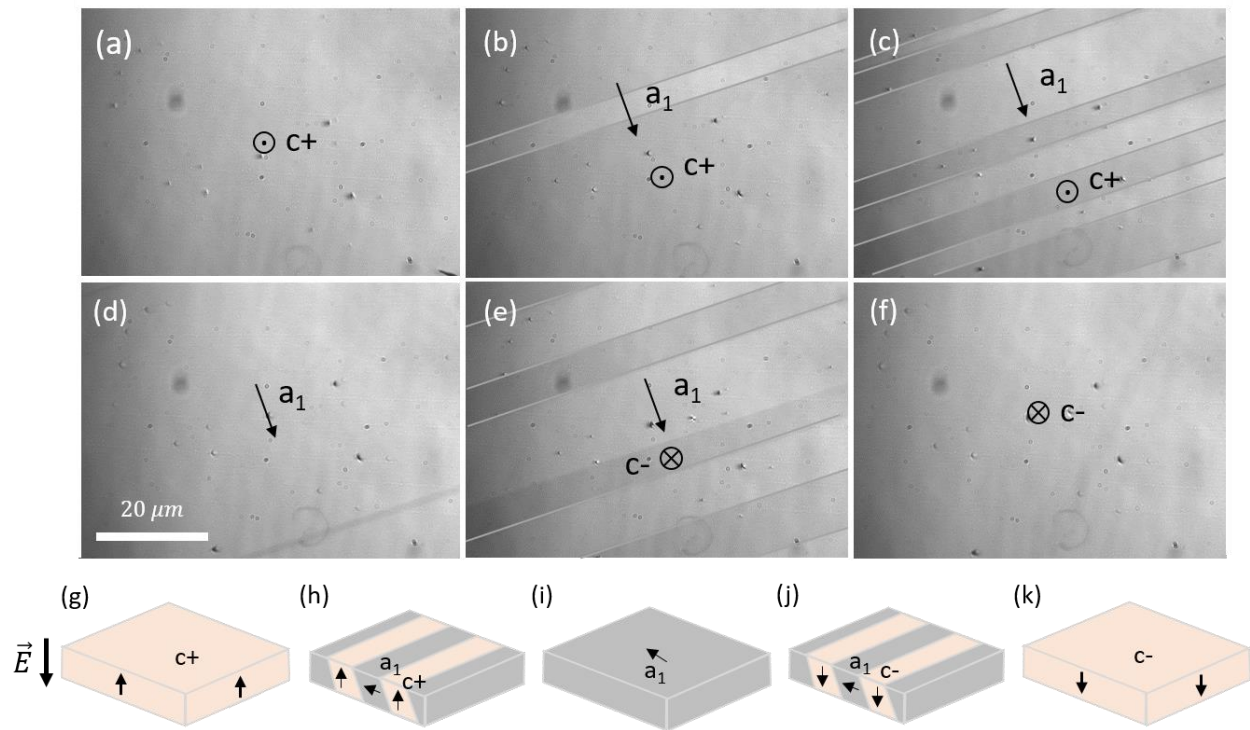


Figure 6.9. (a) The evolution of the single c domain under parallel and antiparallel out-of-plane electric field modulating from 6 to -6 kV/cm. The voltage rises at a rate of 10 V/min. The $c+$, $c-$ with \odot and \otimes denote the domain having the out-of-plane and anti-parallel-out-of-plane polarization direction pointing out and in the paper plane, respectively. The a_1 represents the in-plane domain having the polarization directions shown by the arrows. (b) Schematic illustration of the ferroelectric domain configuration under antiparallel out-of-plane electric field (visualized Fig. 6.9a). The images size of $100 \times 88 \mu\text{m}$.

Our observation can be explained by 180° domain switch behavior as shown in Fig. 6.10. Figure 6.10a present the tetragonal unit cell with Ti atom located at off-center inside the unit cell. To do 180° domain switching process, Ti atom need to switch from c+ to c- position, as shown in Fig. 6.10b. To Ti atom can switch from c+ to c- position, there are 4 paths. The first one, Ti can directly switch from c+ to c-. Other way is jumping to position A before jumping to position c-. The calculation shown that energy to directly Ti from c+ to c- is much larger than that for the way jumping to position A (Fig. 6.10c). The critical field from two-step 90° domain switching is 7.44 kV/cm and that for 180° domain switching is 24.35 kV/cm. If the applied field range from 7.44 kV/cm to 24.35 kV/cm, the 180° domain switching occurs by two-step 90° domain switching.

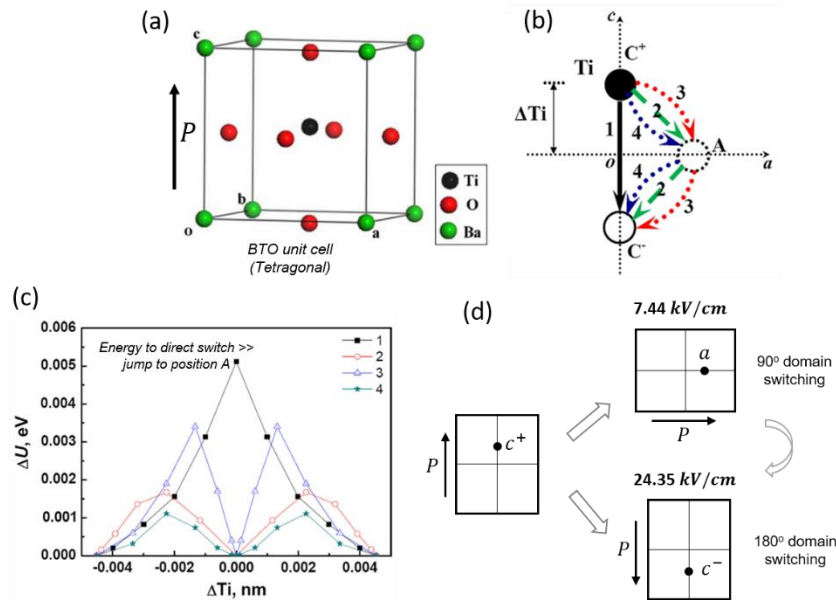


Figure 6.10. (a) Tetragonal BTO unit cell, (b) Ti atoms switch from c+ to c- domain by 4 paths.

In path 1, Ti atom can directly switch from c+ to c- position. In path 2, 3, and 4, Ti atom can jump to position A, then continuously jump to position c-.

(c) The critical field for 90° and 180° domain switching of BTO.[39]

5.3.3 Insightful understanding F-E hysteresis loop of BTO under applying electric field.

We collect the domain evolution of ferroelectric BTO under applying electric field to provide an overview of the P-E hysteresis loop (Fig. 6.11).

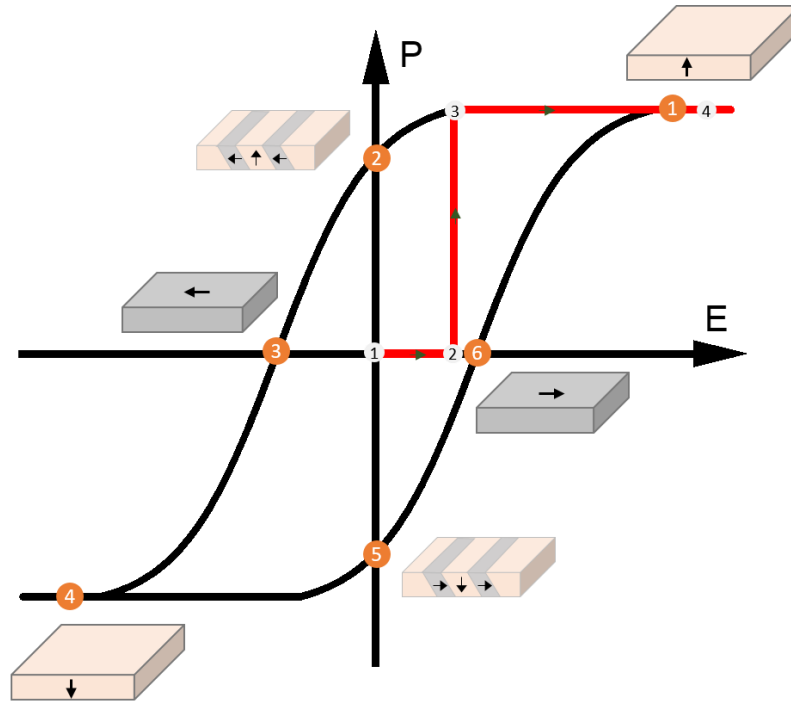


Figure 6.11. The summarized polarization – electric field (P-E) hysteresis loop of ferroelectric BTO from current studies. The red curve shows the polarization and electric field dependence from the virgin state to the saturation state. The tiny arrows and the number on the red curve show the direction of data observation. The numbers (orange circles) on hysteresis loop represent an order of measurement and corresponding position of the BTO domain with applying the antiparallel out-of-plane electric field on the c domain. The arrows on the sketched unit cell represent the polarization direction.

The ferroelectric BTO domain configuration exhibits an alternating in-plane stripe domain at the virgin state (red curve). At low electric fields applying on an out-of-plane, the domain wall motion induces the in-plane mono-domain, resulting in no change of the polarization value. With further increasing electric field, 90° domain-switching induces the out-of-plane monodomain, leading to the suddenly increase of polarization value up to the saturation state. With an applied antiparallel electric field, the out-of-plane mono-domain will be switched to the in-plane mono-domain and switched once again to become the opposite out-of-plane mono-domain. Consequentially, the 180° domain-switching is observed here through the two 90° switching steps. The P-E hysteresis loop exhibits the dependency of polarization as a function of electric field in this domain switching process (Fig. 6.11).

6.4 Conclusion

In summary, the domain-switching process of ferroelectric BTO is obviously demonstrated on our report. The single in-plane domain is realized by applying the low electric field with out-of-plane direction on the alternating in-plane stripe domains. With a higher field, the BTO domains suddenly switch on 90° from the single in-plane domain to the single out-of-plane BTO domain. They result in all polarizations orient to the external electric field direction. To switch the polarization of the single domain from the out-of-plane to the antiparallel-out-of-plane direction, we use the low electric field with antiparallel out-of-plane direction for a long time-keeping. They exhibit that the 180° domain-switching through the two 90° domain-switching steps via the slow domain wall motion is investigated in this process. These results can be explained in terms of reducing energy in BTO during the poling process. Our report especially provided an understanding of the domain-switching criteria that is practically useful for applying and designing ferroelectric applications.

6.5 References

- [1] K. Eshraghian, “Evolution of Nonvolatile Resistive Switching Memory Technologies: The Related Influence on Hetrogeneous Nanoarchitectures,” *Trans. Electr. Electron. Mater.*, vol. 11, no. 6, pp. 243–248, 2010.
- [2] R. Ramesh and L. W. Martin, “Electric field control of magnetism: multiferroics and magnetoelectrics,” *Riv. del Nuovo Cim.*, vol. 44, no. 5, pp. 251–289, 2021.
- [3] R. Ramesh and N. A. Spaldin, “Multiferroics: Progress and prospects in thin films,” *Nanosci. Technol. A Collect. Rev. from Nat. Journals*, vol. 3, pp. 20–28, 2009.
- [4] S. M. Yakout, “Spintronics: Future Technology for New Data Storage and Communication Devices,” *J. Supercond. Nov. Magn.*, vol. 33, no. 9, pp. 2557–2580, 2020.
- [5] J. Ma, J. Hu, Z. Li, and C. W. Nan, “Recent progress in multiferroic magnetoelectric composites: From bulk to thin films,” *Adv. Mater.*, vol. 23, no. 9, pp. 1062–1087, 2011.
- [6] C. Lu, M. Wu, L. Lin, and J. M. Liu, “Single-phase multiferroics: New materials, phenomena, and physics,” *Natl. Sci. Rev.*, vol. 6, no. 4, pp. 653–668, 2019.
- [7] J. J. Wang, F. Y. Meng, X. Q. Ma, M. X. Xu, and L. Q. Chen, “Lattice, elastic, polarization, and electrostrictive properties of BaTiO₃ from first-principles,” *J. Appl. Phys.*, vol. 108, no. 3, 2010.
- [8] T. Mion, D. M. Potrepka, F. J. Crowne, A. Tauber, and S. C. Tidrow, “Dielectric and X-ray diffraction analysis of Ba(Ga,Ta)_{0.05}Ti_{0.90}O₃,” *Ferroelectrics*, vol. 473, no. 1, pp. 13–23, 2014.
- [9] “26.” .

- [10] S. Brivio, C. Rinaldi, D. Petti, R. Bertacco, and F. Sanchez, “Epitaxial growth of Fe/BaTiO₃ heterostructures,” *Thin Solid Films*, vol. 519, no. 17, pp. 5804–5807, 2011.
- [11] T. Mikolajick *et al.*, “Next generation ferroelectric materials for semiconductor process integration and their applications,” *J. Appl. Phys.*, vol. 129, no. 10, 2021.
- [12] J. F. Scott, “Applications of modern ferroelectrics,” *Science (80-.)*, vol. 315, no. 5814, pp. 954–959, 2007.
- [13] T. Y. Kim, S. K. Kim, and S. W. Kim, “Application of ferroelectric materials for improving output power of energy harvesters,” *Nano Converg.*, vol. 5, no. 1, pp. 1–16, 2018.
- [14] L. W. Martin and A. M. Rappe, “Thin-film ferroelectric materials and their applications,” *Nat. Rev. Mater.*, vol. 2, no. 2, 2016.
- [15] S. Zhang, B. Malič, J. F. Li, and J. Rödel, “Lead-free ferroelectric materials: Prospective applications,” *J. Mater. Res.*, vol. 36, no. 5, pp. 985–995, 2021.
- [16] S. Wada, K. Yako, K. Yokoo, H. Kakemoto, and T. Tsurumi, “Domain wall engineering in barium titanate single crystals for enhanced piezoelectric properties,” *Ferroelectrics*, vol. 334, no. 1 PART 2, pp. 17–27, 2006.
- [17] L. S. R. Rocha *et al.*, “A study approach on ferroelectric domains in BaTiO₃,” *Mater. Charact.*, vol. 120, pp. 257–262, 2016.
- [18] T. H. E. Lahtinen, K. J. A. Franke, and S. Van Dijken, “Electric-field control of magnetic domain wall motion and local magnetization reversal,” *Sci. Rep.*, vol. 2, pp. 1–6, 2012.

- [19] F. Rubio-Marcos, A. Del Campo, P. Marchet, and J. F. Fernández, “Ferroelectric domain wall motion induced by polarized light,” *Nat. Commun.*, vol. 6, 2015.
- [20] Z. K. Zhang, D. N. Fang, and A. K. Soh, “A new criterion for domain-switching in ferroelectric materials,” *Mech. Mater.*, vol. 38, no. 1–2, pp. 25–32, 2006.
- [21] V. Boddu, F. Endres, and P. Steinmann, “Molecular dynamics study of ferroelectric domain nucleation and domain switching dynamics,” *Sci. Rep.*, vol. 7, no. 1, pp. 1–10, 2017.
- [22] M. G. Shaikh, S. Phanish, and S. M. Sivakumar, “Domain switching criteria for ferroelectrics,” *Comput. Mater. Sci.*, vol. 37, no. 1–2, pp. 178–186, 2006.
- [23] X. Chao, J. Wang, J. Pu, S. Zhang, and Z. Yang, “Aging behavior and electrical properties of low-temperature sintered (Ba, Ca)(Ti, Zr)O₃-Ba(Cu, W)O₃ ceramics and plate loudspeaker,” *Sensors Actuators, A Phys.*, vol. 237, pp. 9–19, 2016.
- [24] M. Yuan *et al.*, “Biocompatible nanogenerators through high piezoelectric coefficient 0.5Ba(Zr_{0.2}Ti_{0.8})O₃-0.5(Ba_{0.7}Ca_{0.3})TiO₃ nanowires for in-vivo applications,” *Adv. Mater.*, vol. 26, no. 44, pp. 7432–7437, 2014.
- [25] N. R. Alluri, B. Saravanakumar, and S. J. Kim, “Flexible, hybrid piezoelectric film (BaTi(1-x)ZrxO₃)/PVDF nanogenerator as a self-powered fluid velocity sensor,” *ACS Appl. Mater. Interfaces*, vol. 7, no. 18, pp. 9831–9840, 2015.
- [26] X. Yan *et al.*, “Correspondence: Lead-free intravascular ultrasound transducer using BZT-50BCT ceramics,” *IEEE Trans. Ultrason. Ferroelectr. Freq. Control*, vol. 60, no. 6, pp. 1272–1276, 2013.

- [27] M. Goiriena-Goikoetxea *et al.*, “Influence of dislocations and twin walls in BaTiO₃ on the voltage-controlled switching of perpendicular magnetization,” *Phys. Rev. Mater.*, vol. 5, no. 2, 2021.
- [28] M. He, M. Wang, and Z. Zhang, “Electric-field-induced domain intersection in BaTiO₃ single crystal,” *Jpn. J. Appl. Phys.*, vol. 56, no. 3, 2017.
- [29] M. Acosta *et al.*, “BaTiO₃-based piezoelectrics: Fundamentals, current status, and perspectives,” *Appl. Phys. Rev.*, vol. 4, no. 4, 2017.
- [30] L. B. and G. J. S. Bo-Kuai Lai, Inna Ponomareva, Igor A. Kornev, “Domain evolution of BaTiO₃ ultrathin films under electric field: a first-principles study Bo-Kuai Lai, Inna Ponomareva, Igor A. Kornev, L. Bellaiche and G. J. Salamo Physics Department, University of Arkansas, Fayetteville, Arkansas 72701.”
- [31] K. J. A. Franke, T. H. E. Lahtinen, A. Casiraghi, D. L. González, S. J. Hämäläinen, and S. van Dijken, “Electric field control of magnetism based on elastically coupled ferromagnetic and ferroelectric domains,” *Nanoscale Ferroelectr. Multiferroics Key Process. Charact. Issues, Nanoscale Eff. 2 Vol.*, pp. 678–699, 2016.
- [32] P. R. Potnis, N. T. Tsou, and J. E. Huber, “A review of domain modelling and domain imaging techniques in ferroelectric crystals,” *Materials (Basel)*, vol. 4, no. 2, pp. 417–447, 2010.
- [33] J. E. Rault, T. O. Menteş, A. Locatelli, and N. Barrett, “Reversible switching of in-plane polarized ferroelectric domains in BaTiO₃ (001) with very low energy electrons,” *Sci. Rep.*, vol. 4, pp. 1–7, 2014.

- [34] C. M. Landis, “Non-linear constitutive modeling of ferroelectrics,” *Curr. Opin. Solid State Mater. Sci.*, vol. 8, no. 1, pp. 59–69, 2004.
- [35] D. Damjanovic, “Contributions to the piezoelectric effect in ferroelectric single crystals and ceramics,” *J. Am. Ceram. Soc.*, vol. 88, no. 10, pp. 2663–2676, 2005.
- [36] B. Jiang, Y. Bai, W. Chu, Y. Su, and L. Qiao, “Direct observation of two 90° steps of 180° domain switching in BaTiO₃ single crystal under an antiparallel electric field,” *Appl. Phys. Lett.*, vol. 93, no. 15, pp. 1–4, 2008.
- [37] K. J. A. Franke, D. López González, S. J. Hämäläinen, and S. Van Dijken, “Size dependence of domain pattern transfer in multiferroic heterostructures,” *Phys. Rev. Lett.*, vol. 112, no. 1, pp. 1–5, 2014.
- [38] Y. W. Li, J. F. Scott, D. N. Fang, and F. X. Li, “90-degree polarization switching in BaTiO₃ crystals without domain wall motion,” *Appl. Phys. Lett.*, vol. 103, no. 23, 2013.
- [39]

CHAPTER 7: ELECTRIC FIELD CONTROL OF MAGNETIC ANISOTROPY OF Fe FILM ON ALTERNATING a_1 - a_2 BTO DOMAINS

Electric field (E) control of the magnetic anisotropy in Fe epitaxial thin film grown on BaTiO₃ substrate (BTO) is demonstrated at room temperature. The a BTO domain have an in-plane polarization, while the c BTO domain have an out-of-plane polarization. The magnetic domain configuration is an exact imprinting from the ferroelectric domain structure of the BTO during growth. In more detail, the Fe film on a domains exhibits uniaxial magnetic anisotropies with the easy axis is along with [100]-BTO directions. While the biaxial magnetic anisotropy with the easy axis is along with [100]- and [110]-BTO is obtained when Fe film is grown on top of c domain. Under an applied out-of-plane electric field, the alternating a_1 - a_2 or a-c BTO domain configuration is modulated to the new domain configuration. Interesting, these domain configuration change correspond to the modulation of magnetic easy axis of the Fe film. The mechanism of the observation is attributed to the strain transfer induced from the inverse magnetostriction effect during applying electric field to Fe/BTO film. The pinning of inter-ferroic domain walls is persisted during the polarization process, resulting in a magnetic domain wall motion under applying electric field.

7.1 Introduction

In spintronic devices, the magnetic switching and magnetic domain wall motion of ferromagnetic (FM) materials are controlled by applied magnetic field and injected spin-polarized current. However, these traditional methods consume high energy due to inevitable energy loss. Therefore, searching for magnetic field and spin-polarized current free spintronic devices is an imperative research field. Electric field control of magnetization switching is a good candidate for this purpose since the lack of an applied electric current, causing energy loss.[1-5] Multiferroics possessing both ferroelectric and ferromagnetic order are promising materials for realizing electric field control magnetic properties in spintronic devices because of their magnetoelectric (ME) effect. The ME effect is defined as the electric polarization induced by applied magnetic field and vice versa as the magnetization induced by applied electric field. So far, the electric field control magnetism has been reported in many single-phase multiferroics such as BiFeO_3 , BiMnO_3 , and YMnO_3 . [6-9] However, the weak magneto-electric coupling between ferroelectric and ferromagnetic order parameters and the low Curie temperature of a single-phase multiferroics limit the device's efficiency.

Recently, multiferroics heterostructures, i.e., FM/FE heterostructures combining both ferromagnetic and ferroelectric materials are of interest. This structure enables us to achieve strong magnetoelectric coupling at interface via elastic coupling between the two ferroic phases. In principle, the ferroelectric material is elastically strained under an applied electric field due to the inverse piezoelectric effect. This elastic strain is well transferred from ferroelectric into the ferromagnetic due to the strong elastic coupling between them, especially in epitaxial interfaces. Owing to the inverse magneto-restriction, the magnetic anisotropy of the ferromagnetic is modulated. As a result, we can use electric field to modulate the magnetic anisotropy of the

ferromagnetic. On the other hand, the FM/FE heterostructures also allow us to individually optimize ferroelectric and ferromagnetic properties in each ferroic. The switching of a FM order by an applied electric field without magnetic fields and spin-polarized current using has been demonstrated in many hybrid structures such as $\text{Fe}_3\text{O}_4/\text{BTO}$, Co/BTO , and FeCo/BTO . [10-14] Besides, due to the pinning neighboring ferroic domains, the ferroelectric domain is adjusted by applying an external electric field results in domain wall motion in FM.

Among many FE/FM heterostructures, Fe/BTO is one of the most potential FE/FM heterostructures because of the intimate interface connection existing between the Fe and BTO and the small lattice mismatch of $\sim 1.3\%$. Additionally, BTO is an attractive ferroelectric material due to its polymorphism and interesting ferroelectric domain configuration. These heterostructures also exhibit the ferroic orders at room temperature. To date, there have been many reports on the manipulation of magnetization in Fe/BTO heterostructures by thermal and electrical means. [15-26] However, they are lack a thoroughly study about a full understanding of the strain-driven magnetic anisotropy of an Fe film in evolution polarization direction of BTO under applying electric field. In this study, we show clear experimental evidence for the strain-induced magnetic anisotropy of Fe film in Fe/BTO heterostructures in zero and under applying electric field, giving a significant impact on designing next generation applications at ultra-low energy consumption.

7.2 Experiment methods

We deposited a 10 nm thick epitaxial Fe film on a BTO (001) substrate by molecular beam epitaxy (MBE) under a base pressure of $\sim 10^{-9}$ Torr. The cleaned BTO substrate was pre-heated at 600 °C in ultra-high vacuum to remove residual impurities. After that, the substrate was cooled down to 300 °C for growth, where the BTO is present in its cubic phase. The Fe was deposited at an

evaporation rate of 0.1 Å/s using a Fe effusion cell (Effucell Inc.), the rate is determined by a quartz crystal thickness monitor. The quality of the substrate and the film was monitored by an *in-situ* reflection high energy electron diffraction (RHEED). X-ray diffraction (XRD) was used for crystal structure determination. The ferroelectric and ferromagnetic domains were imaged independently using optical polarization microscopy. The ferroelectric BTO domains were imaged using birefringence contrast with the polarizer and analyzer in cross-configuration. The magnetic domain patterns were measured using the magneto-optical Kerr effect (MOKE). Local magnetic hysteresis curves were constructed from the evolution of magnetic contrast in single domain areas during magnetization reversal. Electric fields were generated by using the Fe films as top electrode and the silver paste on the back side of the BTO substrate as bottom electrode.

7.3 Results and discussions

7.3.1 Electric field control of magnetic anisotropy in epitaxial Fe on a1-a2 BTO domains

7.3.1.1 Epitaxial Fe/BTO thin film

Figure 7.1a shows the RHEED patterns of BTO substrate and Fe film taken along [110] and [100] azimuth of BTO substrate. Streaky RHEED pattern of BTO substrate indicates clean and flat surface. The line RHEED pattern of Fe film indicates the epitaxial with film's growth mode is layer by layer. The epitaxial relationship of Fe film on BTO is $[110]_{\text{Fe}}/[100]_{\text{BTO}}$. To characterize crystal structure of grown Fe/BTO film, we performed the room-temperature θ -2 θ XRD measurement (Fig. 7.1b). A set of (001)/(100); (002)/(200), and (003)/(300) reflection peaks at $2\theta \sim 22^\circ, 45^\circ$ and 70° , respectively, from the BTO substrate insists on the coexistence of multi stripe domains on tetragonal BTO at room temperature. Besides, the only Fe (200) orientation at the diffraction peak at 65.05° is observed, indicating that the obtained Fe film is single crystal. The

out-of-plane lattice parameters Fe of 2.874 Å is estimated which is larger than bulk one ($a_{\text{Fe}} = 2.870 \text{ \AA}$) corresponding to Fe film under compressive strain along in-plane.

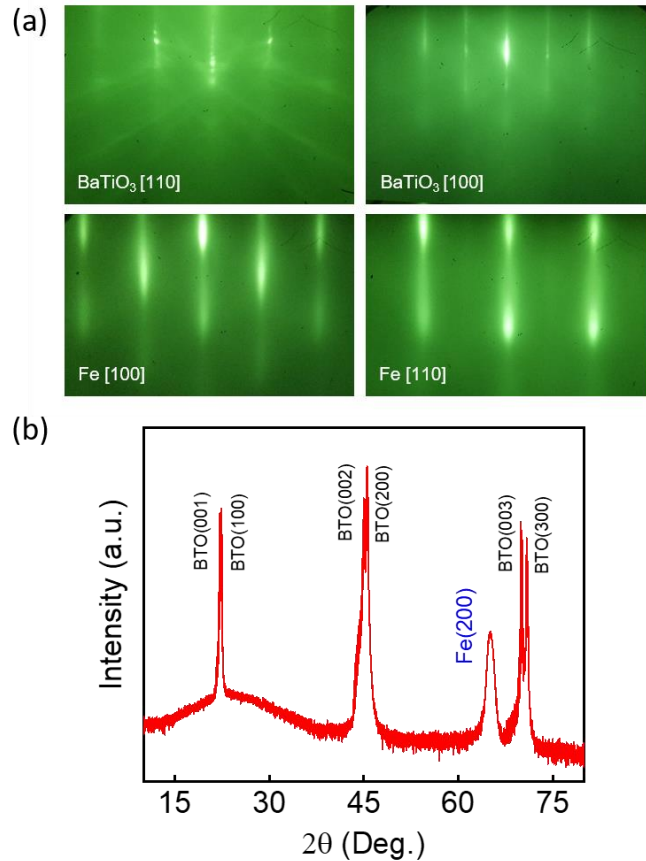


Figure 7.1. (a) RHEED patterns of BTO substrate and Fe films at growth temperature of 300 °C.

(b) Room temperature XRD pattern of 10 nm Fe thin film formed on BTO substrate.

7.3.1.2 Magnetic anisotropy of Fe film grown on a₁-a₂ BTO domains

Full imprinting of ferroelectric domain of the BTO into the Fe film at room temperature in zero electric field is illustrated in Fig. 7.2. Figure 7.2a shows the schematic illustration of ferroelectric domain configuration and the ferroelectric microstructure image of BTO. The average width of

ferroelectric stripe domains in the sample are 3 to 6 μm . The ferroelastic domain pattern of the BTO consists of alternating a_1 (gray) and a_2 (dark) stripe domains with in-plane polarization directions and their polarization are orthogonal each other. The BTO polarization direction of the a_1 , and a_2 are along with [100] and [010], respectively. Ferromagnetic domain of the Fe thin film on top of BTO is an exact copy of the ferroelastic domain pattern which is stripe shape ferromagnetic domain as shown in Fig. 7.2b. The arrows indicate the determined polarization directions in each stripe ferroelastic domain, while the double head arrows indicated the determined magnetic easy axes in each stripe ferromagnetic domain. Here, one-to-one copies of ferroelectric stripes are produced through interface strain coupling, which causes the distinct magnetic responses in the Fe film on top of the a_1 and a_2 domains. These drawings are extracted by the measurement result in Fig. 7.2.

Figure 7.3 shows a polar plot of the normalized remnant magnetization (M_R/M_S) and coercivity (H_C) for both stripe domains, and several local magnetization curves for different applying magnetic field angles (α). The α is angle between the applied magnetic field and the stripe domain walls. At $\alpha = 45^\circ$, a square magnetization curve is observed on the a_1 domain with $M_R/M_S \sim 1$ implying the magnetic easy axis, whereas the a_2 domain shows the magnetic hard axis with $M_R/M_S \sim 0$. Oppositely, at $\alpha = 135^\circ$, the a_1 domain magnetization curve indicates a magnetic hard axis while the a_2 domain magnetization curve indicates a magnetic easy axis. The twofold symmetry of the magnetoelastic anisotropy and the near orthogonal alignment of the uniaxial magnetic easy axis in the a_1 and a_2 domains are confirmed by the polar plot of the M_R/M_S . Noticeable in Fig. 7.3a, the switching fields (H_C) of Fe film on each a_1 and a_2 domains as a function of magnetic field angle (α) are abnormal curve. According to the Stonner-Wohlfarth theory, a maximum H_C is obtained when the field is applied along the uniaxial magnetic easy axis.[27] However, our sample shows

unusual polar plot of H_C due to strong coupling between the neighboring a_1 - a_2 stripe ferromagnetic domains.

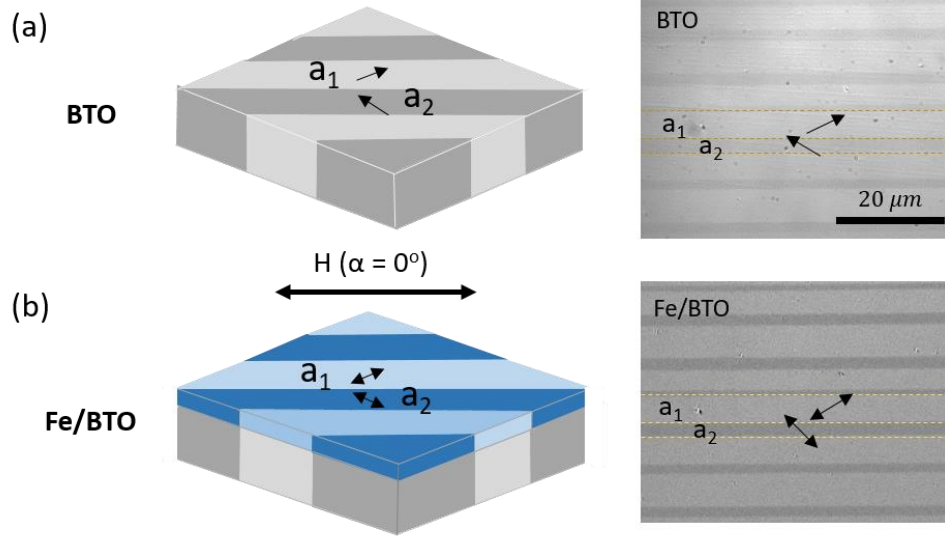


Figure 7.2. (a) Schematic illustration of the ferroelastic domain pattern of a cleaned BTO (001) substrate (left) and its ferroelectric (FE) microstructure after Fe film growth (right). (b) Schematic illustration of the magnetic domain configuration of Fe/BTO film (left) and its MOKE image (right). The arrows in (a) indicate the direction of ferroelectric polarization, and the double-headed arrows in (b) represent the magnetic easy axes.

To confirm the magnetic anisotropy of the film, we compared it to the theoretical estimation. The magnetoelastic anisotropy energy density (K_{me}) of Fe film on top of BTO can be written as: [28]

$$K_{me} = B_1(e_{xx}\alpha_x^2 + e_{yy}\alpha_y^2) + B_2e_{xy}\alpha_x\alpha_y \quad (7.1)$$

Here, B_1 and B_2 are the magnetoelastic coupling coefficients, e_{xx} and e_{yy} are the strains along the cubic axes ([100]-Fe and [010]-Fe), e_{xy} is the shear strain along the diagonal [110]-Fe direction,

and α_x and α_y are the directions cosines with respects to [100]-Fe and [010]-Fe. On the top of the ferroelastic a domains, the in-plane Fe lattice exhibits a diamond shape due to a shear strain along [110]-Fe. To calculate K_{me} along to [110]-Fe, we consider to the second term in Eq. 7.1. We can calculate K_{me} of the film on [110]-Fe with using $B_2 = 7.83 \times 10^6 \text{ J/m}^3$, $e_{xy} = 1\%$, and $\alpha_x = \alpha_y = 1/\sqrt{2}$, this calculation yields $K_{me} = 3.9 \times 10^4 \text{ J/m}^3$. Since K_{me} of the Fe film along [110]-Fe is lower than that of other directions, thus it is magnetically easy or the uniaxial magnetic easy axis is oriented to the [110] direction. Besides, by fitting the slope and saturation field of the hard axis hysteresis curves, we can determine the strength of the magnetoelastic anisotropy of the growth film ($M_s/2K_{me}$) with using the saturation magnetization of Fe film is $M_s = 1.7 \times 10^6 \text{ A/m}$. This calculation gives $K_{me} = 3.5 \times 10^4 \text{ J/m}^3$. The close agreement between the calculation and experimentally measured uniaxial magnetoelastic anisotropy indicates that the ferroelastic strain of the BTO substrate is fully transferred to the epitaxial Fe films after MBE growth.

7.3.1.3 The pinning strength between ferroic domains

In order to investigate the pinning strength between ferroic domains, longitudinal MOKE images and hysteresis loop of Fe film have been conducted. Figure 7.4 shows the magnetization reversal process of Fe/BTO with an applied magnetic field (H) direction of $\alpha = 0^\circ$ (H // the stripe domain). At high magnetic field of $H = -200 \text{ Oe}$, the MOKE image shows the dark color (1), indicating that the saturation magnetization state on both a_1 and a_2 domains are obtained; the magnetization direction along with the right hand-side direction.

When the field is removed, applying the magnetic field in the opposite direction (2), the stripe magnetic domains appear with different contrast. The magnetization direction of each domain towards their magnetic easy axis.

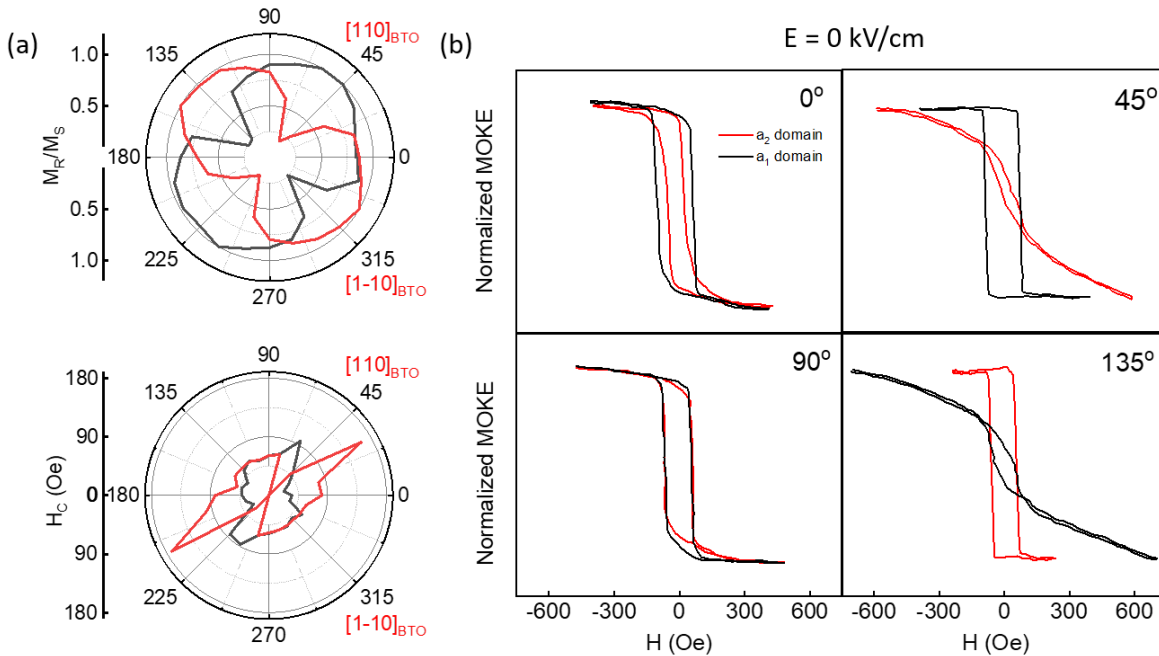


Figure 7.3. Experimental polar plots of (a) the squareness ratio (M_R/M_S) (above) and the magnetic switching fields (H_C) (bottom) of the Fe film grown on the BTO a_1 and a_2 domains. The $[100]$ directions of the a_1 and a_2 domains of BTO substrate are denoted. (b) Magnetic hysteresis loops of Fe on single a_1 and a_2 domains measured at different magnetic field angles under zero electric field. The direction of magnetic field was modulated by sample rotation in the Kerr microscopy while electromagnet was fixed. The widths of the a_1 domain and a_2 domain are 5.13 and 15.1 μm , respectively. The α is angle between the applied magnetic field and the stripe domain walls.

Thus, the magnetization is laterally modulated by near 90° rotation at the domain boundaries. The similar result is obtained in the reverse process (3 and 4). Here, the abrupt changes in local magnetic anisotropy are the evidence for pinning of the magnetic domain walls and the ferroelectric domain boundaries. As a results, during applying magnetic field, the overall stripe pattern does not alter unless the film is saturated and magnetic switching in a_1 and a_2 domain differs considerably

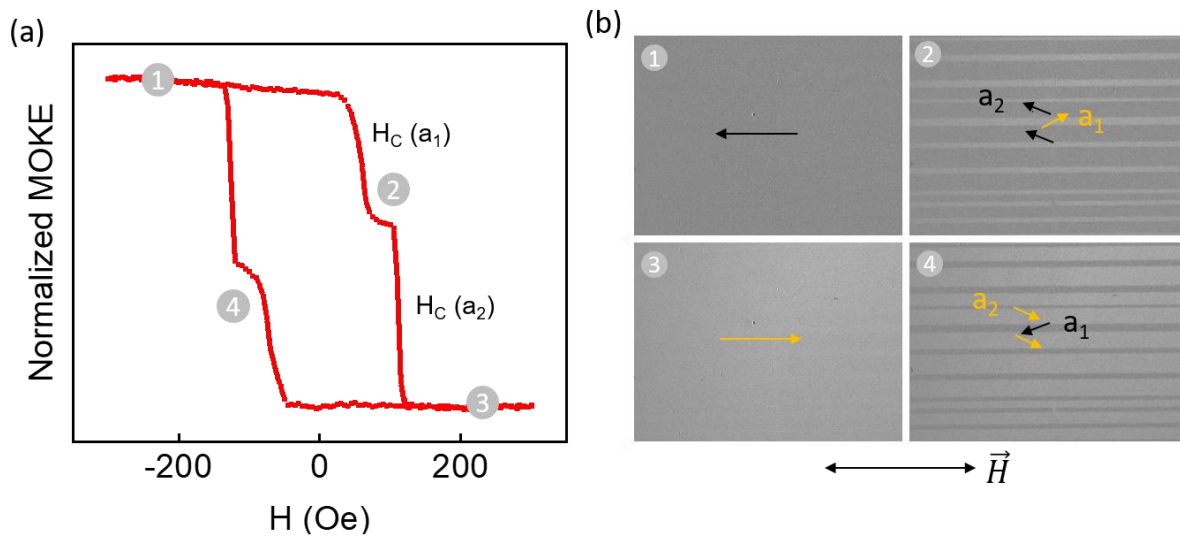


Figure 7.4. (a) In-plane magnetic hysteresis loop of multi a_1 - a_2 Fe domains with applied magnetic field parallel to stripe domain. (b) Kerr microscopy images of a 10 nm thick epitaxial Fe film on BTO under some selected applied magnetic fields for magnetic field direction parallel to stripe domains. The number of images following the field value in hysteresis loop of (a).

7.3.1.4 Electric field control of magnetic anisotropy of Fe film grown on the in-plane a_1 - a_2 BTO domains.

The possibility of controlling the magnetic anisotropy of Fe from uniaxial to biaxial magnetic anisotropy by applying the out-of-plane electric field is shown in Fig. 7.5. Figure 7.5a presents the schematic illustration of the observed BTO ferroelectric domain arrangement under applying an out-of-plane electric field (visualized for the Fig. 7.5b).

From the initial alternating a_1 - a_2 BTO domain at $E = 0$ kV/cm, the a_1 domains are disappeared and replaced by the a_2 domains with increasing the applied electric field to $E = 4$ kV/cm. The a_2 -c stripe domain appears when applying the further electric field and becomes to single c-domain at saturation state with $E = 6$ kV/cm. The c domain polarization direction is along with [001]-direction. Figure 7.5c shows the MOKE curves of Fe film under an in-plane applied magnetic field with $\alpha = 0^\circ$ at various applying electric field. Herein, the evolution BTO domain configuration obviously affects to Fe magnetization process. At $E = 0$ kV/cm, a kink MOKE hysteresis loop which is superposition of ferromagnetic hysteresis loops with different coercive fields in a_1 and a_2 domains is observed. This observation is caused by the different magnetic anisotropy of Fe film grown on a_1 - a_2 stripe domain as mentioned before (Fig. 7.3). The single loop is obtained at $E = 4$ kV/cm, where single a_2 BTO domain is presented. At $E = 5$ kV/cm, the c BTO domain with the polarization direction along with the applying electric field direction appears. The a_1 -c stripe domain of BTO induces the kink hysteresis loop of Fe film. At $E = 6$ kV/cm, the entire BTO domain become to the single out-of-plane c domain. The squareness loop of Fe film is obtained and the coercivity is much decreased to $H_C = 35$ Oe. That is attributed to the forming the new magnetic anisotropy on the single c BTO domain that will be demonstrated later in Fig. 7.7.

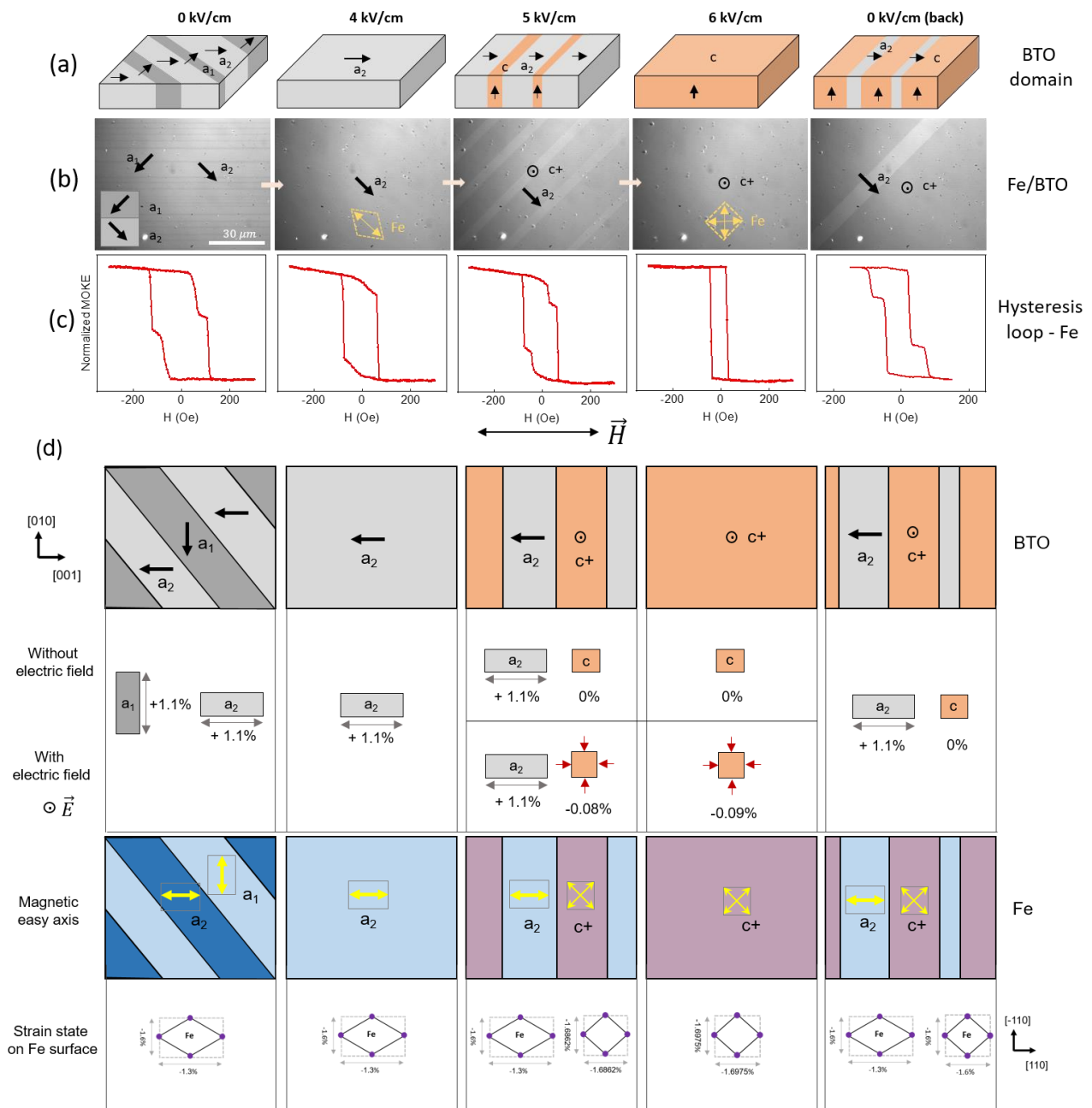


Figure 7.5. (a) Schematic illustration of the observed BTO ferroelectric domain arrangement under applying an out-of-plane electric field. (b) FE domain configuration of the BTO under applied E of 6 kV/cm along out-of-plane direction. (c) Normalized Kerr magnetic hysteresis loops of the Fe film. (d) The analysis of differential-strain transfer from BTO substrate to Fe film.

Figure 7.5d presents the analysis of differential-strain transfer from BTO substrate to Fe film. The differential strain model predicts the induced magnetic anisotropy and the direction of the magnetic easy axis by analyzing the accumulated strain in the Fe film due to changes in the strain state of BTO.

The differential strain in BTO domains can be expressed as ϵ^{BTO} which is difference between the strain along two orthogonal [010]BTO and [100]BTO axes. For instance, the strain differential in BTO for a₁, a₂, and c domains is +1.1%, -1.1%, and 0%. After growth, Fe under strain caused by lattice mismatch between Fe and BTO. However, when BTO domain changes in response to external stimuli (voltage, in this case), the Fe film on top experiences the induced strain from BTO domain switching and piezoelectric effect. Therefore, the total strain on film is: $\epsilon^{Fe} = \epsilon_{gr}^{BTO} + \epsilon_V^{BTO}$. The total differential strain in the Fe film determine the modulation in the imprinted magnetic domain pattern of the film, as the magnetoelastic anisotropy K_σ is given by:

$$K_\sigma \propto \lambda_S(\epsilon_{010}^{Fe} - \epsilon_{100}^{Fe}) \propto \lambda_S \epsilon^{Fe}$$

where λ_S is the magnetostriction coefficient. Therefore a strain change in BTO can induce a strain transfer in the Fe film altering the magnetoelastic anisotropy. The magnetic anisotropy axis or the magnetic anisotropy in the Fe film is thus determined by the sign of the accumulated differential strain. Because the magnetostriction of Fe is positive, $\epsilon^{Fe} > 0$ and $\epsilon^{Fe} < 0$ orient the magnetic easy axis along [010]Fe and [100]Fe, respectively. For full strain transfer from BTO to Fe film, uniaxial magnetic anisotropy is formed on film grown on BTO a-domain, biaxial magnetic anisotropy is formed on that grown on BTO c-domains.

| Electric field | BTO | Lattice mismatch strain | BTO surfaces | Easy axis (Fe) | Strain caused by E (easy axis) | K_{me} (J/m ³) |
|----------------|-----|-------------------------|--------------|----------------|--------------------------------|------------------------------|
| 0 kV/cm | | a domain | | | - 0.5617% | 2.654×10^4 |
| 4 kV/cm | | | | | - 0.55% | 2.595×10^4 |
| 5 kV/cm | | c domain | | | - 0.54% | 2.5515×10^4 |
| 6 kV/cm | | | | | - 1.6862% | 7.97×10^4 |
| 6 kV/cm | | | | | - 1.6975% | 8.02×10^4 |

Figure 7.6. The interpretation of the strain state that the BTO domains at their interface cause in the Fe film while the walls of the a_1 - a_2 domain move to form a single a domain and switch from a domain to a c domain.

Figure 7.6 illustrates the interpretation of the strain state induced on the Fe film by the BTO domains at their interface. Starting from the initial state with an alternating a_1 - a_2 domain configuration, when a small electric field is applied, the a_1 - a_2 domains undergo domain wall movement. Additionally, as explained in Chapter 2, an out-of-plane electric field causes shear strain in the in-plane domains of ferroelectric materials. Therefore, during the domain wall movement and before the switching step of the in-plane a domain, the magnetic domain

experiences strain induced by the shearing from the substrate. This strain causes a slight rotation in the magnetic easy axis of the film in each domain. This change is clearly shown in Figure 7.7.

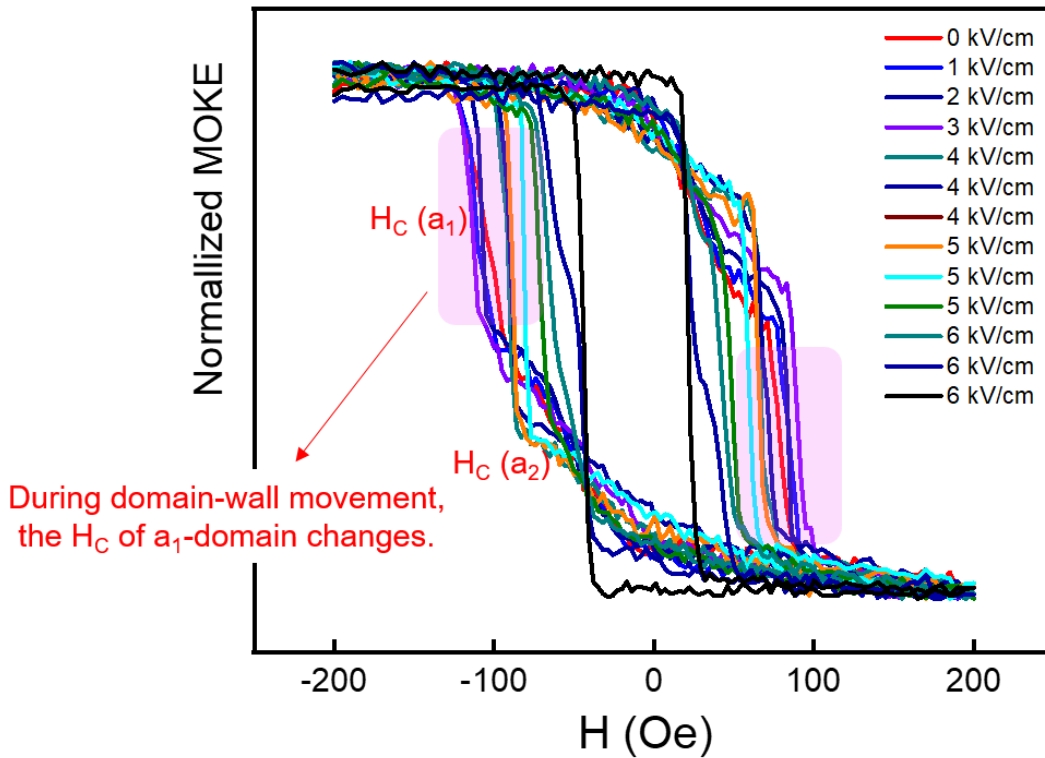


Figure 7.7. Hysteresis loop of combination of a₁-a₂ domain of Fe film under various applied electric field values.

We also can calculate the strain value on each domain on each applied electric field value. The magnetoelastic anisotropy energy is calculated by the formula: $K_{me} = 3/2\sigma\lambda$, where σ is applied stress and λ is magnetostriction coefficient (1.5×10^{-5}). We have $\sigma = strain, \epsilon \times Young's\ modulus$. The Young's modulus of Fe is $2.1 \times 10^{11} (J/m^3)$.

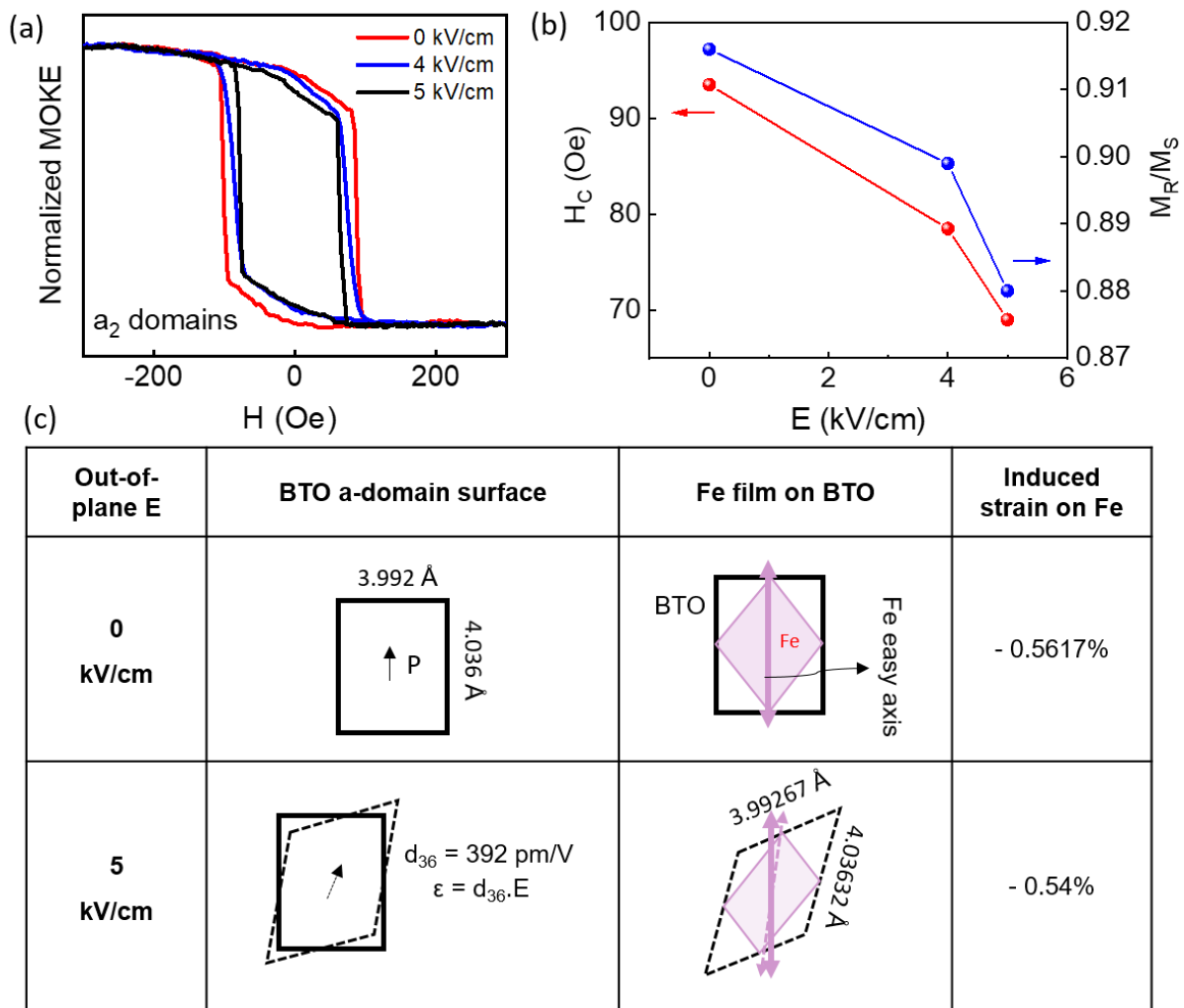


Figure 7.8. (a) The hysteresis loops of the Fe film during application of the out-of-plane electric field, which ranges from zero to $E = +4$ kV/cm, and reaches to $E = +6$ kV/cm. (b) The dependence of the remnant magnetization and the coercivity value to the applied electric field values. (c) Relation between the shearing strain on the BTO surface to the magnetic anisotropy of the Fe film.

The polar plot of the remnant magnetization and the coercivity field in Fig. 7.9a clearly illustrates that the magnetic anisotropy of the c domains exhibits fourfold symmetry. Thus, the Fe film on the single c BTO domain at $E = 6$ kV/cm exhibit the biaxial magnetic anisotropy. Here, the easy axis magnetization axes are aligned along [100]-Fe and [010]-Fe, that is in agreement with the magnetocrystalline anisotropy of bulk Fe. This magnetic anisotropy behavior in the c domains of the Fe film is striking different compared to that on the a domains. To interpret the observation, we need to consider to strained-mediated relationship between local magnetic anisotropy and the underlying ferroelectric domain structure. With applying an external electric field of $E = 6$ kV/cm, the field direction aligned along the direction of spontaneous polarization, the lattice along the c axis (out-of-plane) alongates, while that of the a axis (in-plane) shrinks. To understand the strain induced from the in-plane BTO into the Fe film at the interface, we focus on the in-plane lattice constant altered by the electric field of the BTO. The a axis lattice constant is calculated from the formula [29]:

$$(a - a_0)/a_0 = d_{31} \cdot E \quad (7.2)$$

Where, a_0 and a present the lattice constant in the in-plane film for $E = 0$, and $E \neq 0$, d_{31} is the piezoelectric coefficients of the in-plane lattice at room temperature when applying an external field along to out-of-plane. With $a_0 = 3.993 \text{ \AA}$ and $d_{31} = -82 \text{ pmV}^{-1}$, thus the BTO lattice constant at $E = 6$ kV/cm is $a_{BTO} = 3.99320 \text{ \AA}$. This BTO lattice constant induces a biaxial compressive strain of -1.616% along the cubic axes of Fe film ($a_{Fe} = 2.870 \text{ \AA}$). From the first term in Eq. 1, with $e_{xy} = -1.616\%$, $\alpha_x = 1$, $\alpha_y = 0$, and $B_1 = -3.43 \times 10^6 \text{ J/m}^3$, the magnetoelastic anisotropy along [100]-Fe can be estimated, the result is $K_{me} = -5.5 \times 10^4 \text{ J/m}^3$. The same result is obtained for [010]-Fe with $\alpha_x = 0$, $\alpha_y = 1$. The biaxial compressive strain along [100]-Fe

and [010]-Fe lowers the magnetoelastic anisotropy energy along these directions. This interpretation agrees with the experimentally observed orientation of the easy axis magnetization axes in the c domains. The observation is caused by the strain transfer at Fe film and BTO domain interface. Clearly, the ferroelastic in-plane a_1 (or a_2) and out-of-plane c domains of BTO impose the different local strains on the epitaxial films.

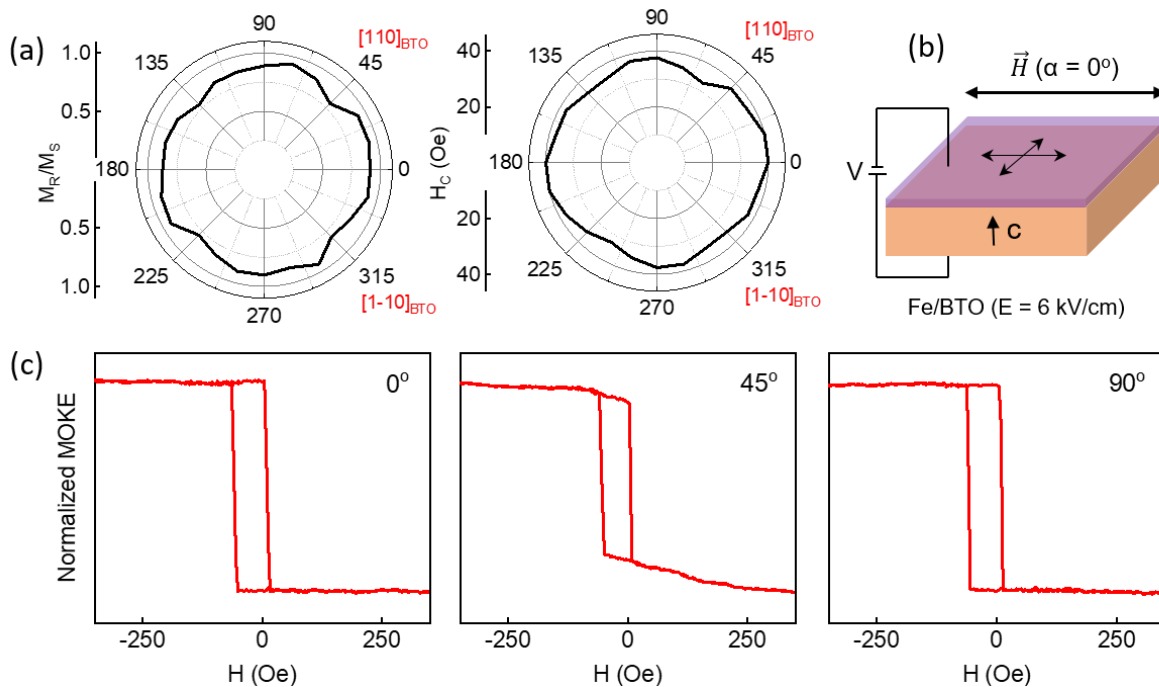


Figure 7.9. (a) Experimental polar plots of squareness ratio of the Fe film at the out-of-plane E of $E = + 6$ kV/cm. (b) The schematic illustration of the domain configuration in the Fe/BTO (right-hand side) at RT at the applied E of 6 kV/cm. The angles between the applied magnetic field (H) and the domain wall is represented by α . The magnetic anisotropies axes of Fe film are depicted with double-headed arrows, the arrows in the bottom schematic indicate the BTO polarization direction. (c) In-plane magnetic hysteresis loop of multiple c - a_2 Fe domains with applied H at different angles during application of $E = 6$ kV/cm.

7.3.1.5 Appearing the a-c stripe domain as remanant state after removing an electric field from the saturation state; Magnetic anisotropy of Fe film on a-c BTO domains

For full strain transfer from the a BTO domain to the Fe film, the in-plane lattice of the Fe films is compressed by -1.6% and -0.6% in the [110]Fe and [-110]Fe directions with respect to that of the bcc Fe bulk structure ($a_{\text{Fe}} = 2.870 \text{ \AA}$), this is caused by the diamond shape on top of the a domains. In contrast, on top of the ferroelastic c domains, the in-plane Fe lattice remains in the cubic shape with the compressed strain of -1.6% in both of the [110]Fe and [-110]Fe directions. After removing the applying out-of-plane electric field from the saturation state, the new a_1 -c stripe domains appear as shown in the ferroelectric domain structure and its schematic illustration is shown in Fig. 7.10a. The new magnetic anisotropy of Fe film is determined on the experimental polar plot of M_R/M_S and H_C (Fig. 7.10b). The twofold symmetry magnetic anisotropy is still observed in the a_1 domain that consists to the results in Fig. 7.3. The M_R/M_S polar plot of the Fe film conducted on the BTO single c domain exhibits the fourfold symmetry, indicating that the in-plane biaxial magnetic anisotropy of Fe film is observed.

The modulation of magnetic easy axis in the out-of-plane c-domain compared to the in-plane a-domain is attributed to the degree of strain transfer at the Fe/BTO interface. This biaxial magnetic anisotropy of Fe on the single c domain has also been reported by Tuomas H. E. Lahtinen et.al.[39]

Figure 7.10c exhibits the a_1 -c stripe domain hysteresis loops measured at several local magnetization curves for the different field angles (α). Herein, the rotation of the ferroelectric polarization in the BTO substrate resulted in the formation of new magnetic anisotropy in Fe film.

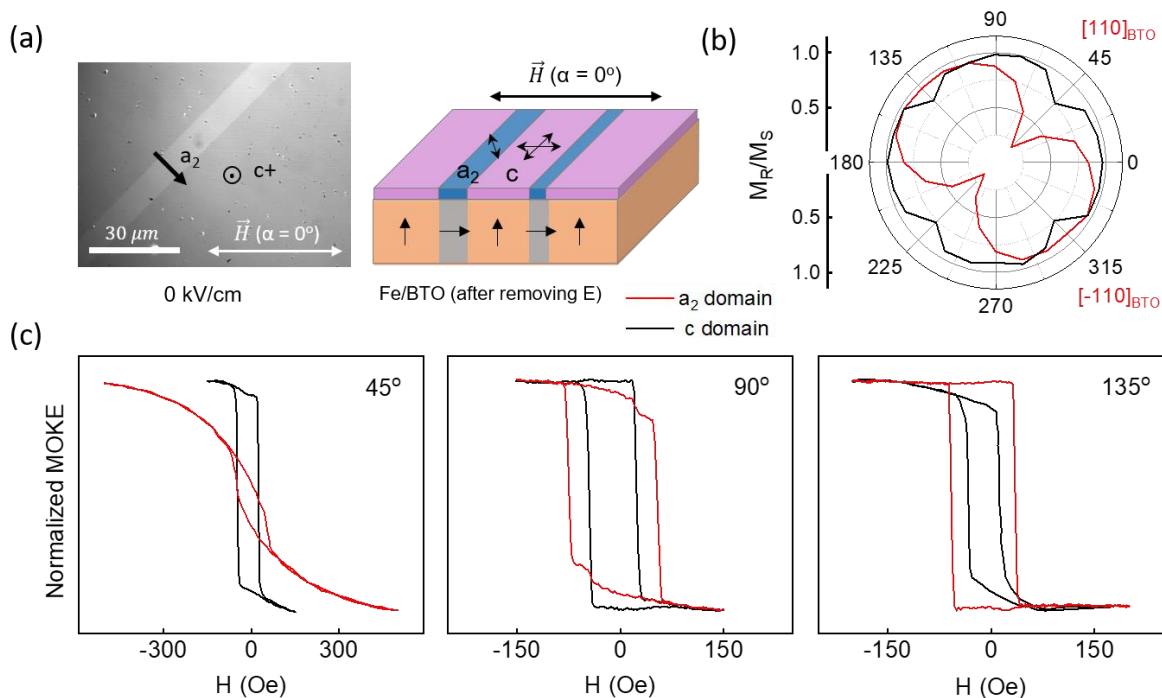


Figure 7.10. (a) FE domain configuration of the BTO substrate after removing electric field (b)

Experimental polar plots of squareness ratio of the Fe film after removing the out-of-plane electric field of $E = + 6$ kV/cm. (c) In-plane magnetic hysteresis loop of single c and a_2 domains of Fe film with applied magnetic field at different magnetic field angles under zero electric field.

The Fe film is on top of the in-plane a domain BTO present the uniaxial magnetic easy axis while that is on top of out-of-plane c domain BTO shows the the biaxial one. The relationship between the direction of the polarization and the magnetic anisotropy, which is mediated by strain transfer at the Fe/BTO interface, results in the Fe magnetic domains mimicking the BTO ferroelectric domains during the evolution process under an applied electric field.

7.4 Conclusion

In summary, we have achieved full ferroelectric-to-ferromagnetic pattern transfer and electric-field-induced magnetic anisotropy changes in Fe/BTO heterostructure. The in-plane alternating BTO domain induces the uniaxial magnetic anisotropy in the Fe film, while the biaxial magnetic anisotropy is exhibited in the single out-of-plane BTO domain. Notably, the magnetic anisotropy can be modified by ferroelectric polarization direction. This underlying mechanism is based on strain-mediated coupling between the ferroelectric substrate and ferromagnetic film. Our results provide valuable insights understanding the strain-driven magnetic anisotropy of FM/FE heterostructures, which can be applied to the design of electric-field controlled magnetic devices.

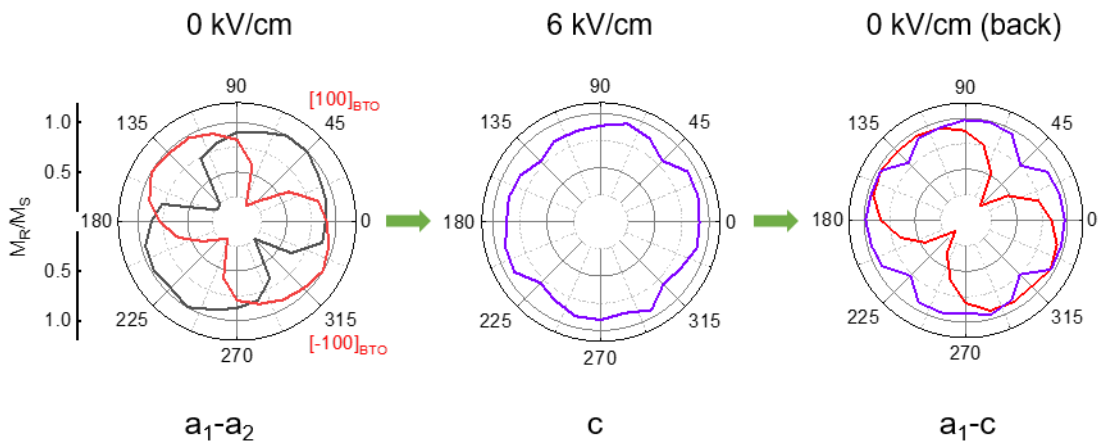


Figure 7.11. Electric field control of magnetic anisotropy of Fe/BTO.

7.5 References

- [1] K. Eshraghian, “Evolution of Nonvolatile Resistive Switching Memory Technologies: The Related Influence on Hetrogeneous Nanoarchitectures,” *Trans. Electr. Electron. Mater.*, vol. 11, no. 6, pp. 243–248, 2010.
- [2] R. Ramesh and L. W. Martin, “Electric field control of magnetism: multiferroics and magnetoelectrics,” *Riv. del Nuovo Cim.*, vol. 44, no. 5, pp. 251–289, 2021.
- [3] R. Ramesh and N. A. Spaldin, “Multiferroics: Progress and prospects in thin films,” *Nanosci. Technol. A Collect. Rev. from Nat. Journals*, vol. 3, pp. 20–28, 2009.
- [4] S. M. Yakout, “Spintronics: Future Technology for New Data Storage and Communication Devices,” *J. Supercond. Nov. Magn.*, vol. 33, no. 9, pp. 2557–2580, 2020.
- [5] J. Ma, J. Hu, Z. Li, and C. W. Nan, “Recent progress in multiferroic magnetoelectric composites: From bulk to thin films,” *Adv. Mater.*, vol. 23, no. 9, pp. 1062–1087, 2011.
- [6] C. Lu, M. Wu, L. Lin, and J. M. Liu, “Single-phase multiferroics: New materials, phenomena, and physics,” *Natl. Sci. Rev.*, vol. 6, no. 4, pp. 653–668, 2019.
- [7] J. J. Wang, F. Y. Meng, X. Q. Ma, M. X. Xu, and L. Q. Chen, “Lattice, elastic, polarization, and electrostrictive properties of BaTiO₃ from first-principles,” *J. Appl. Phys.*, vol. 108, no. 3, 2010.
- [8] T. Mion, D. M. Potrepka, F. J. Crowne, A. Tauber, and S. C. Tidrow, “Dielectric and X-ray diffraction analysis of Ba(Ga,Ta) 0.05Ti 0.90O 3,” *Ferroelectrics*, vol. 473, no. 1, pp. 13–23, 2014.
- [9] “Thermal expansion coefficient of Fe with temperature” .

- [10] S. Brivio, C. Rinaldi, D. Petti, R. Bertacco, and F. Sanchez, “Epitaxial growth of Fe/BaTiO₃ heterostructures,” *Thin Solid Films*, vol. 519, no. 17, pp. 5804–5807, 2011.
- [11] T. Mikolajick *et al.*, “Next generation ferroelectric materials for semiconductor process integration and their applications,” *J. Appl. Phys.*, vol. 129, no. 10, 2021.
- [12] J. F. Scott, “Applications of modern ferroelectrics,” *Science (80-.)*, vol. 315, no. 5814, pp. 954–959, 2007.
- [13] T. Y. Kim, S. K. Kim, and S. W. Kim, “Application of ferroelectric materials for improving output power of energy harvesters,” *Nano Converg.*, vol. 5, no. 1, pp. 1–16, 2018.
- [14] L. W. Martin and A. M. Rappe, “Thin-film ferroelectric materials and their applications,” *Nat. Rev. Mater.*, vol. 2, no. 2, 2016.
- [15] S. Zhang, B. Malič, J. F. Li, and J. Rödel, “Lead-free ferroelectric materials: Prospective applications,” *J. Mater. Res.*, vol. 36, no. 5, pp. 985–995, 2021.
- [16] S. Wada, K. Yako, K. Yokoo, H. Kakemoto, and T. Tsurumi, “Domain wall engineering in barium titanate single crystals for enhanced piezoelectric properties,” *Ferroelectrics*, vol. 334, no. 1 PART 2, pp. 17–27, 2006.
- [17] L. S. R. Rocha *et al.*, “A study approach on ferroelectric domains in BaTiO₃,” *Mater. Charact.*, vol. 120, pp. 257–262, 2016.
- [18] T. H. E. Lahtinen, K. J. A. Franke, and S. Van Dijken, “Electric-field control of magnetic domain wall motion and local magnetization reversal,” *Sci. Rep.*, vol. 2, pp. 1–6, 2012.

- [19] F. Rubio-Marcos, A. Del Campo, P. Marchet, and J. F. Fernández, “Ferroelectric domain wall motion induced by polarized light,” *Nat. Commun.*, vol. 6, 2015.
- [20] Z. K. Zhang, D. N. Fang, and A. K. Soh, “A new criterion for domain-switching in ferroelectric materials,” *Mech. Mater.*, vol. 38, no. 1–2, pp. 25–32, 2006.
- [21] V. Boddu, F. Endres, and P. Steinmann, “Molecular dynamics study of ferroelectric domain nucleation and domain switching dynamics,” *Sci. Rep.*, vol. 7, no. 1, pp. 1–10, 2017.
- [22] M. G. Shaikh, S. Phanish, and S. M. Sivakumar, “Domain switching criteria for ferroelectrics,” *Comput. Mater. Sci.*, vol. 37, no. 1–2, pp. 178–186, 2006.
- [23] X. Chao, J. Wang, J. Pu, S. Zhang, and Z. Yang, “Aging behavior and electrical properties of low-temperature sintered (Ba, Ca)(Ti, Zr)O₃-Ba(Cu, W)O₃ ceramics and plate loudspeaker,” *Sensors Actuators, A Phys.*, vol. 237, pp. 9–19, 2016.
- [24] M. Yuan *et al.*, “Biocompatible nanogenerators through high piezoelectric coefficient 0.5Ba(Zr_{0.2}Ti_{0.8})O₃-0.5(Ba_{0.7}Ca_{0.3})TiO₃ nanowires for in-vivo applications,” *Adv. Mater.*, vol. 26, no. 44, pp. 7432–7437, 2014.
- [25] N. R. Alluri, B. Saravanakumar, and S. J. Kim, “Flexible, hybrid piezoelectric film (BaTi(1-x)ZrxO₃)/PVDF nanogenerator as a self-powered fluid velocity sensor,” *ACS Appl. Mater. Interfaces*, vol. 7, no. 18, pp. 9831–9840, 2015.
- [26] X. Yan *et al.*, “Correspondence: Lead-free intravascular ultrasound transducer using BZT-50BCT ceramics,” *IEEE Trans. Ultrason. Ferroelectr. Freq. Control*, vol. 60, no. 6, pp. 1272–1276, 2013.

- [27] M. Goiriena-Goikoetxea *et al.*, “Influence of dislocations and twin walls in BaTiO₃ on the voltage-controlled switching of perpendicular magnetization,” *Phys. Rev. Mater.*, vol. 5, no. 2, 2021.
- [28] M. He, M. Wang, and Z. Zhang, “Electric-field-induced domain intersection in BaTiO₃ single crystal,” *Jpn. J. Appl. Phys.*, vol. 56, no. 3, 2017.
- [29] M. Acosta *et al.*, “BaTiO₃-based piezoelectrics: Fundamentals, current status, and perspectives,” *Appl. Phys. Rev.*, vol. 4, no. 4, 2017.
- [30] L. B. and G. J. S. Bo-Kuai Lai, Inna Ponomareva, Igor A. Kornev, “Domain evolution of BaTiO₃ ultrathin films under electric field: a first-principles study Bo-Kuai Lai, Inna Ponomareva, Igor A. Kornev, L. Bellaiche and G. J. Salamo Physics Department, University of Arkansas, Fayetteville, Arkansas 72701.”
- [31] K. J. A. Franke, T. H. E. Lahtinen, A. Casiraghi, D. L. González, S. J. Hämäläinen, and S. van Dijken, “Electric field control of magnetism based on elastically coupled ferromagnetic and ferroelectric domains,” *Nanoscale Ferroelectr. Multiferroics Key Process. Charact. Issues, Nanoscale Eff. 2 Vol.*, pp. 678–699, 2016.
- [32] P. R. Potnis, N. T. Tsou, and J. E. Huber, “A review of domain modelling and domain imaging techniques in ferroelectric crystals,” *Materials (Basel)*, vol. 4, no. 2, pp. 417–447, 2010.
- [33] J. E. Rault, T. O. Menteş, A. Locatelli, and N. Barrett, “Reversible switching of in-plane polarized ferroelectric domains in BaTiO₃ (001) with very low energy electrons,” *Sci. Rep.*, vol. 4, pp. 1–7, 2014.

- [34] C. M. Landis, “Non-linear constitutive modeling of ferroelectrics,” *Curr. Opin. Solid State Mater. Sci.*, vol. 8, no. 1, pp. 59–69, 2004.
- [35] D. Damjanovic, “Contributions to the piezoelectric effect in ferroelectric single crystals and ceramics,” *J. Am. Ceram. Soc.*, vol. 88, no. 10, pp. 2663–2676, 2005.
- [36] B. Jiang, Y. Bai, W. Chu, Y. Su, and L. Qiao, “Direct observation of two 90° steps of 180° domain switching in BaTiO₃ single crystal under an antiparallel electric field,” *Appl. Phys. Lett.*, vol. 93, no. 15, pp. 1–4, 2008.
- [37] K. J. A. Franke, D. López González, S. J. Hämmäläinen, and S. Van Dijken, “Size dependence of domain pattern transfer in multiferroic heterostructures,” *Phys. Rev. Lett.*, vol. 112, no. 1, pp. 1–5, 2014.
- [38] Y. W. Li, J. F. Scott, D. N. Fang, and F. X. Li, “90-degree polarization switching in BaTiO₃ crystals without domain wall motion,” *Appl. Phys. Lett.*, vol. 103, no. 23, 2013.
- [39] T. H. E. Lahtinen *et al.*, “Alternating domains with uniaxial and biaxial magnetic anisotropy in epitaxial Fe films on BaTiO₃,” *Appl. Phys. Lett.*, vol. 101, no. 26, pp. 1–5, 2012.
- [40] K. J. A. Franke, B. Van de Wiele, Y. Shirahata, S. J. Hämmäläinen, T. Taniyama, and S. van Dijken, “Reversible electric-field-driven magnetic domain-wall motion,” *Phys. Rev. X*, vol. 5, no. 1, pp. 1–9, 2015.
- [28] Magnetoelastic anisotropy, D. Sander, *Rep. Prog. Phys.* 62, 809 (1999).
- [29] Lattice distortion under an electric field in BaTiO₃ piezoelectric single crystal, 2009 *J. Phys.: Condens. Matter* 21 215903

CHAPTER 8: REVERSIBLE ELECTRIC-FIELD-DRIVEN MAGNETIC ANISOTROPY OF FE/BTO HETEROSTRUCTURES

The reversible control of the magnetic anisotropy in an epitaxial Fe film, grown on the stripe a-c domain of BTO, through the application of an electric field is demonstrated in this chapter. In this configuration, the polarization of the in-plane a domain of BTO is aligned along the [100] direction, while that of the out-of-plane c domains is aligned along the [001] direction. Consequently, the film exhibits uniaxial magnetic anisotropy on the a domain of BTO and biaxial magnetic anisotropy on the c domain of BTO. This observation is attributed to complete strain transfer from the substrate to the film via magnetoelectric coupling at the interface. Specifically, when an external electric field is applied within the range of -11 kV/cm to 11 kV/cm, the magnetic anisotropy of the film is alternately modulated between biaxial and uniaxial magnetic anisotropy. This reversal occurs as the applied field direction changes. This observation confirms the presence of a strong elastic coupling between magnetic and ferroelectric domain walls in Fe/BTO heterostructures. These results hold significant promise for future spintronic applications that utilize voltage-controlled magnetic states through such strain-coupling materials.

8.1 Introduction

As discussed in Chapter 5, BTO exhibits three primary domain configurations: head-to-tail c-a₁, c-a₂, and a₁-a₂ domains. These configurations minimize electrostatic energy at the domain walls. The out-of-plane c domains are polarized along the [001] direction, while the in-plane domains are labeled a₁ and a₂, with polarization along the [010] and [100] directions, respectively. Recent findings have revealed that in BTO single crystals, a 180-degree domain switching occurs through

a two-step 90-degree domain switching process when subjected to an antiparallel electric field. This domain configuration evolution is a significant source of strain on the surface, owing to the varying lattice mismatch between these domain types.

Furthermore, Fe/BTO is one of the most promising candidates for multiferroic research, as detailed in Chapters 6 and 7, primarily because their magnetic properties can be solely controlled by an electric field through interfacial magnetoelectric coupling [1-20]. For these reasons, our research investigates the effects of the electric field on the domain configuration of BTO and its impact on the magnetic anisotropy of the films. Interestingly, we have observed that the magnetic anisotropy can be reversibly controlled by an electric field within the range of -11 kV/cm to 11 kV/cm. The film's magnetic anisotropy alternates between biaxial (in the film on the c domain of BTO) and uniaxial (in the Fe film on the a domain of BTO) when the applied field direction changes. These findings confirm the presence of a strong elastic coupling between magnetic and ferroelectric domain walls in Fe/BTO heterostructures.

8.2 Experiment methods

The 10 nm thick Fe films were deposited onto single crystal BTO (001) substrates using molecular beam epitaxy (MBE – VG Semicon, Inc.). The base pressure of the growth chamber was $\sim 10^{-10}$ Torr. After pre-heating cleaned BTO at 600 °C for 30 minutes in ultra-high vacuum (UHV) to remove impurities, the substrate was cooled down to 300 °C for growth. The evaporation rate of Fe atomic is 0.1 Å/s determined by using a quartz crystal thickness monitor. The quality of the substrate and the film was monitored by *in-situ* reflection high energy electron diffraction (RHEED). After growth, the film was covered by a 2 nm thick Sb capping layer to prevent oxidation under atmospheric conditions. The crystal structure of the samples was characterized by

X-ray diffraction (XRD). The ferroelectric BTO domains were imaged using birefringence contrast with the polarizer and analyzer in cross-configuration. The magnetic domain patterns and hysteresis loops were measured using the magneto-optical Kerr effect (MOKE). The background subtraction method was used to zero-out contrast from structural defect and ferroelectric domain during observation the MOKE signal of Fe film. Electric fields were generated by using the Fe film as top electrode and silver paint on the back of the BTO substrates as bottom electrode.

8.3 Results and discussions

8.3.1 Magnetic anisotropy of Fe film on a-c BTO domains

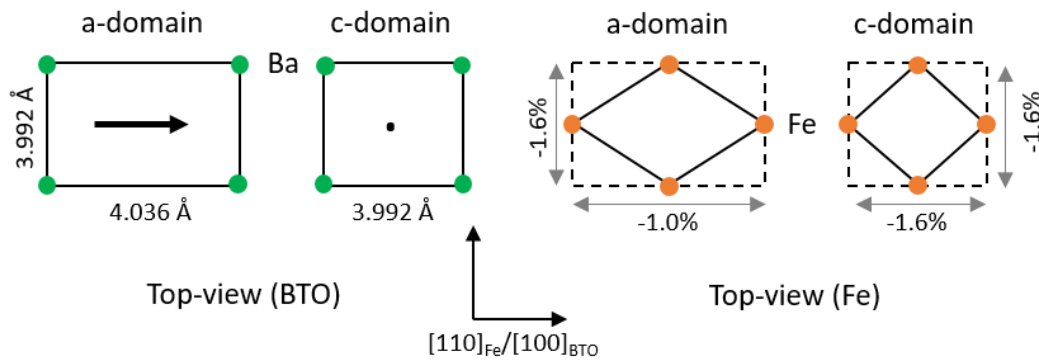


Figure 8.1. The schematic illustration of the in-plane lattice structure and ferroelectric polarization direction of the BTO substrate and the orientation of the Fe film on the a and c BTO domains. For full strain transfer from BTO substrate into the Fe film, the calculated lattice mismatch strain is estimated. The arrow and dot note in BTO unit cell depicts the ferroelectric polarization direction.

The observed compressive strain of Fe film on BTO is visualized by the schematic illustration in Fig. 8.1 with epitaxial relationship of $[110]_{\text{Fe}}/[100]_{\text{BTO}}$. Here, owing to the full strain transfer from the BTO lattice to the Fe film during growth, the in-plane Fe lattice on top of the ferroelastic a domains has the diamond shape with the shear strain along $[110]_{\text{Fe}}$ of -1.6% and the shear along $[-110]_{\text{Fe}}$ of -0.6% , whereas the Fe film on top of c domains is cubic shape with compressive strain of -1.6% and this is equal to $[110]_{\text{Fe}}$ and $[-110]_{\text{Fe}}$. The lattice mismatch strain is estimated using the lattice bcc Fe bulk structure ($a_{\text{Fe}} = 2.870 \text{ \AA}$) and the tetragonal phase of the lattice BTO ($c = 3.992 \text{ \AA}$, $a = 4.036 \text{ \AA}$).[21-25]

In order to determine the magnetic anisotropy of Fe film grown on a-c stripe domain of BTO, the in-plane magnetic hysteresis loops were measured for different orientations of applied magnetic field. Figure 8.2a represents the polar plots of $M_{\text{R}}/M_{\text{S}}$ and H_{C} as function of magnetic field orientation. The Fe film grown on the c-domain exhibits the biaxial magnetic anisotropy with the net magnetic easy axis along $[110]_{\text{BTO}}$ and $[-110]_{\text{BTO}}$. While Fe film grown on the a-domain exhibits the uniaxial magnetic anisotropy with magnetic easy axis along $[100]_{\text{BTO}}$. To explain this observation, we use the in-plane lattice of BTO and Fe film (Fig. 8.1), as mentioned before, the unit cell of a domains in the (001)-oriented BTO surface is rectangular with a tetragonality of 1.1% , and the in-plane lattice of c domains is cubic. As a result, the Fe film formed on a-domains has a diamond shape unit cell with the maximum magnetoelastic anisotropy energy along $[110]_{\text{Fe}}$ direction ($K_{\text{me}} = 3.9 \times 10^4 \text{ J/m}^3$).[40] Because of the negative magnetostriction constant of Fe, the uniaxial magnetic easy axis is oriented along the orthogonal $[-110]_{\text{Fe}}$ direction (parallel to BTO domain wall). On the other hand, the unit cell of the Fe film formed on the c-domains exhibits a square shape, resulting in the biaxial compressive strain along $[100]_{\text{Fe}}$ and $[010]_{\text{Fe}}$, the magnetoelastic anisotropy energy of these direction is lower than that of other directions (K_{me}

$([100]_{\text{Fe}}) = K_{\text{me}} ([010]_{\text{Fe}}) = -5.5 \times 10^4 \text{ J/m}^3$.[26] Thus, the biaxial magnetic easy axis of Fe film on the c-domain orients to $[100]_{\text{Fe}}$ and $[010]_{\text{Fe}}$.

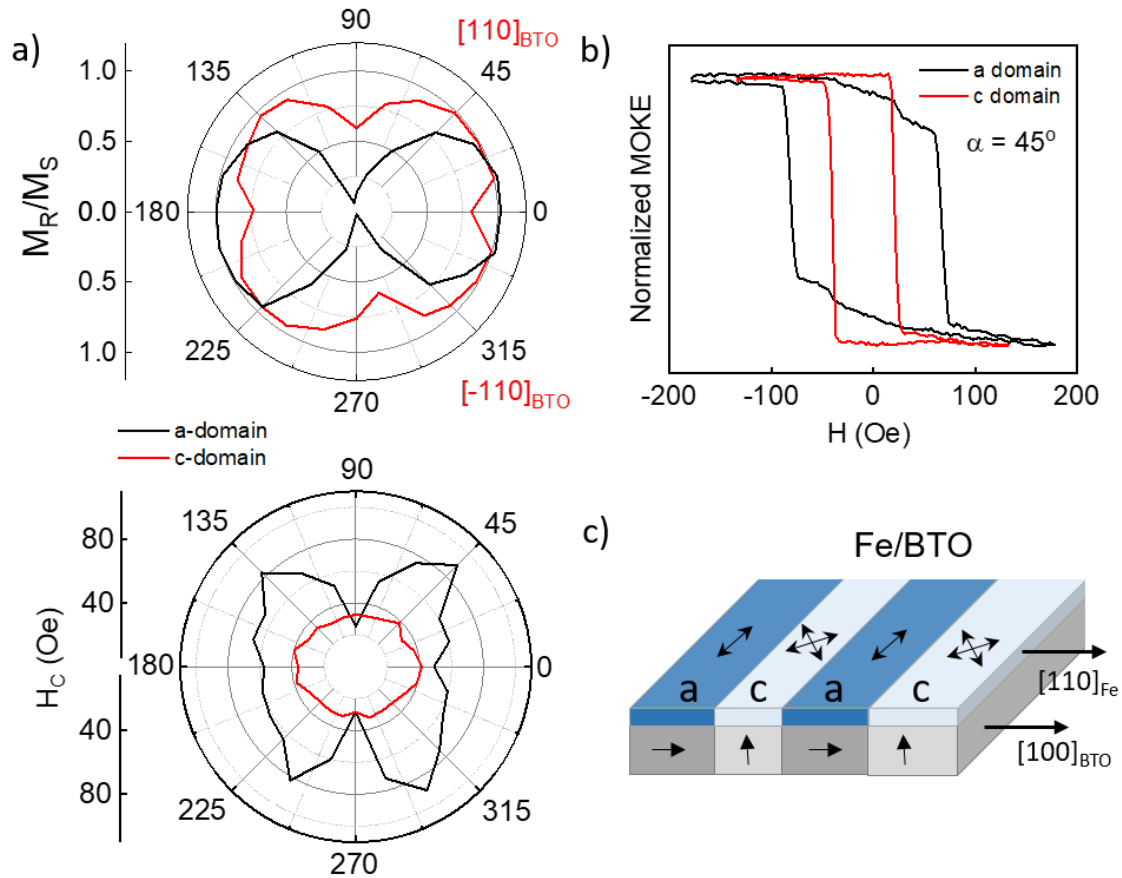


Figure 8.2. (a) Experimental polar plots of squareness ratio (M_R/M_S) and the magnetic switching fields (H_C) of the Fe film on a and c domains. (b) Magnetic hysteresis loop of single a (black curve) and single c (red line) domain measured at $\alpha = 45^\circ$. (c) Schematic illustration of ferromagnetic domain configuration of Fe/BTO film. The arrows indicate the direction of ferroelectric polarization, and the double-headed arrows represent the magnetic easy axes.

Figure 8.2b shows the magnetic hysteresis loops of single a (black loop) and single c (red loop) domain measured at $\alpha = 45^\circ$ with α is angle between magnetic field and BTO domain-wall. As a result, the square hysteresis loop on Fe film on c domains and the moderate remanence magnetization value on hysteresis loop Fe film on a domains is detected. This observation can be explained by the magnetic field is aligned along the magnetic easy axis of the c domains while it is aligned along the between easy and hard axis of a domains. To visualize the ferroelastic domain configuration of BTO and the magnetic anisotropy of Fe/BTO film, we provide the schematic illustration shown on Fig. 8.2c. Here, the domain configuration of cleaned BTO (underlying layer) is depicted with a-domain having in-plane ferroelectric polarization (the horizontal arrows) and c-domain having out-of-plane ferroelectric polarization (the vertical arrows). After film growing, the domain configuration of the epitaxial Fe film (top layer) is fully imprinted from the ferroelastic BTO domains which is explained by strain transfer at the multiferroic heterostructure interface. This leads to the uniaxial magnetic anisotropy (double-head arrows) of Fe film formed on a-domain, while Fe films formed on c-domain have biaxial magnetic anisotropy (two double-head arrows).

8.3.2.2 The pinning strength between ferroic domains

The magnetic anisotropy of Fe film on the a and c BTO domain is mentioned in Fig. 8.3 above. The uniaxial magnetic anisotropy is observed when Fe film on the a BTO domain, while that is grown on the c BTO domain shows the biaxial magnetic anisotropy. To ensure that the ferroelectric BTO domain and the magnetic Fe film domain is simultaneously driven by electric field in this case, we attempt to measure the magnetic hysteresis curves of sample during the magnetic domain wall motion (Fig. 8.3).

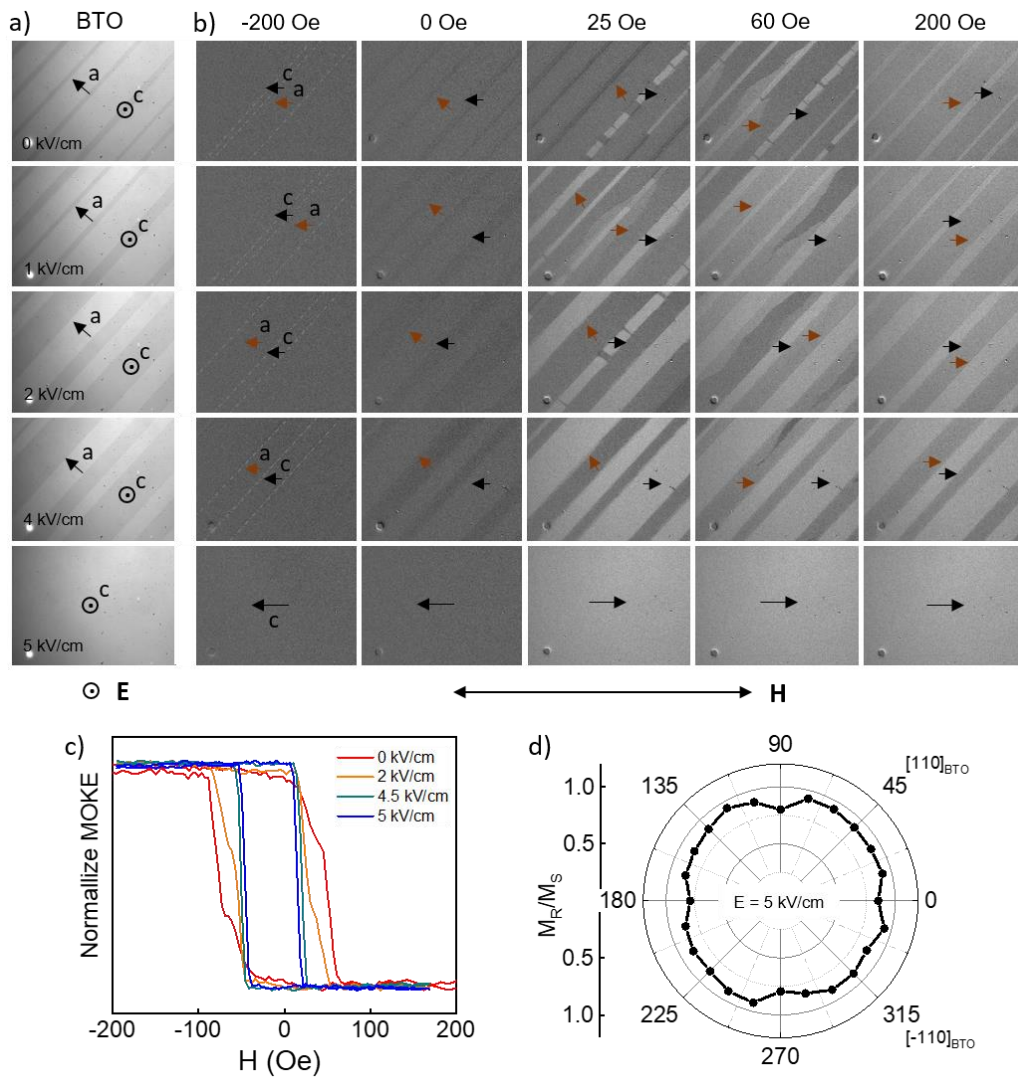


Figure 8.3. (a) Polarization microscopy images of the ferroelectric (BTO) during the application of an out-of-plane electric field. (b) The Kerr microscopy images of epitaxial Fe film on BTO for different applying electric field (corresponding to BTO domain configuration shown on (a)). (c) Magnetic hysteresis curves of a-c stripe domains measured at different electric field level. (d) Experimental polar plots of a squareness ratio of the Fe film under applied out-of-plane electric field of $E = 5$ kV/cm.

The electric field is changed in ascending, the double-hysteresis loop ($E = 0$ kV/cm with alternative a-c stripe domains of BTO) become come to single-hysteresis loop ($E = 5$ kV/cm with single c-domain of BTO). The hysteresis behavior under applying electric field is believed to be associated with the alternation of magnetic anisotropy from combination of uniaxial (a-domain) and biaxial (c-domain) magnetic anisotropy to single biaxial magnetic anisotropy (single c-domain) at ferroelectric saturation state. To insist that the electric field effects on magnetic anisotropy mechanism discussed in this paper does not alter the magnitude of magnetic anisotropy, we determine the polar plot of squareness ratio of Fe film at ferroelectric saturation state. The magnetic anisotropy of Fe film on single c-domain at ferroelectric polarization saturation state is as shown on Fig. 8.3c. The M_R/M_S at room temperature shows clear fourfold symmetry, and the easy axes is maintained orienting to $[110]_{\text{BTO}}$ and $[-110]_{\text{BTO}}$ as comparing with polar plot shown early on Fig. 8.3c. In other words, the strength and symmetry of the magnetic anisotropy is sustained during applying electric field or it does not modulate the magnitude of magnetic anisotropy.

8.3.2.3 Electric field control of magnetic anisotropy of Fe film on top of the c BTO domains.

Figure 8.4 displays the microscopy images of Fe/BTO during application of an external electric field from 5 kV/cm to -5 kV/cm and the converser process. This observation taken by the polarized light microscopy at room temperature. The entire polarization evolution process model of BTO domains was clearly presented and explained in the previous chapter 6. The cubic surface of BTO at single c domain induces the bixial magnetic anisotropy on Fe film. The uniaxial magnetic anisotropy is observed when Fe on the a domain of BTO with rectangular surface. When electric field decreases from 5 kV/cm, magnetic hysteresis loop shape changes with coervivity increase. This is because the appearance of a domain. Single hysteresis loop with higher

coercivity and lower remanent value is observed at -2 kV/cm (single a domain of BTO). The single hysteresis loop become kink loop with applying field due to the appearance of c domains. Finally, at saturation state, the single c domain of BTO induces the single square hysteresis loop. The square loop is caused by the applied magnetic field parallel to the Fe easy axis on the c domain,

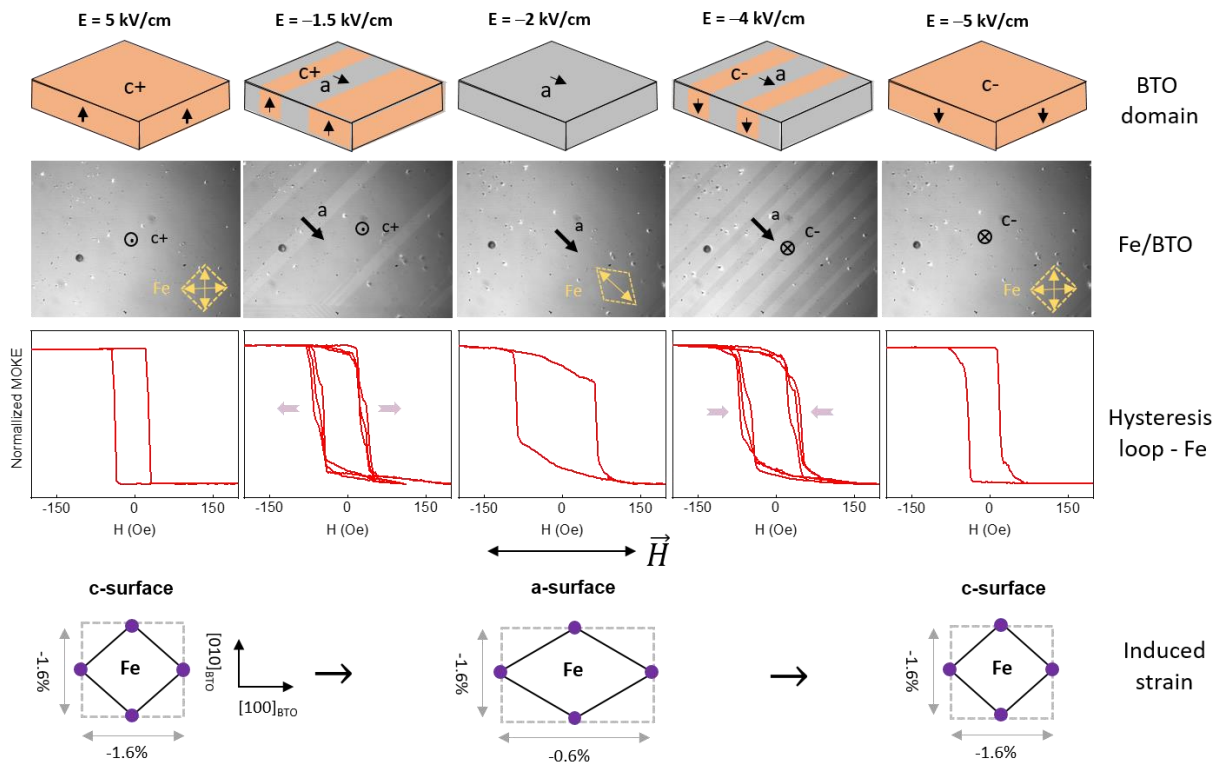


Figure 8.4. (a) The evolution of the single c domain under parallel and antiparallel out-of-plane electric field modulating from 0 to -5 kV/cm. The voltage rises at a rate of 1 V/min. The c+, c- with the dots and x marks denote the domain having the out-of-plane and anti-parallel-out-of-plane polarization direction pointing out and in the paper plane, respectively. The a_2 represents the in-plane domain having the polarization directions shown by the arrows. (b) Schematic illustration of the ferroelectric domain configuration under antiparallel out-of-plane electric field.

| Electric field | BTO | Mismatch strain | BTO surfaces | Rotating angle | Easy axis (Fe) | Strain caused by E (easy axis) | K_{mc} (J/m ³) |
|----------------|-----|-----------------|--------------|----------------|----------------|--------------------------------|------------------------------|
| 5 kV/cm | | | | 0° | | - 1.6073% | 7.5944×10^4 |
| -1 kV/cm | | a domain | | 0° | | -1.5665% | 7.4017×10^4 |
| | | | | 0.510° | | - 0.4556% | 2.1527×10^4 |
| -2 kV/cm | | c domain | | 0.735° | | -0.4521% | 2.1361×10^4 |
| -4 kV/cm | | | | 1.015° | | - 0.4514% | 2.1328×10^4 |
| -5 kV/cm | | | | 0° | | - 1.5702% | 7.419×10^4 |
| | | | | 0° | | - 1.5712% | 7.424×10^4 |

Figure 8.5. The interpretation of the strain state induced on the Fe film by the BTO domain surface at their interface during a 180° domain switching process under the application of an antiparallel electric field.

The BTO surface is under compressive strain at an electric field of 5 kV/cm and parallel to the polarization direction of the c+ domain. This strain is symmetry-induced, meaning that the magnetic easy axis of the Fe film is comparable to the bulk one. However, an out-of-plane electric field causes shear strain on a domain when it appears at -1 kV/cm. The uniaxial magnetic easy axis of the film rotates (0.510°) as a result of this strain. Similar to this, in the case of a domain, the magnetization rotates 0.735° and 0.1015°, respectively, when the applied electric field value is of -2 and -4 kV/cm. The same direction of the applied electric field and the polarization direction of

the c domain put the single c domain under tensile strain when it forms at saturation state (-5 kV/cm). The magnetic anisotropy of Fe film is back to biaxial one and its easy axes are similar to that of bulk Fe. We also can calculate the strain value on each domain on each applied electric field value. The magnetoelastic anisotropy energy is calculated following the formula presented in Chapter 7.

The change in magnetic anisotropy of the Fe film under an antiparallel electric field is depicted in Figure 8.6. The variation in H_C corresponds to the butterfly loop pattern of strain versus electric field in ferroelectric materials. This indicates a strong magnetoelectric coupling at the Fe/BTO interface, enabling full strain transfer from the substrate to the film.

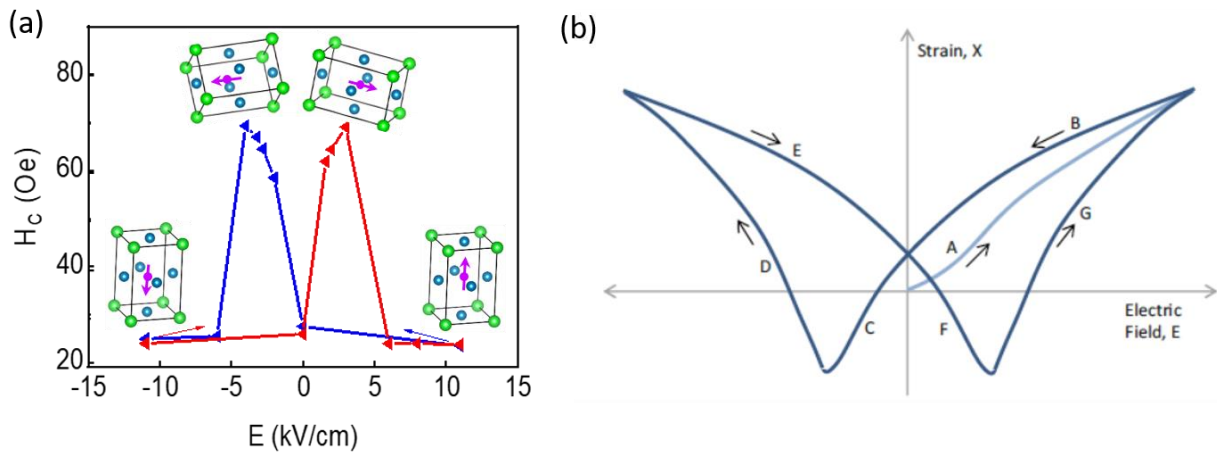


Figure 8.6. (a) Coercivity dependent of applied electric field value on 180° domain-switching process. (b) Strain – Electric field hysteresis loop of ferroelectric material with the butterfly loop.

8.4 Conclusion

The epitaxial Fe film is successfully grown on stripe a-c BTO domain. The uniaxial magnetic easy axis is exhibited on Fe film formed on a domain of BTO while the biaxial magnetic easy axis is exhibited on Fe film formed on c domain of BTO. The magnetic anisotropy modulation is originated by the full imprinting strain from ferroelastic a-c stripe domains into the Fe film during growth process. When external electric field is applied, the alternation of magnetic anisotropy from uniaxial (when the entire area is located on top of the ferroelectric a domain) to biaxial (when the underlying ferroelectric domain is of c type) and vice versa. The modulation on magnetic anisotropy is related to pinning of ferromagnetic domain walls on top of ferroelastic boundaries. As a result of our findings, we believe that a suitable strain source using can provide the change on magnetic properties which is the attractive design possibility of developing next generation magnetic switching device at ultralow energy consumption.

8.5 References

- [1] K. Eshraghian, “Evolution of Nonvolatile Resistive Switching Memory Technologies: The Related Influence on Hetrogeneous Nanoarchitectures,” *Trans. Electr. Electron. Mater.*, vol. 11, no. 6, pp. 243–248, 2010.
- [2] R. Ramesh and L. W. Martin, “Electric field control of magnetism: multiferroics and magnetoelectrics,” *Riv. del Nuovo Cim.*, vol. 44, no. 5, pp. 251–289, 2021.
- [3] R. Ramesh and N. A. Spaldin, “Multiferroics: Progress and prospects in thin films,” *Nanosci. Technol. A Collect. Rev. from Nat. Journals*, vol. 3, pp. 20–28, 2009.
- [4] S. M. Yakout, “Spintronics: Future Technology for New Data Storage and Communication Devices,” *J. Supercond. Nov. Magn.*, vol. 33, no. 9, pp. 2557–2580, 2020.
- [5] J. Ma, J. Hu, Z. Li, and C. W. Nan, “Recent progress in multiferroic magnetoelectric composites: From bulk to thin films,” *Adv. Mater.*, vol. 23, no. 9, pp. 1062–1087, 2011.
- [6] C. Lu, M. Wu, L. Lin, and J. M. Liu, “Single-phase multiferroics: New materials, phenomena, and physics,” *Natl. Sci. Rev.*, vol. 6, no. 4, pp. 653–668, 2019.
- [7] J. J. Wang, F. Y. Meng, X. Q. Ma, M. X. Xu, and L. Q. Chen, “Lattice, elastic, polarization, and electrostrictive properties of BaTiO₃ from first-principles,” *J. Appl. Phys.*, vol. 108, no. 3, 2010.
- [8] T. Mion, D. M. Potrepka, F. J. Crowne, A. Tauber, and S. C. Tidrow, “Dielectric and X-ray diffraction analysis of Ba(Ga,Ta) 0.05Ti 0.90O 3,” *Ferroelectrics*, vol. 473, no. 1, pp. 13–23, 2014.
- [9] “26.” .

- [10] S. Brivio, C. Rinaldi, D. Petti, R. Bertacco, and F. Sanchez, “Epitaxial growth of Fe/BaTiO₃ heterostructures,” *Thin Solid Films*, vol. 519, no. 17, pp. 5804–5807, 2011.
- [11] T. Mikolajick *et al.*, “Next generation ferroelectric materials for semiconductor process integration and their applications,” *J. Appl. Phys.*, vol. 129, no. 10, 2021.
- [12] J. F. Scott, “Applications of modern ferroelectrics,” *Science (80-.)*, vol. 315, no. 5814, pp. 954–959, 2007.
- [13] T. Y. Kim, S. K. Kim, and S. W. Kim, “Application of ferroelectric materials for improving output power of energy harvesters,” *Nano Converg.*, vol. 5, no. 1, pp. 1–16, 2018.
- [14] L. W. Martin and A. M. Rappe, “Thin-film ferroelectric materials and their applications,” *Nat. Rev. Mater.*, vol. 2, no. 2, 2016.
- [15] S. Zhang, B. Malič, J. F. Li, and J. Rödel, “Lead-free ferroelectric materials: Prospective applications,” *J. Mater. Res.*, vol. 36, no. 5, pp. 985–995, 2021.
- [16] S. Wada, K. Yako, K. Yokoo, H. Kakemoto, and T. Tsurumi, “Domain wall engineering in barium titanate single crystals for enhanced piezoelectric properties,” *Ferroelectrics*, vol. 334, no. 1 PART 2, pp. 17–27, 2006.
- [17] L. S. R. Rocha *et al.*, “A study approach on ferroelectric domains in BaTiO₃,” *Mater. Charact.*, vol. 120, pp. 257–262, 2016.
- [18] T. H. E. Lahtinen, K. J. A. Franke, and S. Van Dijken, “Electric-field control of magnetic domain wall motion and local magnetization reversal,” *Sci. Rep.*, vol. 2, pp. 1–6, 2012.

- [19] F. Rubio-Marcos, A. Del Campo, P. Marchet, and J. F. Fernández, “Ferroelectric domain wall motion induced by polarized light,” *Nat. Commun.*, vol. 6, 2015.
- [20] Z. K. Zhang, D. N. Fang, and A. K. Soh, “A new criterion for domain-switching in ferroelectric materials,” *Mech. Mater.*, vol. 38, no. 1–2, pp. 25–32, 2006.
- [21] V. Boddu, F. Endres, and P. Steinmann, “Molecular dynamics study of ferroelectric domain nucleation and domain switching dynamics,” *Sci. Rep.*, vol. 7, no. 1, pp. 1–10, 2017.
- [22] M. G. Shaikh, S. Phanish, and S. M. Sivakumar, “Domain switching criteria for ferroelectrics,” *Comput. Mater. Sci.*, vol. 37, no. 1–2, pp. 178–186, 2006.
- [23] X. Chao, J. Wang, J. Pu, S. Zhang, and Z. Yang, “Aging behavior and electrical properties of low-temperature sintered (Ba, Ca)(Ti, Zr)O₃-Ba(Cu, W)O₃ ceramics and plate loudspeaker,” *Sensors Actuators, A Phys.*, vol. 237, pp. 9–19, 2016.
- [24] M. Yuan *et al.*, “Biocompatible nanogenerators through high piezoelectric coefficient 0.5Ba(Zr_{0.2}Ti_{0.8})O₃-0.5(Ba_{0.7}Ca_{0.3})TiO₃ nanowires for in-vivo applications,” *Adv. Mater.*, vol. 26, no. 44, pp. 7432–7437, 2014.
- [25] N. R. Alluri, B. Saravanakumar, and S. J. Kim, “Flexible, hybrid piezoelectric film (BaTi(1-x)ZrxO₃)/PVDF nanogenerator as a self-powered fluid velocity sensor,” *ACS Appl. Mater. Interfaces*, vol. 7, no. 18, pp. 9831–9840, 2015.
- [26] X. Yan *et al.*, “Correspondence: Lead-free intravascular ultrasound transducer using BZT-50BCT ceramics,” *IEEE Trans. Ultrason. Ferroelectr. Freq. Control*, vol. 60, no. 6, pp. 1272–1276, 2013.

- [27] M. Goiriena-Goikoetxea *et al.*, “Influence of dislocations and twin walls in BaTiO₃ on the voltage-controlled switching of perpendicular magnetization,” *Phys. Rev. Mater.*, vol. 5, no. 2, 2021.
- [28] M. He, M. Wang, and Z. Zhang, “Electric-field-induced domain intersection in BaTiO₃ single crystal,” *Jpn. J. Appl. Phys.*, vol. 56, no. 3, 2017.
- [29] M. Acosta *et al.*, “BaTiO₃-based piezoelectrics: Fundamentals, current status, and perspectives,” *Appl. Phys. Rev.*, vol. 4, no. 4, 2017.
- [30] L. B. and G. J. S. Bo-Kuai Lai, Inna Ponomareva, Igor A. Kornev, “Domain evolution of BaTiO₃ ultrathin films under electric field: a first-principles study Bo-Kuai Lai, Inna Ponomareva, Igor A. Kornev, L. Bellaiche and G. J. Salamo Physics Department, University of Arkansas, Fayetteville, Arkansas 72701.”
- [31] K. J. A. Franke, T. H. E. Lahtinen, A. Casiraghi, D. L. González, S. J. Hämäläinen, and S. van Dijken, “Electric field control of magnetism based on elastically coupled ferromagnetic and ferroelectric domains,” *Nanoscale Ferroelectr. Multiferroics Key Process. Charact. Issues, Nanoscale Eff. 2 Vol.*, pp. 678–699, 2016.
- [32] P. R. Potnis, N. T. Tsou, and J. E. Huber, “A review of domain modelling and domain imaging techniques in ferroelectric crystals,” *Materials (Basel)*, vol. 4, no. 2, pp. 417–447, 2010.
- [33] J. E. Rault, T. O. Menteş, A. Locatelli, and N. Barrett, “Reversible switching of in-plane polarized ferroelectric domains in BaTiO₃ (001) with very low energy electrons,” *Sci. Rep.*, vol. 4, pp. 1–7, 2014.

- [34] C. M. Landis, “Non-linear constitutive modeling of ferroelectrics,” *Curr. Opin. Solid State Mater. Sci.*, vol. 8, no. 1, pp. 59–69, 2004.
- [35] D. Damjanovic, “Contributions to the piezoelectric effect in ferroelectric single crystals and ceramics,” *J. Am. Ceram. Soc.*, vol. 88, no. 10, pp. 2663–2676, 2005.
- [36] B. Jiang, Y. Bai, W. Chu, Y. Su, and L. Qiao, “Direct observation of two 90° steps of 180° domain switching in BaTiO₃ single crystal under an antiparallel electric field,” *Appl. Phys. Lett.*, vol. 93, no. 15, pp. 1–4, 2008.
- [37] K. J. A. Franke, D. López González, S. J. Hämmäläinen, and S. Van Dijken, “Size dependence of domain pattern transfer in multiferroic heterostructures,” *Phys. Rev. Lett.*, vol. 112, no. 1, pp. 1–5, 2014.
- [38] Y. W. Li, J. F. Scott, D. N. Fang, and F. X. Li, “90-degree polarization switching in BaTiO₃ crystals without domain wall motion,” *Appl. Phys. Lett.*, vol. 103, no. 23, 2013.
- [39] T. H. E. Lahtinen *et al.*, “Alternating domains with uniaxial and biaxial magnetic anisotropy in epitaxial Fe films on BaTiO₃,” *Appl. Phys. Lett.*, vol. 101, no. 26, pp. 1–5, 2012.
- [40] K. J. A. Franke, B. Van de Wiele, Y. Shirahata, S. J. Hämmäläinen, T. Taniyama, and S. van Dijken, “Reversible electric-field-driven magnetic domain-wall motion,” *Phys. Rev. X*, vol. 5, no. 1, pp. 1–9, 2015.

CHAPTER 9: CONCLUSIONS

In conclusion, this study has yielded valuable insights into the P-E hysteresis loop of ferroelectric BTO. For the first time, we have observed the formation of a single in-plane domain as an intermediate step during the application of an out-of-plane electric field to the a_1 - a_2 and a - c domains. We have demonstrated complete control over the BTO domain configurations by adjusting the level of the applied electric field. This result holds great promise for research in multiferroic materials that rely on strain induced by an externally applied field to control the magnetic anisotropy of films.

Additionally, we have thoroughly investigated the optimized growth conditions for Fe films on BTO substrates. It was found that when Fe films are grown on tetragonal BTO below the growth temperature of 120 °C, they exhibit tensile strain, while growth on cubic BTO above 120 °C results in compressive strain, potentially due to the presence of the FeO_x interface layer. Through our research, we have determined that a temperature of 300 °C is the ideal condition for depositing Fe films on BTO, leading to the formation of the highest-quality epitaxial films, that sample is used for the next studies. In the course of this work, we have demonstrated the electric field control of the magnetic anisotropy in epitaxial Fe/BTO heterostructures. During growth, the ferroelastic BTO domains have been fully imprinted onto the Fe film. Uniaxial magnetic anisotropy is observed in the epitaxial Fe film on the in-plane a_1 - a_2 domains, while the biaxial magnetic easy axis of Fe films is presented on a single out-of-plane c domain. Furthermore, the pinning of inter-ferroic domain walls persists during the polarization process, resulting in the motion of magnetic domain walls under an applied electric field. This confirms the coupling between the direction of the BTO

polarization and the magnetic anisotropy mediated through strain transfer at the Fe/BTO interface. Moreover, we have demonstrated the reversible electric-field-driven modulation of the magnetic anisotropy of the film. This significant result has promising implications for the future use of multiferroic materials in spintronic devices. However, it's important to note that this thesis does not fully cover the important aspects of this topic. Further research is needed to explore the magnetic anisotropy dependence on the domain size of ferroelectric BTO. My future work will not only extend to Fe films but also encompass other magnetic materials, which will be the next steps in my research journey.

ACKNOWLEDGEMENT

My journey as a PhD student in Korea has been an incredible experience that began at the age of 23. I am deeply grateful for the chance to work in such a supportive environment with some of the kindest person I have ever met.

Most importantly, I would like to express my sincere gratitude my two advisors, Prof. Sunglae Cho and Prof. Chanyong Hwang, for their unwavering support and guidance throughout my PhD research period. I am also really thankful for their dedication, including the weekends they spend discussing and correcting my published papers. I would like to acknowledge all professors in the Department of Physics at the University of Ulsan for their valuable teaching. I also would like to thank Prof. Cao Khang Nguyen for introducing me to the opportunity to study in Korea.

I wish express my thanks to Dr. Van Quang Nguyen for dedicating his time to teach me about MBE devices and for guiding me many things on science experiments, paper writing skills, and life lessons too. Additionally, I would like to show my thanks to Dr. Moon Kyoung-Woong for consistently answering my questions and providing significant assistance with MOKE measurement, a system that contributed to a substantial portion of my PhD data. I extend my gratitude to all the members of the ASM LAB and QUANTUM SPIN TEAM for creating an exceptional experimental environment.

Last but not least, I want to convey my deepest appreciation to my beloved family for their supporting and understanding throughout my PhD journey. Without them, I would not have been able to complete this thesis. “I hope I make you proud.”